

The Effect of Structural Microheterogeneity on the Initiation and Propagation of Ectopic

Activity in Cardiac Tissue

by

Marjorie Letitia Holden Hubbard

Department of Biomedical Engineering
Duke University

Date: _____

Approved:

Craig Henriquez, Supervisor

Roger C. Barr

Nenad Bursac

Donald Rose

Madison Spach

Dissertation submitted in partial fulfillment of
the requirements for the degree of Doctor
of Philosophy in the Department of
Biomedical Engineering in the Graduate School
of Duke University

2010

ABSTRACT

THE EFFECT OF STRUCTURAL MICROHETEROGENEITY ON THE INITIATION
AND PROPAGATION OF ECTOPIC ACTIVITY IN CARDIAC TISSUE

by

Marjorie Letitia Hubbard

Department of Biomedical Engineering
Duke University

Date: _____

Approved:

Craig Henriquez, Supervisor

Roger C. Barr

Nenad Bursac

Donald Rose

Madison Spach

An abstract of a dissertation submitted in partial
fulfillment of the requirements for the degree
of Doctor of Philosophy in the Department of
Biomedical Engineering in the Graduate School
of Duke University

2010

Copyright by
Marjorie Letitia Holden Hubbard
2010

Abstract

Cardiac arrhythmias triggered by both reentrant and focal sources are closely correlated with regions of tissue characterized by significant structural heterogeneity. Experimental and modeling studies of electrical activity in the heart have shown that local microscopic heterogeneities which average out at the macroscale in healthy tissue play a much more important role in diseased and aging cardiac tissue which have low levels of coupling and abnormal or reduced membrane excitability. However, it is still largely unknown how various combinations of microheterogeneity in the intracellular and interstitial spaces affect wavefront propagation in these critical regimes.

This thesis uses biophysically realistic 1-D and 2-D computer models to investigate how heterogeneity in the interstitial and intracellular spaces influence both the initiation of ectopic beats and the escape of multiple ectopic beats from a poorly-coupled region of tissue into surrounding well-coupled tissue. An approximate discrete monodomain model that incorporates local heterogeneity in both the interstitial and intracellular spaces was developed to represent the tissue domain.

The results showed that increasing the effective interstitial resistivity (ρ_{eff}) in poorly coupled fibers alters the distribution of electrical load at the microscale and causes propagation to become more like that observed in continuous fibers. In poorly coupled domains, this nearly continuous state is modulated by cell length and is characterized by decreased gap junction delay, sustained conduction velocity, increased sodium current, reduced maximum upstroke velocity, and increased safety factor. In inhomogeneous fibers with adjacent well-coupled and poorly coupled regions, locally increasing ρ_{eff} in the poorly coupled region reduces the size of the focal source needed to generate an ectopic beat, reduces dispersion of repolarization, and delays the onset of

conduction block that is caused by source-load mismatch at the boundary between well-coupled and poorly-coupled regions. In 2-D tissue models, local increases in effective interstitial resistivity as well as microstructural variations in cell arrangement at the boundary between poorly-coupled and well-coupled regions of tissue modulate the distribution of maximum sodium current which facilitates the unidirectional escape of focal beats. Variations in the distribution of sodium current as a function of cell length and width lead to directional differences in the response to increased effective interstitial resistivity. Propagation in critical regimes such as the ectopic substrate is very sensitive to source-load interactions and local increases in maximum sodium current caused by microheterogeneity in both intracellular and interstitial structure.

Dedication

To my loving husband, Lemuel, and my Mom, Dad, and brother, Brian

Table of Contents

Abstract	iv
List of Tables.....	x
List of Figures.....	xi
Acknowledgements.....	xiv
1. Introduction and Background	1
1.1 Excitable Cells and Action Potentials	2
1.2 Sources and Sinks and Impulse Propagation	4
1.3 Myocardial Architecture	5
1.3.1 Intracellular Space	6
1.3.2 Interstitial Space.....	10
1.4 Source-Sink Mismatch.....	14
1.5 Arrhythmias in the Heart	17
1.5.1 Mechanisms Underlying Cardiac Arrhythmias.....	17
1.5.2 Fibrillation in the Heart	18
1.5.3 The Arrhythmogenic Substrate	19
1.5.4 The Effect of Tissue Heterogeneity on Reentry.....	20
1.5.5 The Effect of Tissue Heterogeneity on Ectopic Activity	25
1.6 Specific Aims and Overview	28
2. History of Model Development	31
2.1 One-Dimensional Structural Models	31
2.2 Multi-Dimensional Microstructural Models.....	34
3. Models and Methods	37
3.1 Ionic Models	37

3.2	Tissue Models.....	39
3.3	Details of Time Integration and Data Analysis	47
4.	The Effect of Combined Microheterogeneity in the Interstitial and Intracellular Spaces on 1-D Propagation.....	48
4.1	Introduction.....	48
4.2	Methods.....	50
4.2.1	Discrete Fibers with Uniform Structure	50
4.2.2	Discrete Fibers with Heterogeneous Structure.....	52
4.2.3	Premature Stimulation in a Discontinuous Heterogeneous Fiber.....	53
4.2.4	Measurement and Stimulation Protocols	54
4.3	Results	55
4.4	Discussion	69
5.	Intracellular Microheterogeneity in a Monolayer of Cardiac Myocytes	76
5.1	Introduction.....	76
5.2	Methods.....	77
5.2.1	Tissue Structure.....	77
5.2.2	Myocyte Representation	78
5.2.3	Gap Junction Distribution	78
5.2.4	Membrane Properties.....	80
5.2.5	Computational Details	80
5.3	Results	81
5.3.1	Effect of brick wall tissue structure.....	81
5.3.2	Effect of jutting at cell borders	85
5.3.3	Effect of Lateral Decoupling on CV Ratio	87
5.4	Discussion	91

6.	The Effect of Tissue Microstructure on the Escape of Ectopic Beats.....	95
6.1	Introduction.....	95
6.2	Methods.....	96
6.2.1	Ionic Model.....	96
6.2.2	Structural Model (1-D).....	98
6.2.3	Randomly Generated Structural Model (2-D).....	99
6.2.4	Basic Structure Models (2-D).....	99
6.2.5	Stimulation and Measurement Protocols.....	101
6.3	Results.....	103
6.3.1	Initiation of Focal Beats in 1-D.....	103
6.3.2	Effect of Cell Arrangement in 2-D Tissue.....	105
6.3.3	Combined Effect of Cell Size and Increased ρ_{oeff} in 2-D Tissue.....	106
6.3.4	Effect of Increased ρ_{oeff} in Randomly Generated Tissue.....	110
6.3.5	Implications for ectopic beats and reentrant circuits.....	111
6.4	Discussion.....	121
7.	Conclusions.....	125
7.1	Major Findings.....	125
7.2	Limitations and Future Work.....	128
	Biography.....	142

List of Tables

Table 3.1: Comparison of conduction velocities (CV) measured in the 1-D approximate discrete monodomain model (ADMD) and discrete bidomain (BD) models	41
Table 3.2: Comparison of maximum upstroke velocities V_{\max} measured in the 1-D discrete monodomain (ADMD) and discrete bidomain (BD) models	41
Table 3.3: Comparison of conduction velocities (CV) measured in the 2-D approximate discrete monodomain model (ADMD) discrete bidomain (BD) models.....	46
Table 3.4: Comparison of maximum upstroke velocities (V_{\max}) measured in the 2-D approximate discrete monodomain model (ADMD) and 2-D discrete bidomain (BD) models	46
Table 4.1: Intracellular delay (IC Delay), gap junction delay (GJ Delay) and conduction velocity(CV) in ADMD fibers composed of cells of different lengths, L.....	58
Table 5.1: Longitudinal and transverse conduction velocities (L/T) and maximum upstroke velocities (L/T) measured over a range of gap junction conductances (g_j) in tissues with various cell arrangements.....	84
Table 5.2: Longitudinal (L) and Transverse (T) conduction velocities and maximum upstroke velocities for various tissue structures which have adult gap junction distribution and gap junctions removed at select locations.	87
Table 5.3 Longitudinal (L) and Transverse (T) conduction velocities (cm/s) and conduction velocity ratios (AR) for plane wave and point propagation in adult RAND, RANDwSD50 and RANDwSD100 tissue models.....	88
Table 6.1: Gap junction delay, $I_{Na,Max}$ and Action Potential Duration(APD) measured during longitudinal propagation as a function of ρ_{off} in different regions of inhomogeneous tissues with varied underlying structures.	108
Table 6.2: Gap junction delay, $I_{Na,Max}$ and Action Potential Duration(APD) measured during transverse propagation as a function of ρ_{off} in different regions of inhomogeneous tissues with varied underlying structures.	109

List of Figures

Figure 3.1: Tissues with varied cell arrangements.....	43
Figure 3.2: Visual representations of the (A) 2-D discrete bidomain and (B) the 2-D approximate monodomain model.....	45
Figure 4.1: Resistor grids for (A) the 1-D discrete bidomain model (B) the 1-D approximate discrete monodomain model and (C) the 1-D approximate continuous monodomain model	52
Figure 4.2: Representation of the 0.5 cm inhomogeneous fiber.....	53
Figure 4.3: Representation of a 1-cm inhomogeneous fiber with a poorly-coupled central region.....	54
Figure 4.4: The ratio of intracellular to gap junction (IC/GJ) delay and gap junction delay as a function of ρ_{eff} . IC/GJ Ratio shown for (A) well-coupled fibers and (B) poorly-coupled fibers composed of cells of different lengths, L. (C) Gap junction delay shown for poorly coupled fibers composed of cells of different lengths, L.....	56
Figure 4.5: Plots of conduction velocity as a function of ρ_{eff} for (A) Well-coupled and (B) poorly-coupled fibers composed of cells of length L. In each graph, three different equivalent models are shown: CMD2: the continuous monodomain with $dx=2 \mu\text{m}$, ADMD2: the approximate discrete monodomain with $dx = 2 \mu\text{m}$, and CMDL: the continuous monodomain with $dx=L$	59
Figure 4.6: Maximum Upstroke Velocity at cell center as a function of ρ_{eff}	60
Figure 4.7: Variation in maximum sodium current as a function of ρ_{eff}	62
Figure 4.8: Safety Factor (SF) measured in a 1-D fiber as a function of ρ_{eff}	63
Figure 4.9: Conduction along inhomogeneous fibers with different combinations of R_g and ρ_{eff}	65
Figure 4.10: Membrane Current measured at Cell 29 in the inhomogeneous fiber with $R_{g(\text{PC})}=60 \Omega\text{-cm}$ during (A) depolarization and (B) repolarization. (C) Maximum Sodium Current and (D) Action Potential Duration measured along the inhomogeneous fiber. .	66
Figure 4.11: Action Potential Dispersion along the inhomogeneous fiber when $R_g(\text{PC})=63 \Omega\text{-cm}^2$	67
Figure 4.12: The conduction delay measured at the boundary between the poorly coupled and well-coupled region as a function of the coupling interval.....	69

Figure 4.13: The maximum sodium current density (A,B) and the APD profile (C,D) in response to two consecutive stimuli (S1,S2), given in the poorly coupled region of an inhomogeneous fiber.....	74
Figure 5.1: A segmented myocyte shown with (A) an adult gap junction distribution and a (B) neonatal gap junction distribution.	80
Figure 5.2: Activation maps(A,B) and action potentials propagating parallel to the longitudinal(C) and transverse (D) axes in response to a point stimulus given in tissues with varying levels of structural discontinuity.	89
Figure 5.3: The effect of lateral decoupling on longitudinal propagation.....	91
Figure 6.1: Plots of parameters related to the funny current.....	97
Figure 6.2: Representation of a 2 cm inhomogeneous fiber, with a 1 cm poorly coupled central region.....	98
Figure 6.3: Representations of the inhomogeneous tissues with the poorly coupled region shown in gray and fibrotic strands shown in red. (A) Centralized inhomogeneous region used in the RAND model. (B) Basic inhomogeneous RAND mesh used to study longitudinal propagation (C) Basic inhomogeneous RAND mesh used to study transverse propagation.	101
Figure 6.4: (A) Plot of the focal size as a function of gap junction resistivity (R_g) and effective interstitial resistivity (B) Delay at the boundary between the well-coupled and poorly coupled regions as a function of R_g and ρ_{oeff}	104
Figure 6.5: Activation maps during the first 100 ms of propagation in inhomogeneous tissue with varying levels of escape.....	105
Figure 6.6: Distribution of $I_{\text{Na,max}}$ (A,B) and gap junction delays(C,D) in inhomogeneous RAND tissues during longitudinal(A,C) and transverse propagation(B,D) with no conduction block. <i>Dark Gray:</i> Poorly coupled Tissue. <i>Light Gray:</i> Well-coupled Tissue.	111
Figure 6.7: (A,B,C) Partial escapes shown for comparable tissues with $g_j(\text{inner})=0.003 \mu\text{S}$, $g_j(\text{outer})=0.10 \mu\text{S}$, and $\rho_{\text{oeff}}=0.5 \text{ k}\Omega\text{-cm}$ (D,E,F) Multiple escapes for tissues with ρ_{oeff} increased to $2.5 \text{ k}\Omega\text{-cm}$	113
Figure 6.8: Magnified image with isolines for the escape shown in Figure 6.7A.....	114
Figure 6.9: Magnified image with isolines for the escape shown in Figure 6.7B.	115
Figure 6.10: Magnified images with isolines for the escape shown in 6.7C.....	116
Figure 6.11: Contained reentry shown for the case with $g_j(\text{outer}) = 0.1 \text{ mS/cm}^2$, $g_j(\text{inner network})=0.002 \text{ ms/cm}^2$, and $\rho_{\text{oeff}}=0.50 \text{ k}\Omega\text{-cm}$ throughout the tissue.....	118

Figure 6.12: Progression of the escape of ectopic beat and the resulting reentry for a period of 700 ms. Shown for the case with g_j (outer) = 0.100 mS, g_j (inner) network=0.002 mS, and ρ_{oeff} increased to 5.0 k Ω -cm in the central region of the tissue.119

Figure 6.13: Partial escape from a poorly coupled region shown for two comparable cases where activation is driven by funny current focal sources. In both cases, g_j of the poorly coupled inner region is 0.003 mS, and ρ_{oeff} is uniformly equal to 0.5 k Ω -cm120

Figure 6.14: (A) Voltage activation map (time in ms) shown with contour lines during the escape. (A) Distribution of $I_{\text{Na,max}}$ ($\mu\text{A}/\text{cm}^2$) shown with contour lines after all the cells have activated. The active cell at the point of escape is indicated with a star.122

Acknowledgements

First and foremost, I would like to give all praise and glory to God for the way He has continually worked in my life. This is just the beginning of great things to come! Thank you to Dr. Craig Henriquez, my PhD advisor, for encouraging me to think independently and for giving me the space to learn and grow in my own way. Thank you also to the past and present members of the Henriquez Lab: in particular, to John Pormann for leaving his legacy to live on through *Cardiowave*, to Sarah Roberts for her research on microstructural bidomain models, to Jong Kim for chats about research and life in general, and finally to Vincent Jacquemet for his expertise in cardiac electrophysiology and his assistance in developing computational tools for the microstructural models of cardiac tissue. Thank you to my dissertation committee, Dr. Roger Barr, Dr. Nenad Bursac, Dr. Donald Rose, and Dr. Madison Spach, for providing constructive comments about my dissertation and for the practical and philosophical knowledge they passed on through class lectures and journal articles. I would be remiss if I did not thank Ned Danieley for keeping the computers in Hudson Hall 260 and 261 up and running and the wonderful staff in the BME department, Kathy Barbour, Susan Story-Hill, Ellen Ray, Joyce Franklin, Erica Clayton, Kathy Ashley, and Marcus Henderson, for their smiling faces and their willingness to help in whatever way possible. I would also like to acknowledge the National Science Foundation and the Duke Endowment Fund for the financial support during my first three years of school, and the UNCF/Merck Dissertation Fellowship program for both the financial support and mentorship during my last two years.

To my Duke Family, thank you for the chats and the support over the past six years. A special thank you to my lil' sister Bisi Lediju for deciding to join me at Duke

and helping to spice up the hall just a little bit. To my Immanuel Temple church family, you all have been great, and I couldn't have done it without you. Extra special thanks go out to the Mason, McClain, Fortune, Elliott, Trotman, and Mitchell families- your unselfish love, prayers and weekly family dinners helped to make North Carolina a home and not just a place I went to school. The time I have spent with the Praise and Worship Team at Immanuel Temple has been one of the highlights of my time here in North Carolina and great outlet for me outside of the research lab. I am forever grateful for having been a founding member, and the members of the praise team will always have a special place in my heart.

Thank you to my mom, dad, and brother for their love, laughter, and encouragement over the past twenty-seven years. I couldn't have asked for a better family! And last but certainly not least, a very, very special thank you to my wonderful husband, Lemuel Hubbard, who has been with me throughout the ups and the downs and has remained supportive for the many, many years I have been in school. Thank you for loving me just the way I am.

1. Introduction and Background

Over the past thirty years, computer models of cardiac tissue have generated a wealth of information about the complexity of interactions between membrane properties and structural heterogeneity in the heart. One of the greatest strengths of computer models is that they provide a versatile platform for researchers to help interpret experimental data and make new predictions about hypotheses that are not yet observable or testable using currently available experimental techniques. This cooperative relationship between computer models and experiments has led to a number of interesting findings such as the importance of the discontinuous nature of propagation in the heart and the prediction of unique reentrant patterns induced by extracellular stimulation(70, 102, 105, 123).

Despite the great strides that have been made in the field of cardiac electrophysiology using both computational and experimental models, there still remains a great need for the translation of basic research studies into a better understanding of the mechanisms underlying cardiac arrhythmias and ultimately into therapies for cardiac diseases. In response to this need, researchers have developed computer models of varying complexity that give a more realistic representation of cardiac structure. However, computational demands limit the amount of structural detail that can be included in large-scale models of cardiac tissue, which raises important questions about how much anatomic detail is required to adequately capture the behavior of normal and diseased cardiac tissue. One of the most commonly cited unknowns in both modeling and experimental studies is the extent to which microheterogeneity influences the nature of cardiac propagation in critical regimes

characterized by increased resistance to current flow in both the intracellular and interstitial spaces.

In this dissertation study, we use realistic, multiscale computer models to investigate how changes in interstitial properties influence basic conduction properties, ectopic activity, and the induction of microreentry in normally coupled and poorly coupled cardiac tissue. In particular, we seek answers to the following questions:

1. How does heterogeneity in intracellular and interstitial microstructure influence propagation in critical regimes characterized by reduced cell-to-cell coupling?

2. Can the combination of interstitial and intracellular microheterogeneity contribute to complex patterns of escape for ectopic beats that originate in a poorly coupled region of tissue?

3. Can continuous domains which average the microheterogeneities in the interstitial and intracellular spaces effectively capture the complex behavior observed in poorly coupled tissue?

1.1 Excitable Cells and Action Potentials

Cardiac cells are classified as excitable cells, which have the ability to generate and propagate electrical currents by passing ions and molecules through the plasma membrane, a semi-permeable lipid bilayer that controls the flow of particles in and out of the cell. In general, charged particles cannot diffuse directly through the cell membrane, and the transport of ions through the cell membrane is facilitated by

specialized structures called ion channels. At equilibrium, the separation of charges across the membrane establishes an electric field force (Nernst potential) that balances the diffusive force across the membrane. Many of the ion channels located within the excitable cell membrane are voltage-gated, and, consequently, the permeability of the membrane to specific ions can be changed simply by changing the transmembrane potential.

The activation of the cardiac cell using a stimulus current is an “all or nothing” phenomenon. For stimulus currents less than the threshold current, the cell membrane response is a passive subthreshold response that can be modeled using a simple RC circuit. Once the membrane voltage moves above threshold, the voltage-gated ion channels activate and the movement of the ions across the membrane occurs in a distinct order. This flow of current causes the voltage potential measured across the cardiac cell membrane, termed the action potential, to rapidly increase (depolarization phase), stabilize (plateau phase), and then rapidly decrease (repolarization phase). During the depolarization phase, sodium current is the primary current entering the cell. Inward calcium currents sustain the action potential plateau, and finally potassium ions rush out of the cell during repolarization.

The simplest membrane element can be represented by a “parallel conductance model,” where the Nernst potential of each ion is represented by a battery, the permeability of each ion channel is represented by a variable conductance (resistance), and the membrane capacitance of the lipid bilayer is represented as a capacitor. In a single cell, the governing equation for the membrane voltage is given as follows:

$$\frac{dV_m}{dt} = -\frac{I_{ion}}{C_m} \quad (1)$$

where V_m is the membrane voltage, C_m is the specific membrane capacitance across the lipid bilayer, and I_{ion} is the sum total of the ionic current densities passing through the membrane element.

1.2 Sources and Sinks and Impulse Propagation

In multicellular preparations such as fibers or tissue, one must not only consider the flow of currents across the membrane but also the current flow between interconnected cells. If each point in the domain is set to the same voltage, i.e. space-clamped conditions, Eq. 1 can be used to describe the membrane voltage at each point in space. Otherwise, the source-sink interactions between neighboring cells enable an action potential that is induced by a stimulus at one end of the domain to propagate from the stimulated end of the domain to the inactivated regions of the domain. Impulse propagation in a thin, cylindrical fiber is modeled using the linear core conductor model. The generalized cable equation that characterizes the core-conductor model for a cardiac fiber immersed in a large bath is as follows:

$$D \frac{\partial^2 V_m}{\partial x^2} = \beta \left(C_m \frac{\partial V_m}{\partial t} + I_{ion} \right) \quad (2)$$

where V_m is the membrane voltage, I_{ion} is the sum of all ionic current densities, D is the tissue conductivity, C_m is the specific membrane capacitance, and β is the surface-to-volume ratio.

1.3 Myocardial Architecture

Myocardial architecture influences the flow of the electrical current through the heart at all levels of scaling. At the macroscale, the heart is divided into four separate chambers: the left and right atria in the upper half of the heart and the left and right ventricle in the lower half of the heart. Electrical signals in the heart originate at the sinoatrial (SA) node in the right atrium and propagate rapidly through the atria to the atrioventricular (AV) node. After reaching the AV node, the current enters the bundle of His, passes rapidly through the branching Purkinje fiber network, and then activates the ventricular region almost instantaneously from the apex (bottom) to the base (top) of the ventricles(97). At the mesoscale, cardiac fibers in the ventricle are organized into interconnected sheets of tissue that branch and rotate by up to 180° through the endocardial, myocardial, and epicardial regions of the ventricular wall (85). Differences in cellular connections in adjacent muscle layers may enhance electrophysiological heterogeneity in the heart and contribute to wavefront reentry (81, 82). The heart contains large numbers of fibroblast cells that are responsible for depositing and maintaining the interstitial collagen network that intertwines through the sheets of cardiac tissue and provides structural support for the heart (15). In normal cardiac tissue, the cardiac fibers are still able to interconnect at discrete points. As the amount of collagen between the layers of tissue increases in response to aging or disease, the side-to-side connections between fibers become disrupted, resulting in slow, abnormal propagation (103).

While the larger structural components in the heart are the most visible sources of heterogeneity, experimental evidence suggests that components of cardiac microstructure including cell size and shape, gap junction distribution and expression,

and the amount and distribution of membrane and extracellular matrix proteins can have a significant impact on cardiac propagation, particularly in diseased tissue(58, 59). Accordingly, the impact of these microstructural features on wavefront propagation is the focus of this dissertation study. In most cases, these architectural changes can be subdivided into two major categories: changes that occur in the intracellular space of the heart and changes that occur in the interstitial (extracellular) space. Throughout this thesis, the intracellular space will refer to the interconnected myocytes, including both the region inside the cell and the gap junction coupling between cells, while the interstitial space will refer to the region surrounding the myocytes.

1.3.1 Intracellular Space

At the most basic level cardiac muscle is composed of individual myocytes that interconnect by way of gap junction proteins, enabling electrical waves to propagate throughout the heart. Although wavefront propagation appears to be continuous and coordinated at the macroscale, a number of fundamental studies regarding electrical current flow at the microscale have allowed researchers to develop a more complete picture of how structural discontinuities at all levels of scaling affect electrical propagation in both healthy and diseased cardiac tissue. In 1981, Spach et al. published the results of several experiments that investigated how electrical properties at a single measurement site changed with respect to the direction of the propagating wavefront(109). Contrary to continuous media theory, experimental measurements in canine atrial and ventricular muscle showed that increases in conduction velocity were associated with decreased maximum rate of rise of the action potential upstroke and increased time constant of the action potential foot and that conduction failure was more likely in the direction of highest velocity. These milestone studies suggested for the first

time that the discrete junctional connections between cells cause variations in cellular loading at the microscale that can provide directional differences in the safety of conduction, even when membrane properties are uniform.

Modeling studies of the discontinuous 1-D fiber have found that the junctional conduction delay may account for as much as 50% of the overall conduction time, a finding that has also been observed in 1-D strands of cultured neonatal rat cells(25). More detailed comparisons of one-dimensional (1-D) models of continuous and discontinuous fibers have also shown that conduction velocity in the discontinuous fiber is not inversely proportional to the square of axial resistivity and the maximum rate of rise of the action potential increases as gap junction resistance increases. A well-known study by Shaw and Rudy comparing the effects of reduced membrane excitability and reduced intercellular coupling in a discrete 1-D fiber with LRd membrane dynamics found that although conduction velocity decreases steadily in both cases, maximum upstroke velocity and safety factor have a biphasic response to reduced intracellular coupling(98). Conduction velocities as slow as 0.26 cm/s were possible in the case of reduced coupling compared to 17 cm/s in the case of reduced excitability. Shaw and Rudy also found that the L-type calcium current plays a much larger role in sustaining action potential propagation in poorly coupled fibers which have long conduction delays between cells.

Early studies by Fast and Kleber using 1-D and 2-D strands of neonatal rat myocytes showed that lateral coupling between cardiac fibers in the 2-D strands decreased the junctional conduction delay, thus making electrical propagation more homogeneous at the microscale; however, in contrast to the results obtained by Spach et al. in *in vitro* slices of canine myocardium, they found no directional differences in

maximum upstroke velocity and no difference in overall longitudinal conduction velocity between 1-D strands and 2-D strands of neonatal rat myocytes (24, 25). A key difference between the monolayers and the canine myocardium was the shape of the cells and the distribution of gap junctions: neonatal cells have a more spindle-like geometry, with gap junctions distributed uniformly around the periphery, while adult cells are more stair step and have a greater distribution of gap junctions at the ends of cells. A more detailed study of electrical propagation in 2-D cultured monolayers of neonatal rat myocytes by Fast et al. found that structural inhomogeneities such as non-uniform gap junction expression, non-myocyte cells, and long collagenous septa (greater than the length of a cell) were associated with variations in maximum upstroke velocity, slowed conduction velocity, and conduction block; however, subcellular inhomogeneities did not significantly affect wavefront propagation or create directional differences in the maximum upstroke velocity(24). In a subsequent experimental study in cultured strands of neonatal rat ventricular myocytes, Rohr, Kucera, and Kleber compared the effects of reduced membrane excitability and reduced gap junction coupling on microconduction. Similarly to Shaw and Rudy(98), they found that preparations with reduced coupling could support much lower conduction velocities (0.25 cm/s over 1mm) than preparations with reduced excitability, which suggests that regions of tissue with low levels of coupling may be able to facilitate microentry(91).

In recent years, Spach et al. have constructed a detailed two-dimensional model (2-D) of cardiac tissue which incorporates features of myocardial architecture such as gap junction distribution, overlap between cells, and jutting at cell borders(105). Using neonatal and adult models of cardiac tissue, they have been able to reproduce conduction velocities and maximum rate-of-rise values that are very similar to those that

have been observed experimentally. Although both the adult and neonatal models had similar conduction velocity ratios, directional differences in the action potential upstroke were only observed in the adult model of cardiac tissue. One of their most interesting findings from this model is that propagation speed and action potential waveshape in the transverse direction are significantly affected not only by gap junction distribution but also by cell size(105).

Recent advancements in tissue engineering and high-resolution optical mapping techniques have provided additional insight into how structural features such as cell alignment, fiber orientation, and gaps between rows of cells affect propagation. By using microabrasion and micropatterning methods, Bursac et al. created cardiac monolayers of neonatal rat cells with controlled degrees of anisotropy and fiber direction(10). Studies in these monolayers have shown that greater coalignment of cardiac cells increases the anisotropy ratio (AR) due to increased longitudinal and decreased transverse conduction velocities. In addition, selectively engineering gaps between cardiac fibers decreases transverse conduction velocity (increases AR) and also reduces longitudinal conduction velocity when the conduction velocity ratio is greater than 3.5. The decreases in longitudinal conduction velocity were attributed to an increase in the number of branch points in the micropatterned monolayers compared to confluent monolayers which had no gaps between rows of cells.

A more recent *in vivo* study which used genetically modified mice (Cx43/Scn5a^{1798insD/+}) to look at the combined effect of reduced gap junction coupling and reduced membrane excitability found that in the right ventricle, conduction velocity in the transverse direction (CV_T) but not the longitudinal direction (CV_L) experienced pronounced slowing compared to wildtype mice(110). The authors propose that the

lateral uncoupling may moderate changes in longitudinal propagation, and that the lower levels of coupling in the transverse direction of adult tissues may magnify the effect of reduced coupling on CV_T .

1.3.2 Interstitial Space

Cardiac myocytes are surrounded by a heterogeneous interstitial space that contains a wide variety of components including ground substance, blood vessels, connective tissue, and collagen. In a detailed study of the interstitial space, Frank and Langer quantified the content of the interstitium as 59% blood vessels, 23% ground substance distributed evenly throughout the space in the T-tubules, 6% empty space, 4% collagen, and 7% connective tissue cells(30). The ground substance, which takes up 58% of the interstitial space if the blood vessels are not considered, is primarily composed of negatively charged protein polysaccharides that are fixed in location. Ground substance is particularly prominent in the narrow space between myocyte membranes and capillary walls: the spacing is less than 200 nm for 36% of myocyte membranes(30). Taken as a whole, the extracellular space occupies approximately 27% of the total tissue; however, the intravascular compartment is thought to be electrically insulated from the interstitial space, leaving approximately 5-10% of the total space permeable to extracellular current flow(28).

One study by Levick suggests that even in healthy tissue the resistivity of the interstitial space varies non-linearly depending on both the narrowness of the space and the interaction of different fibrous components including collagen, glycosaminoglycans (GAGs) and proteoglycan core protein(69). In another study of the effect of FGF-2 (fibroblast growth factor) on angiogenesis, Filion et al. measured the rate of diffusion of the small, globular protein through the capillary and myocyte basement membranes,

which are composed of a thin but dense layer of proteoglycans, and the extracellular matrix, which is composed of a thicker but less dense collection of collagen, GAGs, and proteoglycans. Using models of binding kinetics and estimates for the different compositions of the membranes, they calculated that the diffusivity of FGF-2 through the extracellular matrix may be 35 times faster than the diffusivity through the basement membranes(27). This analysis of diffusion through different areas of the interstitial space is likely applicable for a wide range of small molecules.

Both experimental and modeling studies have shown that, similar to the intracellular space, changes in interstitial properties can also influence conduction velocity, action potential waveshape, and the dynamics of ionic currents(28, 38, 41). Fleischhauer et al. conducted experimental studies in rabbit papillary muscles to investigate the correlations between the electrical resistances of the different compartments of the extracellular space(28). In one part of the experiment, varying amounts of dextran were added to the perfusate to modulate the colloid osmotic pressure, which subsequently altered the volume (resistivity) of the interstitial space. In a separate part of the experiment, varying amounts of hematocrit (packed red blood cells) were added to the blood perfusate in the artery to vary the resistivity of the vascular space. Decreasing the colloid osmotic pressure from 36 mm Hg to 9 mm Hg decreased the extracellular electrical resistance by 56% and increased conduction velocity by 41%. Interestingly, when the colloid osmotic pressure was increased from 36 mm Hg to 9 mm Hg, the extracellular electrical resistance increased by 35% but the conduction velocity did not change. Increasing the intravascular resistivity by 3-fold had no effect on extracellular electrical resistance or on conduction velocity. Based on these findings, the researchers concluded that the current flow in the extracellular space

is primarily through the interstitial region rather than through the electrically insulated intravascular region. In addition, the researchers proposed that the insignificant change in conduction velocity as the extracellular electrical resistance increased could be due to low participation of regions with extremely high cleft resistance in propagation.

Using 3-D bidomain models of thin and thick slabs of tissue which included structural features such as anisotropy and fiber orientation, Henriquez et al. found that directional changes in the maximum upstroke velocity and the action potential foot could also be observed in tissue preparations that were connected to an adjacent bath and had unequal anisotropy in the interstitial and intracellular spaces. A related study by Roth on propagation in a 3-D bidomain also showed that action potential waveshape varies based on the location of measurement within a thick strand and that propagation proceeds much faster along the surface of a thick strand than along the core(92).

Experimental studies by Spach et al. suggest that the presence of capillaries in newborn ventricular muscles can modulate the linear phase-plane trajectory of the action potential foot in a directional manner that is not observed in *in vitro* models of cardiac monolayers. A corresponding "2-domain model" with either a discrete or continuous intracellular space coupled to a separate interstitial and intravascular space further showed that directional differences in the action potential foot could be linked to feedback from spatial variations in the interstitial electric field and the related spatial variations in the capacitive current flowing through the capillary wall(107). This model did not include the effects of the perfusing bath, which was shown by Roth to have a significant influence on the action potential foot even when measurements are taken relatively deep (150 μm) inside the tissue(93).

Using a slightly different two-domain microstructural model which included a discrete intracellular space and a separate but coupled resistive interstitial space, a recent study by Cabo and Boyden has shown that restricting the size of the extracellular space flattens the relationship between conduction velocity and gap junction conductance which reduces the sensitivity of the epicardial border cells to gap junction remodeling(12). The 2-D microstructural models used in this study included minimal overlap and jutting between cells and did not include heterogeneity in cell size or shape.

In a more complex manner, Roberts, Stinstra and Henriquez have developed a detailed 3-D geometric model of myocytes immersed in an extracellular space that contains both interstitial space and capillaries(89). Using this model, Roberts et al. were able to study the effect of non-uniform distributions of interstitial space around the cross-section of a cardiac fiber and demonstrate that extremely confined regions of the membrane can be excluded from propagation along a fiber, resulting in an increase in longitudinal conduction velocity(89). This model may be particularly useful for studying propagation in the case of bundles of tightly packed Purkinje fibers. Another study by Stinstra et al., which used the multidomain geometric model to study ischemic conditions in a cardiac fiber, verified that 1) capillary swelling after loss of hydrostatic pressure during ischemia increases the longitudinal extracellular resistivity, but not the transverse resistivity 2) cell swelling also increases extracellular longitudinal resistivity, and 3) gap junction closure has a disproportionate influence on transverse propagation resulting in very large longitudinal to transverse anisotropy ratio(115).

The consistent underlying theme across all of these studies of the interstitial space is that the spatial variation in the interstitial microstructure may also lead to unexpected changes in conduction properties in cardiac tissue.

1.4 Source-Sink Mismatch

Pathological changes in microstructure such as alterations in gap junction expression and distribution, changes in cell size, increases in interstitial fibrosis, lateral decoupling, and the appearance of patches of diseased tissue with altered membrane properties may create regions of greater source-load mismatch than is commonly observed in healthy tissue. In one of earliest modeling studies of the effect of discrete gap junctions on propagation in cardiac tissue, Joyner investigated the effect of cell length, periodic spatial variations in axial resistivity, and regions of adjacent well-coupled and poorly coupled cells using the Beeler-Reuter membrane model and a classic monodomain structural model(53). The cells were assumed to be isopotential, thus enabling the intracellular resistivity and the gap junction resistivity to be lumped into a single resistor. This study showed that the effects of cell length on action potential waveshape and conduction velocity become much more apparent as the space constant of the fiber approaches the length of the cell (as in the case of increased axial resistivity), and that the rising phase of the action potential is very sensitive to loading variations created by the distribution of axial resistance along the fiber. Joyner also noted that the effects of structure are dependent on the membrane model used in the study.

In another modeling study by Cabo et al., the propagation of a planar wavefront through a narrow isthmus was used to investigate the effect of wavefront curvature on slow conduction and conduction block(13). At the site of the escape from the isthmus, the wavefront showed pronounced curvature and reduced conduction velocity due to source-load mismatch between the small source current at the isthmus and the large area of unexcited tissue located on the other side of the isthmus. As the wavefront propagated away from the isthmus, the curvature of the wavefront decreased while the

conduction velocity increased. The critical isthmus width that resulted in conduction block was both rate-dependent and directionally dependent with isthmuses smaller than 200 μm resulting in conduction block in the longitudinal direction and isthmuses smaller than 600 μm resulting in conduction block in the transverse direction.

In a review of wavefront curvature, Fast and Kleber estimate the critical radius for which wavefront curvature affects conduction in well-coupled cardiac tissue to be approximately 150-300 μm , which would make conduction abnormalities caused by curvature difficult to detect using current experimental techniques. Small, curved wavefronts may be caused by a number of sources including escape from a narrow isthmus as shown in the study by Cabo et al. or propagation from an ectopic or pacemaker source(26).

A subsequent experimental study by Rohr, Kucera, Fast and Kleber, examined the onset of conduction block caused by source-sink mismatch at a tissue expansion from a single 1-D strand to rectangular monolayer of cells. They found that partial uncoupling of the current load using palmitoleic acid reduced source-sink mismatch and delayed the onset of conduction block at the tissue expansion. Conduction block persisted when the source was partially uncoupled; however, partial uncoupling of both the current source and current load improved conduction because of local differences in the geometry of the wavefront in the strand compared to the larger monolayer(90).

A related modeling study by Wang and Rudy used 1-D inhomogeneous fibers ($\Delta x=100 \mu\text{m}$) to investigate the effect of source-sink mismatches caused by structural discontinuities that increase tissue load (increased gap junction coupling, tissue expansion, reduced excitability)(118). In the case of increased coupling, a poorly coupled region ($g_j=0.08 \mu\text{S}$) of the fiber was connected to a well-coupled region ($g_j=2.5$

μS) that was 30 times as conductive. They found that the cells located right before the transition zone (the Achilles' heel) experienced a sharp decrease in both safety factor and the maximum sodium current and showed much longer conduction delays than were observed in the poorly coupled region of the fiber. Conduction block eventually occurred in the fiber when g_j of the poorly coupled regions was set to $0.08 \mu\text{S}$. Because of the large conduction delay during the plateau phase of the action potential at the transition site, the L-type calcium current played a much larger role in sustaining propagation along the fiber at the transition zone between the two regions.

Source-mismatch also influences action potential duration and dispersion of repolarization in cardiac tissue. Steinhaus et al. as well as Christini et al., have shown when an action potential propagates from poorly coupled to well-coupled region, the site of transition experiences an increase in action potential duration, similar to that observed during stimulation(100, 113). This increase occurs because the poorly coupled cells at the transition are more strongly connected to cells that are at an early stage of repolarization, resulting in a decrease in the loading membrane current flowing during repolarization. During propagation from a well-coupled to a poorly coupled region, the transition site experiences a decrease in action potential duration, similar to that observed during a collision. This decrease occurs because the well-coupled cells at the transition are more strongly connected to cells that have already repolarized resulting in an increase in the loading membrane current flowing during repolarization.

Several studies by Laurita and Rosenbaum have demonstrated the concept of modulated dispersion in which premature stimuli can dynamically alter inherent gradients of repolarization that exist cardiac tissue. In one such study in Langendorff-perfused guinea pig hearts, they show that in tissue with dispersion of restitution

kinetics and dispersion of diastolic intervals between cells, premature stimuli (S2) given at very long and short coupling intervals increase gradients of repolarization while premature stimuli given at intermediate coupling intervals decrease gradients of repolarization (64). In a second related study, they investigated the effect of modulated dispersion on the propagation of a second premature stimuli (S3) that was given in the center of a site of source-load mismatch that was created by adding narrow isthmus to the experimental preparation (65). They found that when the S3 beat was given after S1-S2 beats with very long and very short coupling intervals (large repolarization gradients), unidirectional conduction block occurred. When the S3 beat, was given after S1-S2 beats with intermediate coupling intervals (lower repolarization gradients), unidirectional conduction block did not occur. In summary, these studies suggest that sites of source-load mismatch are also sensitive to local current gradients during repolarization and may contribute to the formation of arrhythmogenic substrates.

1.5 Arrhythmias in the Heart

1.5.1 Mechanisms Underlying Cardiac Arrhythmias

Reentry and focal activity are the two main mechanisms underlying arrhythmias in the heart(77). Reentry occurs in the heart when a region of tissue recovers quickly enough to be re-excited by a neighboring region of excitable tissue. Reentrant circuits in the heart can be created by a single circulating source (observed clinically as tachycardia), multiple wavelets, or a completely disorganized pattern of wavefront propagation (observed clinically as fibrillation)(2, 78). The concept of reentry was first described by George Mines in a ring of cardiac tissue 1913 and has been studied extensively ever since(76). The two basic requirements for reentry are slow conduction

and uni-directional conduction block, both of which enable portions of recovered and excited tissue to exist simultaneously the same region of tissue(1, 88).

Focal (Ectopic) activity occurs when a region of cells in the heart, aside from pacemaker cells in the sinoatrial node, fires rapidly and electrically activates the cardiac muscle. Focal activity occurs in response to triggers such as delayed afterdepolarizations and early afterdepolarizations or due to enhanced automaticity caused by funny currents or other hyperpolarization-activated currents in cardiac cells(17). When combined with a heterogeneous substrate, rapidly firing focal sources can also be an initiating source of reentry in the heart.

1.5.2 Fibrillation in the Heart

Ventricular fibrillation (VF) is one of the most widely studied cardiac arrhythmias because it often occurs without warning and patients who are not treated rapidly after the onset of fibrillation quickly die from lack of blood flow to the rest of the body. Ventricular fibrillation is a major cause of sudden cardiac death and is thought to be responsible for 19% of deaths in the United States alone. Reentry is one of the major drivers for ventricular arrhythmias(77); however, ectopic sources have also been linked to the occurrence of arrhythmias during ischemia (low blood flow to a region of the heart) and reperfusion (restoration of blood flow)(17).

Atrial fibrillation (AF) is the most commonly diagnosed abnormality in heart rhythm affecting almost 10% of patients over 80 years old. Although atrial fibrillation is not lethal, it significantly increases the risk of stroke and heart failure(32, 66). The exact mechanisms underlying atrial fibrillation are not completely understood; however, a number of research studies suggest that rapidly firing ectopic foci and/or reentrant waves in the atrial sleeves of the pulmonary veins (PV) and upper left atria may be a

primary driver of atrial fibrillation (AF) in patients both with and without structural heart disease (3, 4). The atrial sleeves extend from an opening in the left atrium as far as 25 mm into the pulmonary vein. Both spirally oriented and longitudinally oriented myocyte cell arrangements have been observed in the PV, and fibrotic tissue is found interspersed with myocytes throughout the entire length(43). In the narrow peripheral end of the pulmonary vein, the myocytes are surrounded by a high density of blood vessel branches and a scalloped elastic laminae(94).

1.5.3 The Arrhythmogenic Substrate

The early stages of ischemia in the ventricles of the heart are characterized by a number of pathological changes including an increase in the extracellular resistance due to a decrease in perfusion pressure and intravascular volume followed by an increase in the intracellular resistance due to gap junction uncoupling(57). During reperfusion, the ectopic activity generated in the ischemic region escapes to the surrounding tissue leading to widespread arrhythmias as the conditions return to normal. Untreated ischemia results in cell death and myocardial infarction, and the necrotic tissue is replaced with unexcitable scar tissue that facilitates slow, tortuous conduction(19, 80). The infarcted region also undergoes structural remodeling such as a reduction in connexin levels and lateralization (redistribution of Cx43 from the cell ends to the lateral edges)(14, 73). The heterogeneity in the border zone between the infarcted tissue and the healthy tissue may enable relatively benign ectopic beats to develop into more widespread reentrant cardiac arrhythmias(4, 83).

The myocardial sleeves near the pulmonary vein are a primary site of origination for focal triggers in atrial fibrillation(52). Histology studies have revealed a heterogeneous substrate characterized by a decrease in gap junction coupling, increased

collagen fibrosis, and non-uniform cell and fiber arrangement, particularly farther inside the PV where ectopic foci are thought to originate(3, 44, 95). In older patients, patients with structural heart disease and in patients with persistent AF both the pulmonary veins as well the surrounding atrial myocardium show a large decrease in gap junction coupling (both Cx40 and Cx43) and a large increase in the amount of fibrotic tissue which may help to sustain both ectopic activity as well as microreentry(58, 72). Because AF leads to both electrical and structural changes that further increase the likelihood of AF (“AF begets AF”), an alternative approach to AF therapy is targeting the adverse structural remodeling (cellular uncoupling, fibrosis) that occurs in the intercellular space of atrial tissue(121). *In-vivo* studies seem to indicate that increasing gap junction coupling using novel pharmacological therapies such as rotigaptide decreases the number of arrhythmias due to reentry, but has no effect on the incidence of arrhythmias caused by focal activity, thus raising additional questions about how pathological changes such as increased fibrosis or tight spaces in the interstitial space of diseased atria affect ectopic behavior. The importance of understanding how combined changes in both the interstitial and intercellular spaces influence AF is further underscored by the anti-arrhythmic benefit of newer drug therapies such as ACE inhibitors which have been shown to decrease the amount of interstitial fibrosis(7).

1.5.4 The Effect of Tissue Heterogeneity on Reentry

A number of researchers have used *in vitro* experimental studies and simulation studies with varying levels of structural discontinuity to investigate the effect of three major classes of microheterogeneities on reentrant activity: cellular uncoupling, small, randomly distributed obstacles and sinks ($0.040 \text{ mm}^2 - 1 \text{ mm}^2$), and long, thin obstacles.

Cellular Uncoupling

In one study of the effect of cellular uncoupling on spiral wave dynamics, Bub et. al. found that application of heptanol (a gap junction uncoupler) to heterogeneous cultures of embryonic chick myocytes created regions of conduction block that triggered the formation of multiple rotating waves instead of the double-armed spiral observed in control cultures(9). In order to gain further insight into the effect of heterogeneity and cell-to-cell coupling on wavebreak, they also ran computer simulations using cellular automaton models with heterogeneities, discrete cellular automaton models without heterogeneities, and continuous models with randomly distributed heterogeneities. Based on these simulations, they conclude that small-scale heterogeneities significantly influence wave break-up, particularly when conduction velocity is reduced.

Qu used a finely discretized anisotropic continuous model to investigate how reductions in coupling strength and random uncoupling of cells affect spiral wave cycle length(87). He found that moderate reductions in coupling strength did not significantly impact cycle length, but randomly uncoupling cells increased the cycle length of the spiral wave and, consequently, stabilized spiral wavebreak in tissue with a steep restitution curve. In this type of model, it is not easy to relate the random properties to the underlying tissue structure and the approach cannot account for the complex patterns of cell coupling such as that seen in adult cells or the effect of reducing cell coupling in the presence of other structural inhomogeneities.

Small, Randomly Distributed Obstacles

A study by Steinberg et al. introduced heterogeneities into cultured monolayers of embryonic chick cells by pre-plating the culture cover slips with varying levels of

collagen(111). As the background collagen concentration decreased, the monolayers showed variations both in cell density and connectivity throughout the substrate as well as an increase in reentrant and fragmented wavefronts. In order to test the hypothesis that variations in cell density and reduced intercellular coupling were responsible for the increase in abnormal propagation, the authors created several continuous models with different densities of randomly distributed current sinks (each sink $\sim 0.040 \text{ mm}^2$). Fitz-Hugh-Nagumo membrane models were used to model the ionic currents. They found that increasing the density of current sinks caused a linear decrease in conduction velocity followed by “an abrupt transition to conduction block.” The point of transition to conduction block correlated well with the appearance of fragmented and reentrant waves; wavebreak and reentry could only be initiated by interaction of the wave with clusters of current sinks as opposed to a single sink. This study once again suggests the existence of a critical regime that significantly increases vulnerability to conduction abnormalities.

Steinburg et al. also found that uniform decreases in the diffusion coefficient (coupling) led to increased stability of waves at higher sink densities. This discrepancy was explained by creating a dimensionless scaling factor that accounted for differences in transit time between multiple heterogeneities at different conduction velocities; however, the authors note that the results from the model are in contrast to other experimental findings such as the one by Bub et al. which showed decreased wave stability when coupling was reduced. The authors further suggest that discrete models may be needed to accurately simulate propagation in the presence of significant heterogeneity and low levels of coupling. Additional studies using microstructural

computer models that are more directly correlated with *in vitro* monolayers would be useful for validating this hypothesis.

In an *in vitro* optical mapping study using isotropic monolayers, Bian and Tung investigated the mechanism by which a central region with a zig-zag pattern of discontinuities similar to that observed in infarcted ventricular tissue facilitates reentry during rapid pacing(5). They found that the effect of asymmetries in the transverse connections within the center region was especially pronounced when the overall number of transverse connections was low and the rate of pacing was high and that reentry was more easily induced in cultures with spatial asymmetry due to differences in conduction velocity restitution and conduction block. The paced beats in this study were given outside of the central region, whereas ectopic beats would more likely originate inside of the poorly coupled region.

The macroscopic effects of long, thin obstacles on conduction in 2-D monolayers correspond well with results from experimental studies in larger tissue preparations. Several studies by Spach et. al., have shown that substrates with large anisotropy (crista terminalis (atria), fibrotic tissue, etc.) have directional differences in maximum upstroke velocity that can increase the likelihood of uni-directional conduction block and wavefront re-entry. Similarly, observations of electrical propagation in infarcted ventricular tissue have also shown that regions of dense, elongated fibrotic tissue decrease transverse intercellular coupling and create slow, tortuous conduction pathways that favor the formation of reentrant circuits.

The majority of computer modeling studies described above have investigated the effect of tissue heterogeneities on reentry using coarsely discretized tissue models. A more recent microstructural model, which models fibrosis by placing long, thin barriers

between rows of cells, was created by Spach et. al. to explain variable responses to same site S1-S2 stimulation in aging human atrial bundles. They found that conduction abnormalities (wavefront shifts, microreentry) observed in both experimental and simulated extracellular waveforms were caused in large part by directional differences in incremental and decremental propagation. This study also provides evidence that structural inhomogeneities may create local differences in wavefront propagation that increase tissue sensitivity to premature stimuli and the magnitude of the sodium current.

Researchers have been able gain more insight into the effects of microheterogeneity in vivo by experimenting with genetically engineered mice with varying levels of Cx43 (also termed CKO mice). Studies of propagation in strands of myocytes from germline Cx43 $-/-$ cells showed that in the absence of Cx43, cell-to-cell conduction delays significantly increased and conduction velocity decreased to 4% of the value observed in wildtype Cx43 $(+/+)$ mice 35. Studies of propagation in Cx43 $+/-$ heterozygous mice with ~50% of wildtype Cx43 levels showed essentially no change in conduction velocity and no increased risk of arrhythmias except in the presence of other triggers such as ischemia. Similarly, a study of O-CKO mice with a progressive loss of Cx43 also showed that moderate reductions in Cx43 levels did not significantly impact CV; however, continued reduction of Cx43 levels to less than 50% of levels observed in control mice reduced conduction velocity by as much as 50%, prolonged QRS duration, reduced QRS amplitude, and greatly increased the risk of sudden cardiac death presumably due to cardiac arrhythmia.

1.5.5 The Effect of Tissue Heterogeneity on Ectopic Activity

Several simulation studies of ectopic activity in the atria and ventricles suggest that coupling-induced changes in electrical load can influence whether a cell or group of cells will transform into a source of spontaneous activity and whether the triggered beat can propagate to the surrounding tissue. The most widely used ionic model of spontaneous and triggered activity is a modified LRd model developed to mimic the cell response to calcium overloading. Studies using this model suggest that very high and very low levels of coupling between the focal source and the surrounding tissue lead to loading effects that suppress focal activity, while intermediate values of coupling facilitate focal activity(96, 122). The level of coupling has also been shown to influence the membrane potential and rate of firing associated with the ectopic event.

Other researchers have investigated the effects of coupling and anisotropy in two-dimensions by incorporating a simulated spontaneous source such as a sinoatrial cell or by pacing real or simulated myocytes incorporated within a simulated continuous sheet of cardiac tissue(117, 119). These studies also indicate that there is a window of coupling that enables the initiation and propagation of focal activity and further suggest that structural changes that increase the anisotropy of the substrate facilitate ectopic activity.

Additional information about the role that microscale changes in coupling play in facilitating spontaneous behavior has been provided by recent in vivo studies as well as in-vitro studies in isotropic neonatal monolayers. Gutstein et al. used genetically engineered chimeric mice, which have localized patches of uncoupled cardiac cells juxtaposed to regions with high levels of coupling, to study the impact of focal uncoupling on both reentrant and ectopic activity(36). They found that chimeric mice

had a greater incidence of spontaneous events compared to wildtype mice, but did not have a greater likelihood of sustained arrhythmias. These studies suggest that focal activity may have a more complex dependence on the pattern of heterogeneity, in which the formation of an ectopic beat is facilitated by isolated regions of uncoupled cells and sustained propagation is facilitated by a more widespread degree of gap junction uncoupling.

Another research group has created several *in vitro* experimental models of a small spontaneously active region characterized by heterogeneous uncoupling ('ectopic nexus'), surrounded by a larger, well-coupled quiescent region(4, 6, 86). Spontaneous activity in the central region was triggered experimentally by applying BaCl₂ or isoproterenol, while Heptanol was used to uncouple cells in the region of interest. FitzHugh-Nagumo and Beeler-Reuter computational models of spontaneously active cells were combined with continuous isotropic models in order to gain insight into the experimental results. In the case of the FHN model, cellular uncoupling was simulated in a portion of model tissue by uniformly reducing the diffusion coefficient as a function of time. Their structural model consisted of two connected continuous sheets of size 0.3 mm x 0.6 mm. In the case of the Beeler-Reuter model, a well-coupled and poorly coupled region of tissue were separated by a region of tissue with a exponential gradient of coupling. The boundary between the well-coupled and poorly coupled regions was shifted gradually in time in order to simulate time-varying conditions that may occur during reperfusion after ischemia. Both the experimental and computational models have provided additional evidence that (1) regions of low, heterogeneous coupling promote the development of spontaneous activity (2) mass propagation of local ectopic waves is facilitated by moderate levels of coupling between the focal source and the

surrounding tissue and (3) transitions in the border zone between well-coupled and poorly-coupled tissue can strongly influence the dynamics of the ectopic nexus.

While these models present evidence that low levels of cellular connectivity and heterogeneity in cellular automaticity facilitate the development of more widespread ectopic activity, they do not fully answer questions about how heterogeneities in structure (rather than in membrane excitability) modulate ectopic activity.

Notably, there are only a few computational studies that have combined detailed ionic models with structural models in order to investigate ectopic activity. In one model, Winslow et al. were able to generate propagating focal sources by inducing Na-K overloading in a relatively small region of composed of 1000 rabbit cells. The structural model used in the study was a continuous 2-D model consisting of 512x512 uniformly coupled cells(124). In a more recent model, Kuijpers et al. investigated the role of I_f on propagation using a 2-D discrete bidomain model, the Cellular Bidomain Model that included structural remodeling such as reduced gap junction conductance and diffuse fibrosis(63). The underlying structure in the model was an irregular brick wall with subelements that were 200 μm x 80 μm . The Courtemanche model of human atrial cells was used as the ionic model, and a funny current based on the DiFrancesco-Noble model formulation was added to the diseased portions of tissue. They found that ectopic activity occurred in regions of tissue with high I_f and cellular uncoupling. In regions of tissue with poor coupling, they were able to generate ectopic activity with focal regions comprising 10% of the total tissue area.

The combination of a detailed ionic model, which can give insight into the relative roles of sodium and calcium currents, and a detailed structural model, which

can take into account the low, heterogeneous levels of coupling at the microscale, may be essential for understanding the mechanisms underlying ectopy in diseased tissue.

1.6 Specific Aims and Overview

Although a large body of research has been dedicated to investigating the effect of tissue heterogeneities on wavefront propagation, there still remain many questions about how the size and the distribution of microstructural discontinuities affect macroscopic conduction properties in critical regimes characterized by low intercellular coupling and focal or other abnormal membrane activity. In addition, the effect of interstitial microheterogeneity on propagation is often overlooked, even though there is substantial experimental evidence to suggest that the components in the interstitial space such as blood vessels, basement membrane proteins, collagen, etc. contribute to heterogeneity in both the size and the composition of the space. (12, 28, 89, 104)

In order to gain additional insight into the nature of cardiac propagation in these critical regimes, the following hypotheses and specific aims were proposed in this dissertation study:

Hypothesis 1. Reduction of the interstitial space reduces the relative importance of the gap junction resistance, thus facilitating very slow conduction and altering conditions (gap junction delay, changes in load, etc.) that lead to conduction block

Specific Aim 1. To construct 1-D and 2-D models of cardiac tissue that include both intercellular and interstitial spaces, and study the effects of effective interstitial resistivity(which is related to both the material composition of the space and the size of

the space) on axial current flow, repolarization dynamics, maximum sodium current and safety factor (SF) in tissue with normal coupling and in tissue with reduced coupling caused by structural remodeling.

Hypothesis 2. Local increases in effective interstitial resistivity will decrease the size of the area needed to initiate a propagated focal activation, while heterogeneities in the effective interstitial resistivity will increase the likelihood of uni-directional conduction block and microreentry.

Specific Aim 2. To construct 1-D and 2-D models that incorporate heterogeneous interstitial and intracellular spaces and determine how changes in the effective interstitial resistivity affect the focal size needed to initiate and propagate ectopic beats and the inducibility of sustained macro and micro-reentry.

Chapter 2 presents an overview of the bidomain and monodomain structural models that have historically been used to study propagation in cardiac tissue. An alternative model, the approximate discrete monodomain (ADMD) model, is presented in Chapter 3, and is used throughout the dissertation study to investigate the combined effect of intracellular and interstitial microstructure on propagation. Details of the ionic models, the microstructural models, and the computational methods are also presented in Chapter 3.

In Chapter 4, one-dimensional ADMD models of cardiac fibers are used to investigate the effect of increased effective interstitial resistivity on conduction properties such as conduction velocity, maximum upstroke velocity, conduction delay, and maximum sodium current in well-coupled and poorly coupled tissue. We also look

at how local increases in effective interstitial resistivity influence the escape of single beats and premature beats from a poorly coupled region into an adjacent well-coupled region. The results in this chapter have been published in the *American Journal of Physiology-Heart and Circulatory Physiology* (used with permission) and also as a conference proceedings paper for the *Computers in Cardiology Conference*(49, 50).

Chapter 5, which was published in the *Europace* journal (used with permission), examines the effect of specific components of myocardial architecture such as cell arrangement, gap junction placement, and lateral decoupling on propagation in both well-coupled and poorly coupled tissue using 2-D microstructural models based on classical discrete monodomain models (51). The effect of the interstitial space is added to the 2-D microstructural model to create a 2-D ADMD model that is used in Chapter 6 to examine how co-localization of regions of increased effective interstitial resistivity and regions with intracellular heterogeneity influence the escape of ectopic beats in ventricular tissue. In Chapter 7, we summarize the major findings and present the limitations of our model and areas for future study.

2. History of Model Development

Most early structural models of cardiac tissue were based on extensions of the continuous core-conductor model that had been successfully applied to electrical propagation in nerve fibers (54, 56). In this chapter, we give a brief overview of models that have been developed over the past thirty years to incorporate more details about the unique interstitial and intracellular microstructure of cardiac tissue.

2.1 One-Dimensional Structural Models

Classical Continuous Bidomain

One of the most commonly used structural models of cardiac tissue is the bidomain model, which represents the intracellular and interstitial regions as two overlapping continuous domains. In the classical bidomain, the heterogeneities of the intracellular and interstitial spaces are averaged together and used to assign the bidomain conductivities(38).

$$\frac{1}{\rho_{ieff}} \frac{\partial^2 \phi_i}{\partial x^2} = \beta' I_m - I_{stim,i} \quad (3)$$

$$\frac{1}{\rho_{oeff}} \frac{\partial^2 \phi_e}{\partial x^2} = -\beta' I_m - I_{stim,e} \quad (4)$$

$$I_m = I_{ion} + C_m \frac{\partial V_m}{\partial t} \quad (5)$$

where Φ_i is the intracellular potential, Φ_e is the extracellular potential, and $V_m = \Phi_i - \Phi_e$ is the transmembrane potential. I_m is the transmembrane current density which is split into an ionic current, I_{ion} , a capacitive current, where C_m is the specific membrane capacitance, and intracellular and extracellular stimulus current densities, $I_{stim,i}$ and $I_{stim,e}$

(23, 74). The effective intracellular and interstitial resistivities, ρ_{ieff} and ρ_{oeff} , are functions of space and are equal to the resistivity of the subcellular region divided by the fraction occupied by the intracellular or interstitial domain: $\rho_{ieff} = \rho_i / f_i$, $\rho_e = \rho_e / f_e$, and $f_i = 1 - f_e$. β' is surface to volume ratio multiplied by the intracellular volume fraction, f_i . These definitions are applicable to all of the model equations described in this chapter.

Equivalent Continuous Monodomain

In the case of the continuous bidomain, which has no spatial variation in ρ_{ieff} , the governing equation for the equivalent continuous monodomain (CMD) can be expressed as

$$\frac{1}{\rho_{ieff} + \rho_{oeff}} \frac{\partial^2 V_m}{\partial x^2} = \beta' I_m \quad (6)$$

Classical Discrete Monodomain

In response to the findings of Spach et al. there was a shift from continuous models that represented cardiac tissue as a fully connected medium to more discontinuous models that represented cardiac tissue as groups of cells interconnected through gap junctions(109). In the 1-D fiber, this is accomplished by introducing periodic resistive connections between cells that have a higher resistance than the inside of the cardiac myocyte, but a lower resistance than the cell membrane. The fiber is also assumed to lie in a large bath so the extracellular space has a negligible influence on conduction properties. The governing equation for the classical discrete monodomain is given in Eq. 7.

$$\frac{\partial}{\partial x} \left(\frac{1}{\rho_i(x)} \frac{\partial}{\partial x} V_m \right) = \beta I_m \quad (7)$$

Notably, one study by Shaw and Rudy which used the LRd model to study electrical propagation in a discrete 1-D cardiac fiber found that when the discretization element was set equal to average length of a single myocyte and the gap junction resistance was lumped with the intracellular resistivity, electrical properties such as conduction velocity and maximum upstroke velocity were within 1% of the values obtained using a highly-discretized, discontinuous fiber(98).

Discrete Bidomain

In order to study the combined effect of increased interstitial resistivity and microscale heterogeneities such as gap junction coupling and cell size on propagation, several researchers have implemented a discrete form of the bidomain model which has been used to look at the effect of discrete gap junctions on extracellular potential distributions(60, 116).

The governing equations for the 1-D discrete bidomain (BD) model can be expressed as

$$\frac{\partial}{\partial x} \left(\frac{1}{\rho_{ieff}(x)} \frac{\partial}{\partial x} \phi_i \right) = \beta' I_m \quad (8)$$

$$\frac{\partial}{\partial x} \left(\frac{1}{\rho_{oeff}(x)} \frac{\partial}{\partial x} \phi_e \right) = -\beta' I_m \quad (9)$$

$$I_m = I_{ion} + C_m \frac{\partial V_m}{\partial t} - I_{stim} \quad (10)$$

Equivalent Discrete Monodomain

Although the discrete bidomain model is more structurally accurate, the fine discretization needed to create this model is computationally expensive which makes it difficult to run large numbers of simulations efficiently particularly in multi-dimensions (61, 71). As described in the section above, previous studies of the classical continuous bidomain have applied the condition of equal anisotropy in order to reduce the continuous bidomain to an equivalent monodomain model which is less computationally expensive(39). In 1-D, when the ratio of the intracellular to interstitial resistivity along the fiber is equal to a constant, $\rho_{ieff}(x)=k\rho_{oeff}(x)$, the governing equation for the equivalent discrete monodomain can be expressed as

$$\left(\frac{k}{1+k} \right) \frac{\partial}{\partial x} \left(\frac{1}{\rho_{ieff}(x)} \frac{\partial}{\partial x} V_m \right) = \beta' I_m \quad (11)$$

As ρ_{oeff} approaches zero, Eq. 11 becomes equivalent to the classical discrete monodomain equation described in Eq. 7 (98).

2.2 Multi-Dimensional Microstructural Models

Creating realistic models of cardiac structure becomes much more computationally challenging as the number of dimensions increases and, consequently, the complex structure of the tissue is often visualized most easily as a resistor grid. Leon and Roberge developed a 2-D parallel cable network in which each row of cardiac cells is represented as a continuous fiber and multiple rows of cardiac cells are connected in parallel by a regular pattern of transverse resistors. This approach is computationally efficient and allows for a more discontinuous representation of transverse propagation. Another version of the coupled cable model also incorporates discrete gap junctions at

random intervals along the fiber, allowing for discontinuous propagation in both longitudinal and transverse directions. One disadvantage of this model is the inability to model microstructural differences in gap junction distribution similar to those observed in normal and diseased adult tissue.

Spach et al. have constructed a detailed two-dimensional model (2-D) of cardiac tissue that incorporates features of myocardial architecture such as gap junction distribution, overlap between cells, and jutting at cell borders. Using neonatal and adult models of cardiac tissue, they have been able to reproduce conduction velocities and maximum rate-of-rise values that are very similar to those that have been observed experimentally. In order to study the effect of interstitial and intravascular loading effects on cardiac propagation, Spach et al. also created a two-domain model consisting of a discrete 2-D intracellular space coupled to a separate extracellular space which included both an interstitial space and inactive capillaries. Using this model, they were able to model directional changes in the action potential foot as a function of capacitive loading without requiring the presence of an extracellular bath adjacent to the tissue preparation, which can also influence action potential waveshape.

In a recent study, Kuijpers et al. presented a new discrete bidomain model, termed the Cellular Bidomain model, that represents the structure of cardiac tissue using a simulation graph(63). The nodes of the graph represent segments which have both an internal and external potential, while the edges of the graph represent cell coupling which is defined as either an internal or external conductance. At a minimum each segment represents a single cell, which means that this model cannot be used to investigate the subcellular dynamics of propagation.

Roberts, Stinstra and Henriquez have developed a detailed 3-D geometric model of myocytes immersed in an extracellular space that contains both interstitial space and

capillaries. In one subsequent study using this model, Stinstra et al. were able to estimate bidomain extracellular conductivities for healthy tissue that were in accordance with values reported in the literature. In the intracellular space, the effective longitudinal conductivities were in accordance with the literature values, but the effective transverse values were much smaller than reported(114). In another study comparing the multidomain model to the bidomain model, Roberts et al. found that the bidomain model was a suitable representation for macroscopic intracellular and extracellular conduction properties such as conduction velocity but could not capture the effects that non-uniform cross-sections of confined interstitial space have on propagation along fibers(89). This model may be particularly useful for determining the limits for which the less intricate bidomain model is an accurate model of cardiac propagation.

Microstructural models of cardiac tissue are computationally demanding and are most often limited to very small spatial domains over a time span of less than one second. For this reason, a large majority of computational studies of wavefront propagation are done using coarsely-discretized, continuous models that capture wavefront dynamics in relatively uniform tissue but may not be able to capture complex wave dynamics in critical regimes characterized by low intercellular coupling, microstructural heterogeneity, and reduced or abnormal membrane excitability. In Chapter 3, we present a computationally efficient approximate monodomain model that is used throughout this thesis to study the combined effect of increased effective interstitial resistivity on propagation in poorly coupled 1-D fibers and 2-D tissues.

3. Models and Methods

3.1 Ionic Models

Hodgkin-Huxley Model Formalism

In the early 1950's, Hodgkin and Huxley developed a model to simulate the response of a single nerve cell to a voltage stimulus based on the behavior of single channels(46). Notably, this model provides a way to evaluate the conductivities for a given ion channel. The "gates" (Y_k) controlling the ion channels are assumed to follow first order kinetics as shown in Eq. 12, and the rate constants α and β can be found using experimentally determined analytic functions that depend only on the transmembrane voltage. The ionic current (I_k) that flows through each channel is described by Ohm's Law.

$$\frac{dY_k}{dt} = \alpha_k(1 - Y_k) - \beta_k Y_k \quad (12)$$

$$I_k = g_k(V_m - E_k) \quad (13)$$

where Y_k is the fraction of open channels, α_k and β_k are the rate constants describing the opening and closing of channels, and g_k is the conductance of the channel.

Luo Rudy 1 Cardiac Model

The Luo-Rudy I (LR1) model (1991) is used in Chapter 5 to describe the ionic currents in the cardiac membrane using the Hodgkin-Huxley formalism(75). The LR1 model is based on six ionic currents (I_{Na^+} , I_{Si} , I_K , I_{K1} , I_{Kp} , I_b) with a total of eight gating variables ($m, h, j, d, f, X, X_i, K_1$) and one ionic concentration. These variables are also referred to as membrane state variables.

Luo Rudy Dynamic (LRd) Cardiac Model

The Luo Rudy dynamic (LRd) model was developed in 1994 to describe the flow of currents across the membrane of a ventricular guinea pig cardiac cell(74). Similar to the Luo Rudy I membrane model, Hodgkin-Huxley formalism was used to describe the ionic currents. The membrane model includes 31 state variables and 16 ionic currents. The most significant improvements in the model compared to the LR1 model are the inclusion of pumps and exchangers and the detailed expression of calcium dynamics.

Luo Rudy Dynamic (LRd) Model with funny current

To generate spontaneously active regions of tissue, the membrane currents were modeled using a modified Luo-Rudy dynamic model that included a funny current based on the Difrancesco-Noble model of human Purkinje cells(21). The equations (Eq. 14-17) governing the funny current are shown below:

$$I_f = G_f(V_m - E_f) \quad (14)$$

$$\frac{dy}{dt} = \alpha_y(1 - y) - \beta_y y \quad (15)$$

$$\alpha_y = 5 \times 10^{-4} \exp\left(\frac{-V_m}{14.92}\right) \quad (16)$$

$$\beta_y = 0.8 \exp\left(\frac{-V_m}{14.92}\right) \quad (17)$$

where V_m is the membrane voltage, G_f is the maximum conductance of the funny channel, E_f is the equilibrium potential of the funny channel (set to 40 mV), y is the fraction of open channels, α_y and β_y are the rate constants for the opening and closing of the funny current voltage-gated channel.

3.2 Tissue Models

1-D Approximate Discrete Monodomain

Because the focus of this study is primarily the effect of the interstitial space on propagation in heterogeneous tissue not on the effect of stimulation, the approach we used was to approximate a more general form of the equivalent discrete monodomain (Eq. 11), which incorporates spatial variations in ρ_{ieff} and unequal ratios of ρ_{ieff} and ρ_{oeff} , with a discrete version of the classical continuous monodomain (Eq. 7). The governing equation for the approximate discrete monodomain (ADMD) model in 1-D can be expressed as

$$\frac{\partial}{\partial x} \left(\frac{1}{\rho_{ieff}(x) + \rho_{oeff}(x)} \frac{\partial V_m}{\partial x} \right) = \beta' I_m \quad (18)$$

Using a finite difference approximation, the governing equations for the ADMD equations can be discretized as:

$$[D_{i+1/2}(V_{i+1} - V_i) - D_{i-1/2}(V_i - V_{i-1})]/\Delta x^2 = \beta' I_m \quad (19)$$

$$I_m = I_{ion} + C_m \frac{dV_i}{dt} \quad (20)$$

All of the variables in the monodomain models are defined as in the case of the discrete bidomain. In all of the simulations, the $C_m = 1 \mu\text{F}/\text{cm}^2$ (29, 45).

Validation of the 1-D ADMD Model

Propagation was studied in a discrete 0.5 cm fiber composed of 50 cardiac cells, with no-flux boundary conditions applied at the beginning and the end of the fiber. Each cell had a length (L) of 100 μm , radius (a) of 11 μm , and was discretized into 10 elements with a Δx of 10 μm . Within the cell, ρ_i was set to 150 $\Omega\text{-cm}$. The elements connecting adjacent cells were modified to incorporate the gap junction resistivity (R_g), which was set uniformly throughout the fiber to a value of 1.5 $\Omega\text{-cm}^2$ (representing a well-coupled fiber) or 100 $\Omega\text{-cm}^2$ (representing a poorly coupled fiber). $R_{g\text{eff}}$ was calculated as $R_g / (f_i \Delta x)$. For this validation study, only three values of ρ_{oeff} were tested: 0.5 (nominal value), 2.5, and 10 $\text{k}\Omega\text{-cm}$.

The conduction velocities and maximum upstroke velocities measured in well-coupled ($R_g = 1.5 \Omega\text{-cm}^2$) and poorly coupled ($R_g = 100 \Omega\text{-cm}^2$) ADMD fibers with ρ_{oeff} equal to 0.5, 2.5 and 10 $\text{k}\Omega\text{-cm}$ were compared to values obtained using the discrete bidomain model. In the well-coupled fiber, the conduction velocities and maximum upstroke velocities measured using the ADMD model were within 1% of the values obtained using the discrete bidomain model. In the poorly coupled fiber, the percent difference between the maximum upstroke values remained below 1%; however, the percent difference between the conduction velocities measured in the ADMD model and discrete bidomain models increased to 5%. As shown in Tables 3.1 and 3.2, the percent difference between the ADMD model and the discrete bidomain models for a fiber with a given level of coupling remained essentially the same as ρ_{oeff} increased. Because of the relatively small difference between the ADMD model and the discrete bidomain, the consistency in the percent error for a given level of coupling, and the speed of

computation, the ADMD model was used throughout this study to investigate the effect of increased ρ_{eff} on action potential propagation in both well-coupled and poorly coupled fibers.

Table 3.1: Comparison of conduction velocities (CV) measured in the 1-D approximate discrete monodomain model (ADMD) and discrete bidomain (BD) models

R_g ($\Omega\text{-cm}^2$)	1.5 (Well-Coupled)			100 (Poorly-Coupled)		
ρ_{eff} ($k\Omega\text{-cm}$)	0.5	2.5	10	0.5	2.5	10
<i>BD: CV (cm/s)</i>	36.01	18.83	9.68	5.44	5.13	5.07
<i>ADMD: CV(cm/s)</i>	35.71	18.66	9.60	5.18	4.86	4.82
<i>% Difference</i>	0.83	0.90	0.83	4.8	5.3	4.9

Table 3.2: Comparison of maximum upstroke velocities V_{max} measured in the 1-D discrete monodomain (ADMD) and discrete bidomain (BD) models

R_g ($\Omega\text{-cm}^2$)	1.5 (Well-Coupled)			100 (Poorly-Coupled)		
ρ_{eff} ($k\Omega\text{-cm}$)	0.5	2.5	10	0.5	2.5	10
<i>BD: V_{max} (cm/s)</i>	221	214	216	347	308	238
<i>ADMD: V_{max}(cm/s)</i>	219	212	214	344	309	238
<i>% Difference</i>	0.90	0.93	0.93	0.86	0.30	0

Two-Dimensional Tissue Structure

To explore the effect of specific components of cell architecture on electrophysiological properties, we constructed three subgroups of two-dimensional (2-D) models that represent cardiac tissue as groups of myocytes interconnected through discrete gap junction resistances. All of the tissue models are shown in Figure 3.1A-H.

The first subgroup consists of tissue models with varying degrees of overlap between cells in neighboring rows. In the uniform (UN) model (Fig 3.1A), the myocytes are represented as rectangular boxes, have uniform length and width, and are stacked directly on top of each other. In the brick wall (BW) model (Fig 3.1B), the myocytes are

represented as rectangular boxes, have uniform widths and uniform lengths (except at the borders) and have overlap in a pattern similar to a brick wall. In the random brick wall (RBW) model (Fig 3.1C), the myocytes are represented as rectangular boxes, have uniform widths but variable lengths and have overlap.

The second subgroup consists of tissue models with jutting at the cell ends. The uniform model with jutting (UNJ) (Fig 3.1D) and the random brick wall model with jutting (RBWJ) (Fig 3.1E) are similar to the (UN) and (RBW) models, respectively, except that the myocytes have a regular stairstep pattern of jutting at the cell ends.

The third subgroup consists of tissue models with randomly shaped cells and varying degrees of transverse coupling. In the random (RAND) model (Fig 3.1F), each myocyte is represented as a random stairstep unit with irregular jutting at the cell borders. Both the length and width of the cells are varied, and the myocytes are stacked in a semi-brick wall configuration. This model is defined having normal structural discreteness. Additional heterogeneity was added to the RAND model by removing a certain percentage of the transverse connections between the cell-cell lateral borders(Fig 3.1G-H).

The 2-D RAND model was generated by first creating a basic resistor grid composed of uniformly sized cells with an average length and width that was specified by the user. Each cell was further subdivided into subelements that were either $8\ \mu\text{m} \times 8\ \mu\text{m}$ or $10\ \mu\text{m} \times 10\ \mu\text{m}$ in size. The elements at the ends and along the lateral edges of the

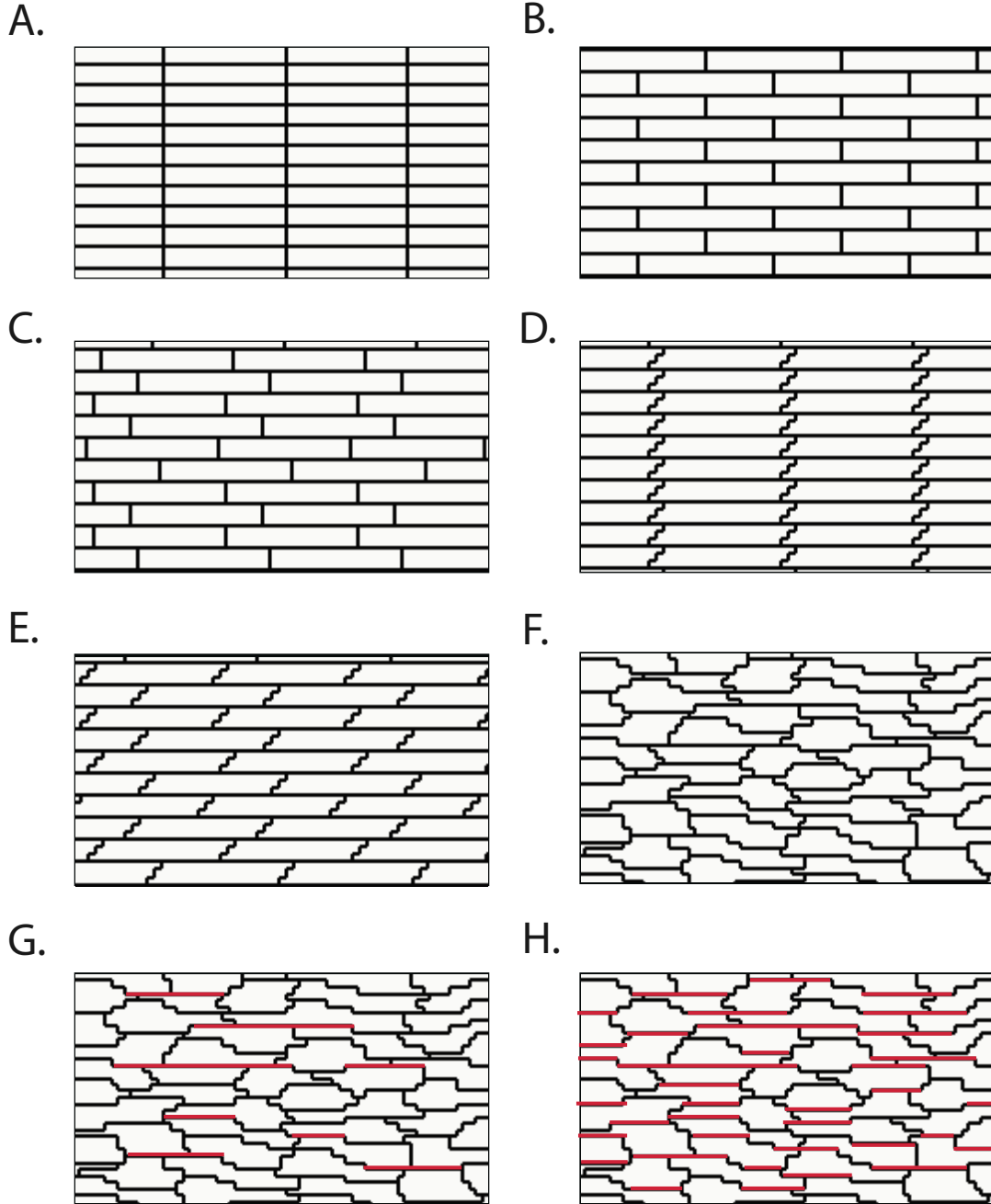


Figure 3.1: Tissues with varied cell arrangements. A - Uniform Model (UN); B - Brick Wall Model (BW); C - Random Brick Wall Model (RBW); D - Uniform model with jutting at cell ends (UNJ); E - Random Brick Wall model with jutting at cell ends (RBWJ); F-Random model (RAND); G-Random model with 50% structural discontinuity (RANDwSD50); H - Random model with 100% structural discontinuity (RANDwSD100). The red lines represent structural discontinuities.

cells were individually perturbed in order to randomly vary the shape of the cell. The myocyte shapes were generated randomly and are only an approximation of cell shapes that may occur in ventricular cardiac tissue. The discrete gap junctions connecting myocytes together were distributed in patterns observed experimentally in neonatal and adult cardiac tissue(104).

Two-Dimensional ADMD Model

One of the main reasons for using a monodomain model in which the intracellular properties are modified to account for the interstitial space is so that we can extend our studies to larger scale models of cardiac tissue where computation time is more of an issue. Similarly to the 1-D case, the effect of increasing the effective interstitial resistivity was incorporated into the 2-D microstructural model by increasing the effective intracellular resistivity of each cell. Figure 3.2 shows a visual representation of the discrete bidomain model and the approximate discrete monodomain model.

The governing equation for the 2-D ADMD can be discretized as follows:

$$\left[\frac{D_x^{i+1/2,j}(V_{i+1,j} - V_{i,j}) - D_x^{i-1/2,j}(V_{i,j} - V_{i-1,j})}{\Delta x^2} \right] + \left[\frac{D_y^{i,j+1/2}(V_{i,j+1} - V_{i,j}) - D_y^{i,j-1/2}(V_{i,j} - V_{i,j-1})}{\Delta y^2} \right] = \beta' I_m \quad (22)$$

$$I_m = I_{ion} + C_m \frac{dV_{i,j}}{dt} \quad (23)$$

The diffusion coefficient in the longitudinal direction between nodes $(i+1,j)$ and (i,j) is defined as $D_x(i+1/2,j)$ and the diffusion coefficient in the transverse direction between nodes $(i,j+1)$ and (i,j) is defined as $D_y(i,j+1/2)$. As in the 1-D case, the diffusion coefficients are inversely related to ρ_{ieff} and ρ_{oeff} . The effective extracellular resistivities were assumed to be the same in both the longitudinal and transverse directions.

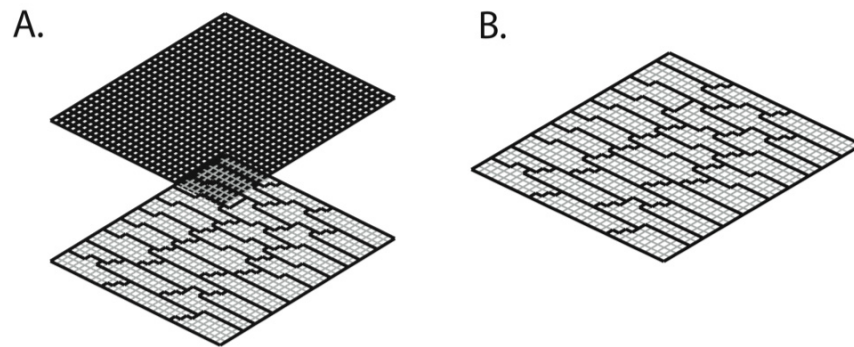


Figure 3.2: Visual representations of the (A) 2-D discrete bidomain and (B) the 2-D approximate monodomain model.

Validation of the 2-D Approximate Discrete Monodomain Models

A 0.50 cm x 0.06 cm (used during longitudinal propagation) and a 0.06 cm x 0.50 cm (used during transverse propagation) 2-D ADMD microstructural model were compared with discrete bidomain models that had the same intracellular structure and the same interstitial properties. Gap junctions were distributed evenly around the cell, and the intracellular resistivity was taken to be 150 Ω -cm. Longitudinal and transverse plane waves were generated in the BD and ADMD meshes by stimulating the cells intracellularly along the left border or the top border of the sheet, respectively, with a set of intracellular current pulses that were approximately 1.5-2 times threshold. In the case

of the bidomain, an equal and opposite stimulus was also given in the extracellular space.

Table 3.3: Comparison of conduction velocities (CV) measured in the 2-D approximate discrete monodomain model (ADMD) discrete bidomain (BD) models

<i>Well-coupled: $g_j=0.30 \mu S$</i>		
ρ_{oeff}	CV_L: BD/ADMD	CV_T: BD/ADMD
0.5	34.5/35.1 (0%)	23.4/23.1 (2%)
2.5	18.4/18.8 (2%)	15.9/15.7 (1%)
<i>Poorly coupled: $g_j=0.01 \mu S$</i>		
ρ_{oeff}	CV_L: BD/ADMD	CV_T: BD/ADMD
0.5	9.9/9.8(1%)	4.2/4.2 (0%)
2.5	9.3/9.0 (3%)	4.1 /4.1 (0%)

Table 3.4: Comparison of maximum upstroke velocities (V_{max}) measured in the 2-D approximate discrete monodomain model (ADMD) and 2-D discrete bidomain (BD) models

<i>Well-coupled: $g_j=0.30 \mu S$</i>		
ρ_{oeff}	V_{max,L}: BD/ADMD	V_{max,T}: BD/ADMD
0.5	210/211 (0%)	215/215 (0%)
2.5	210/211 (0%)	214/214 (0%)
<i>Poorly coupled: $g_j=0.01 \mu S$</i>		
ρ_{oeff}	V_{max,L}: BD/ADMD	V_{max,T}: BD/ADMD
0.5	320/319 (0%)	323/323 (0%)
2.5	274/275 (0%)	322 /322 (0%)

The conduction velocities and maximum upstroke velocities measured in well-coupled ($g_j = 0.30 \mu S$) and poorly coupled ($g_j = 0.01 \mu S$) ADMD tissue with ρ_{oeff} equal to 0.5 and 2.5 and were compared to values obtained using the discrete bidomain model. The conduction velocities and the maximum upstroke velocities measured using the ADMD model were within 3% of the values obtained using the discrete bidomain model. Because of the relatively small difference between the conduction velocities and

maximum upstroke velocities generated by ADMD model and the discrete bidomain and the speed of computation, the ADMD model was used throughout this study to investigate the effect of increased ρ_{eff} on action potential propagation in both well-coupled and poorly coupled tissue.

3.3 Details of Time Integration and Data Analysis

A semi-implicit Crank Nicolson scheme with a conjugate gradient solver was used to solve the system of partial differential equations(18, 42). In the monodomain simulations, the time step was kept constant at 5 μs , and output data was recorded every 10 μs . All simulations used the CardioWave software platform and were run in parallel using the Duke Shared Computer Cluster(84). Data analysis and visualization was done using MATLAB.

4. The Effect of Combined Microheterogeneity in the Interstitial and Intracellular Spaces on 1-D Propagation

4.1 Introduction

Pathological changes in myocardial architecture often create a heterogeneous substrate that supports abnormal electrical rhythms in the heart. In most cases, these architectural changes can be subdivided into two major categories: changes that occur in the intracellular space of the heart and changes that occur in the interstitial (extracellular) space. One of the most widely studied structural changes in the intracellular space involves the gap junction coupling between cells. A number of modeling and experimental studies have shown that changes in gap junction coupling can influence propagation speed, action potential waveshape, and the dynamics of sodium and calcium currents in the heart (40, 98, 104). In particular, lateral decoupling between cells has repeatedly been linked to slow conduction and conduction block, two properties that increase the likelihood of arrhythmia(19, 103).

Variation in myocyte size and shape is another source of heterogeneity in the intracellular space. In normal, healthy hearts, cell length and width can vary widely even among cells that are taken from a single source. Using 1-D discontinuous models, Henriquez and Plonsey have shown that changes in cell length alter features of action potential morphology such as the distribution of maximum upstroke velocity along the cell and the time constant of the action potential foot. Experimental and modeling studies by Spach et al. which compared conduction properties in small neonatal myocytes and larger adult myocytes have also shown that propagation speed and action potential waveshape are significantly affected not only by gap junction distribution but also cell size (40, 104). Myocyte hypertrophy caused by cardiac diseases such as heart failure and hypertension increases conduction velocity and may offset the effects of

decreases in intercellular coupling(120). The relative increases in cell length and width and the heterogeneity in cell size vary with the type of cardiomyopathy; however, very few modeling studies have systematically investigated the effect of cell size in conjunction with other microstructural changes that occur in cardiac disease (16, 31, 79).

In recent years, there have been several studies to explore another important but often-overlooked determinant of electrical propagation in the heart– the structure of the interstitial space(12, 28, 89, 104). Cardiac myocytes are surrounded by a heterogeneous interstitial space that contains a wide variety of components including ground substance, blood vessels, connective tissue, and collagen(8, 30). Even in healthy tissue, the electrical properties of the interstitial space vary non-linearly depending on the size and the composition of the interstitial region. Wide regions of interstitial space that contain porous collagen may have low resistances to current flow while narrow regions of interstitial space that primarily contain basement membrane and dense extracellular matrix proteins may have a very high resistance to current flow (69). Similarly to the intracellular space, changes in interstitial properties such as the resistivity of the space can also influence conduction velocity, action potential waveshape, and the dynamics of ionic currents(28, 38, 41).

As the relationship between structural remodeling and abnormal propagation observed in cardiac diseases such as atrial fibrillation has become more evident, several groups have turned their attention toward developing new therapies that reverse or limit the extent of structural remodeling(7, 33, 35). The successful application of these therapies may depend strongly on our fundamental understanding of how combined microscale heterogeneities in both the interstitial and intracellular spaces influence macroscale propagation in the heart(11, 12, 89, 127). In this study, we build upon previous modeling studies that have independently investigated the effects of interstitial

and intracellular microstructure in order to gain a better understanding of the combined effect of these intracellular and interstitial heterogeneities on electrical propagation.

4.2 Methods

4.2.1 Discrete Fibers with Uniform Structure

Propagation was first studied in four different fibers each of which was composed of cells of a given length:

Fiber with normal cells: 0.5 cm fiber composed of 50 cells, with cell length (L) equal to 100 μm

Fiber with short cells: 0.5 cm fiber composed of 100 cells, with cell length equal to 50 μm

Fiber with long cells: 0.6 cm fiber composed of 40 cells, with each cell length equal to 150 μm

Fiber with cells of various length: 0.5 cm fiber composed of 47 cells with a uniform distribution in length ranging from 50 to 100 μm , with an average length of 100 μm

No-flux boundary conditions were applied at the beginning and the end of the fiber. Each cell had radius (a) of 11 μm , and was discretized into subelements with a Δx of 2 μm . Within the cell, ρ_i was set to 150 $\Omega\text{-cm}$. The elements connecting adjacent cells were modified to incorporate the gap junction resistivity (R_g), which was set uniformly throughout the fiber to a value of 1.5 $\Omega\text{-cm}^2$ (representing a well-coupled fiber) or 100 $\Omega\text{-cm}^2$ (representing a poorly coupled fiber). R_{geff} was calculated as $R_g / (f_i \Delta x)$. The composition and size of the extracellular space may vary widely, particularly in the case of cardiac disease. With this in mind, ρ_{off} values between 0 and 25 $\text{k}\Omega\text{-cm}$ were tested in

order to capture the response of the fiber under both normal conditions and extreme conditions that may only occur sporadically throughout the heart.

Previous studies have shown that setting the discretization element (Δx) of the continuous fiber equal to the length of a single cell gives a good approximation to the discontinuous propagation observed in real cardiac tissue(98). In order to test the accuracy of continuous models when both the intracellular and interstitial resistivities are increasing, the conduction velocity measured using the ADMD model was also compared with the value measured using the highly-discretized and coarsely-discretized equivalent continuous models. The cellular resistivity used in the continuous models was calculated by lumping together the effective intracellular, gap junction and interstitial resistivities from the ADMD model. Resistor grids for the discrete bidomain (BD), approximate discrete monodomain (ADMD), and equivalent continuous monodomain models (CMD) are shown in Figure 4.1.

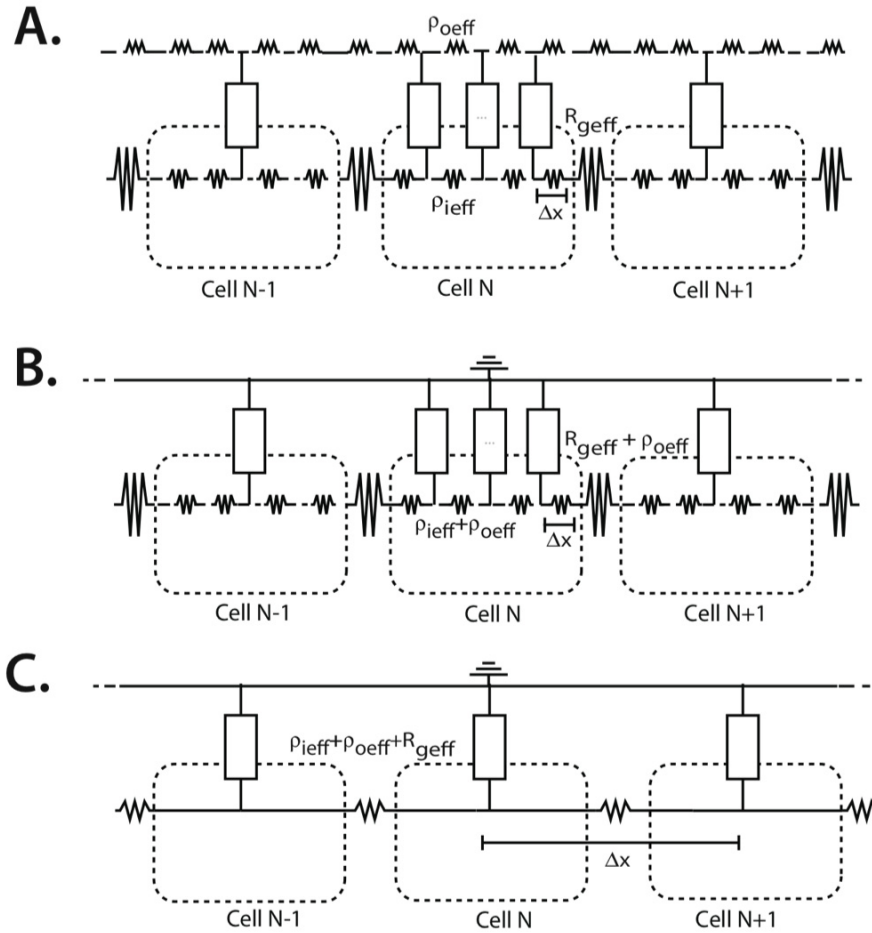


Figure 4.1: Resistor grids for (A) the 1-D discrete bidomain model (B) the 1-D approximate discrete monodomain model and (C) the 1-D approximate continuous monodomain model

4.2.2 Discrete Fibers with Heterogeneous Structure

The second goal of the study was to investigate action potential propagation in inhomogeneous 1-D fibers, which included abrupt changes in both intracellular and interstitial structure at a size scale larger than a single cell. As shown in Figure 4.2, heterogeneity was introduced into the intracellular space by uniformly increasing the

gap junction resistivity, $R_g(PC)$, in the first half of the fiber. Heterogeneity was also introduced into the interstitial space by increasing the ρ_{oeff} of the first half of the fiber to a value between 0.5 and 25 $\text{k}\Omega\text{-cm}$. In the second half of the fiber, all properties were set to normal values ($\rho_i=150 \text{ }\Omega\text{-cm}$, $R_g=1.5 \text{ }\Omega\text{-cm}^2$, $\rho_{\text{oeff}}=0.5 \text{ }\Omega\text{-cm}$). The cell length ($L=100 \text{ }\mu\text{m}$) and cell diameter ($a=11 \text{ }\mu\text{m}$) were kept constant throughout the fiber.

Measurements were taken for different combinations of interstitial resistivity and gap junction resistivity.

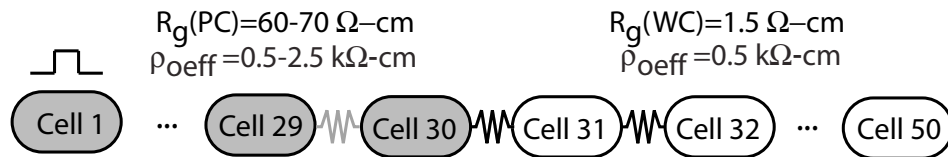


Figure 4.2: Representation of the 0.5 cm inhomogeneous fiber. The first half of the fiber (Cell 1- Cell 30), shown in gray, is poorly-coupled ($R_g=60\text{-}70 \text{ }\Omega\text{-cm}$) and the second half of the fiber, shown in white, is well-coupled ($R_g=1.5 \text{ }\Omega\text{-cm}$). ρ_{oeff} is varied between 0.5 and 2.5 $\text{k}\Omega\text{-cm}$ in the first half of the fiber and kept constant at 0.5 $\text{k}\Omega\text{-cm}$ in the second half of the fiber.

4.2.3 Premature Stimulation in a Discontinuous Heterogeneous Fiber

The third goal of the study was to determine the effect of increased ρ_{oeff} in the case of premature stimuli given at different coupling intervals. A second set of heterogeneous 1-D monodomain models were created by introducing a 0.4 cm long central zone of poorly coupled cells into a 1 cm long well-coupled fiber. The fiber was divided into individual cells of length $100 \text{ }\mu\text{m}$, and each cell was further subdivided into elements that were $10 \text{ }\mu\text{m}$ each. Gap junctions were modeled as individual resistors (R_g). The well-coupled(WC) region of the fiber was assigned an $R_g(WC)$ of $1.5 \text{ }\Omega\text{-cm}^2$, while the poorly-coupled (PC) region was uniformly assigned an $R_g(PC)$ of $60 \text{ }\Omega\text{-cm}^2$ or $70 \text{ }\Omega\text{-cm}^2$. No-flux boundary conditions were applied at the ends of the fiber.

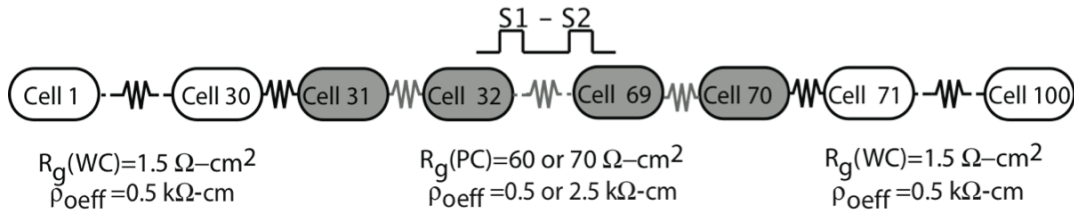


Figure 4.3: Representation of a 1-cm inhomogeneous fiber with a poorly-coupled central region.

4.2.4 Measurement and Stimulation Protocols

Single Stimulus

A single cell (LRd model) was paced to steady state at a basic cycle length of 1s. The steady state value of each state variable was then applied to each cell along the cable and served as the initial conditions. Action potentials were initiated by stimulating the fiber at the two leftmost nodes using a single stimulus that was approximately two times threshold. Conduction velocities were computed based on measurements taken at $x=0.20$ cm and $x=0.40$ cm. Intracellular delays (within the inside of cell) were computed by measuring the difference between the time the first node in the 41st cell reached -60 mV and the time the last node in the 41st cell reached -60 mV. Gap junction delay was measured as the difference between the time that the last node in 41th cell reached -60 mV and the first node in the 42st cell reached -60 mV. Maximum upstroke velocities were measured at the center of cell 21. The stimulus and boundary effects in the discontinuous fiber during depolarization were negligible at distances greater than 0.10 cm from the edges of the fiber. Consistent with the approach used by Shaw and Rudy, the amount of sodium charge generated during excitation was computed by summing the sodium current during the time interval defined by the maximum upstrokes of two neighboring cells (98). Safety factor was also measured using the method of Shaw and Rudy(98).

Premature Stimuli

Premature beats were generated in the central zone using an S1-S2 stimulus protocol. The first stimulus (S1) was generated by stimulating cell 51 with a stimulus that was 1.5 times threshold. The second stimulus (S2) was given at the same site and the same amplitude as the S1, and the S1-S2 coupling interval was varied from 200 ms to 3500 ms. Conduction delays at the boundary between the poorly-coupled central zone and the well-coupled region were measured by subtracting the difference in activation times (taken at $V_m = -50\text{mV}$) measured at the last node of the 69th cell and the first node of the 70th cell. The action potential duration was measured at 90% repolarization.

4.3 Results

Conduction Delays

In order to determine the effect of increased ρ_{off} on electrical loading at the microscale, we measured both the intracellular delay (within the cell) and the gap junction delay (between cells) in well-coupled and poorly coupled fibers with ρ_{off} ranging from 0 to 25 k Ω -cm.

As shown in Figures 4.4A and B, increasing ρ_{off} caused the ratio of intracellular delay to gap junction delay (IC/GJ Delay) to increase. In the well-coupled fiber, increasing ρ_{off} from 0 to 2.5 to 10 k Ω -cm caused the ratio to increase 30-fold. The largest ratio of intracellular to gap junction delay was observed in long cells. In the poorly coupled fiber, the increase in the ratio of gap junction to intracellular delay was much more dependent on the length of the cells. Long cells showed the steepest initial increase in the ratio of intracellular delay to gap junction delay as ρ_{off} was increased from 0 to 2.5 to 10 k Ω -cm, but the overall increase in the IC/GJ ratio in long cells was only 100-fold compared to 120-fold in shorter cells.

Increases in ρ_{oeff} were associated not only with an increase in intracellular delay, but a decrease in the gap junction delay, which also contributed to the increase in the IC/GJ delay ratio as shown in Figures 4.4B and C for the poorly-coupled fiber. In the poorly coupled fibers with $\rho_{\text{oeff}}=0$ k Ω -cm, the gap junction delay measured in the fibers with long cells was 150% larger than the gap junction delay measured in the fiber with short cells. As ρ_{oeff} increased, the gap junction delay decreased most rapidly in poorly coupled fibers composed of long cells. Increasing ρ_{oeff} from 0 to 2.5 k Ω -cm caused a 6% decrease in gap junction delay in fibers with short cells ($L=50\mu\text{m}$), but a 52% decrease in gap junction delay in fibers with long cells ($L=150\mu\text{m}$). At $\rho_{\text{oeff}}=10$ k Ω -cm, the gap junction delays measured in fibers of all cell sizes were within 10% of each other.

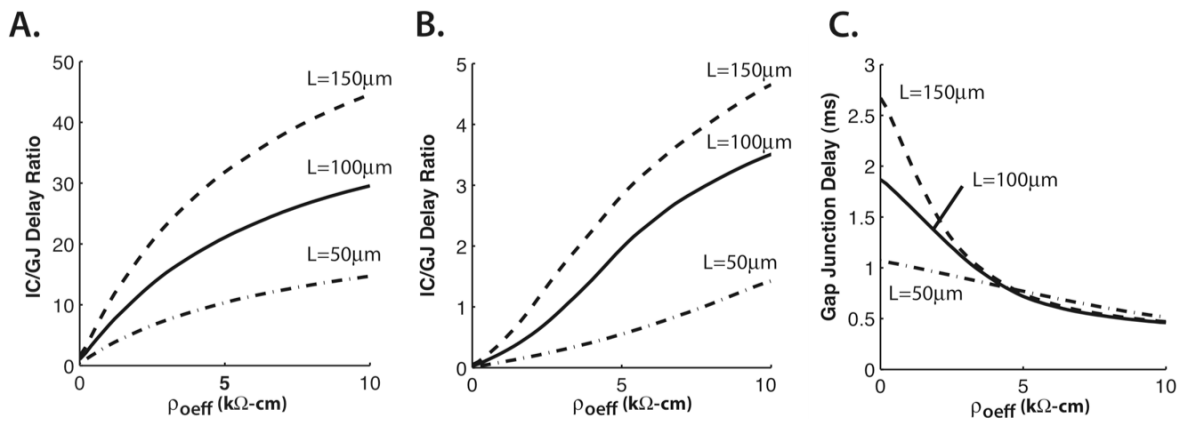


Figure 4.4: The ratio of intracellular to gap junction (IC/GJ) delay and gap junction delay as a function of ρ_{oeff} . IC/GJ Ratio shown for (A) well-coupled fibers and (B) poorly-coupled fibers composed of cells of different lengths, L . (C) Gap junction delay shown for poorly coupled fibers composed of cells of different lengths, L .

Conduction Velocity

The changes in the intercellular and gap junction delays with changes in ρ_{oeff} manifest themselves macroscopically as changes in the conduction velocity. Uniformly increasing ρ_{oeff} in the well-coupled fiber ($R_g = 1.5 \Omega\text{-cm}^2$, $L=100 \mu\text{m}$) from 0 to 2.5 to 10 $\text{k}\Omega\text{-cm}$ caused conduction velocity to decrease from 55.6 cm/s to 18.3 cm/s to 9.5 cm/s, an overall decrease of 83%. This decrease in conduction velocity followed the well-known relationship observed in highly discretized continuous fibers(47), $\theta = \sqrt{K/R}$, where K is a constant and R is the axial resistivity. In contrast, increasing ρ_{oeff} in the poorly coupled fiber caused the macroscopic conduction velocity to decrease more gradually and deviate from the square root relationship. When R_g was set equal to $100 \Omega\text{-cm}^2$, increasing ρ_{oeff} from 0 to 2.5 to 10 $\text{k}\Omega\text{-cm}$ caused conduction velocity to decrease slightly from 5.2 cm/s to 4.8 cm/s to 4.7, a decrease of only 10%.

In this study, additional simulations performed in fibers composed of long cells or short cells showed that fibers composed of long, poorly coupled cells ($R_g=100 \Omega\text{-cm}^2$) had higher conduction velocities and slower decreases in conduction velocity as ρ_{oeff} increased. Increasing ρ_{oeff} from 0 to 10 $\text{k}\Omega\text{-cm}$ caused a 14% decrease in CV in fibers with short cells ($L=50\mu\text{m}$), but a 6% increase in CV in fibers with long cells ($L=150 \mu\text{m}$). In the long, poorly-coupled fiber conduction velocity reached a plateau and increased slightly between $\rho_{\text{oeff}} = 5 \text{ k}\Omega\text{-cm}$ and $\rho_{\text{oeff}} = 10 \text{ k}\Omega\text{-cm}$. A detailed comparison of CV, intracellular delay, and gap junction delay in ADMD fibers composed of cells of different lengths is given in Table 4.1.

Table 4.1: Intracellular delay (IC Delay), gap junction delay (GJ Delay) and conduction velocity(CV) in ADMD fibers composed of cells of different lengths, L.

$R_g=1.5 \Omega\text{-cm}$				$R_g=100 \Omega\text{-cm}$			
$L=50 \mu\text{m}$				$L=50 \mu\text{m}$			
ρ_{oeff} ($k\Omega\text{-cm}$)	IC Delay (ms)	GJ Delay (ms)	CV (cm/s)	ρ_{oeff} ($k\Omega\text{-cm}$)	IC Delay (ms)	GJ Delay (ms)	CV (cm/s)
0	0.0373	0.0734	45.14	0	0.0127	1.0676	4.63
0.5	0.1036	0.0542	11.69	0.5	0.0510	1.0427	4.57
2.5	0.2471	0.0374	87.57	2.5	0.1147	0.9995	4.37
10	0.5051	0.0344	9.27	10	0.7357	0.5164	3.99
$L=100 \mu\text{m}$				$L=100 \mu\text{m}$			
ρ_{oeff} ($k\Omega\text{-cm}$)	IC Delay (ms)	GJ Delay (ms)	CV (cm/s)	ρ_{oeff} ($k\Omega\text{-cm}$)	IC Delay (ms)	GJ Delay (ms)	CV (cm/s)
0	0.0912	0.0885	55.64	0	0.0540	1.8672	5.20
0.5	0.2257	0.0586	35.18	0.5	0.2159	1.7498	5.08
2.5	0.5067	0.0377	18.36	2.5	0.8898	1.2027	4.78
10	1.0168	0.0344	9.51	10	1.6136	0.4602	4.73
$L=150 \mu\text{m}$				$L=150 \mu\text{m}$			
ρ_{oeff} ($k\Omega\text{-cm}$)	IC Delay (ms)	GJ Delay (ms)	CV (cm/s)	ρ_{oeff} ($k\Omega\text{-cm}$)	IC Delay (ms)	GJ Delay (ms)	CV (cm/s)
0	0.1503	0.0954	61.05	0	0.1252	2.6723	5.35
0.5	0.3496	0.0602	33.72	0.5	0.4973	2.3903	5.19
2.5	0.7666	0.0375	18.65	2.5	1.7178	1.2845	4.99
10	1.5284	0.0343	9.60	10	2.1848	0.4695	5.65

The conduction velocities measured in the ADMD fibers were compared with the conduction velocities measured in a highly-discretized(ACMD2) continuous fiber and a coarsely-discretized continuous fiber(ACMDL). As shown in Figure 4.5A, the well-coupled fiber can be accurately represented using a continuous fiber. This is consistent with previous studies which have shown that the differences measured between the well-coupled discontinuous and highly discretized continuous fibers are minor (98). In the poorly coupled fiber, however, large differences in the resistivity of adjacent elements cause pronounced loading effects that are large enough to reduce the macroscopic conduction velocity to a much smaller value than predicted using an equivalent highly-discretized continuous fiber(40, 102). When $R_g = 100 \Omega\text{-cm}^2$ and $\rho_{\text{oeff}} = 0.5 k\Omega\text{-cm}$, the conduction velocity measured in the discrete fiber was almost 50%

smaller than the conduction velocity obtained using the highly discretized continuous fiber. This issue is often addressed in computational studies by modeling poorly-coupled tissue with a fiber that has a discretization length equal to the length of a single cell ($\sim 100 \mu\text{m}$) (98); however, as shown in Figure 4.5B, this approximation becomes less accurate as cell length increases and as ρ_{eff} increases.

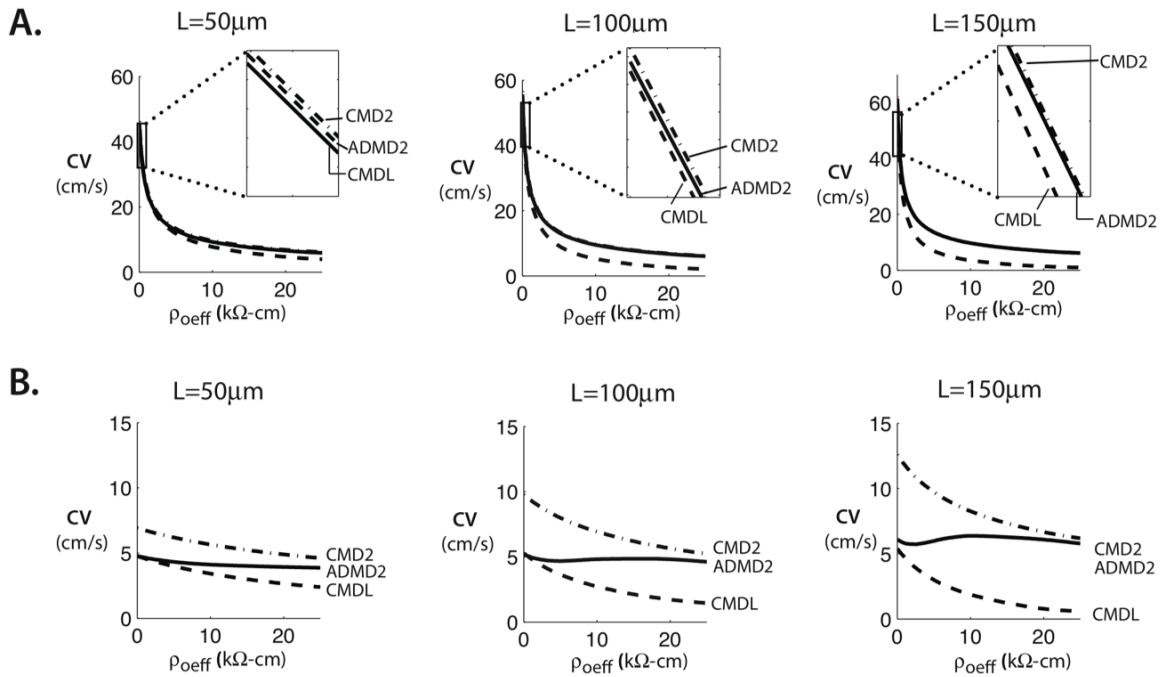


Figure 4.5: Plots of conduction velocity as a function of ρ_{eff} for (A) Well-coupled and (B) poorly-coupled fibers composed of cells of length L . In each graph, three different equivalent models are shown: CMD2: the continuous monodomain with $dx=2 \mu\text{m}$, ADMD2: the approximate discrete monodomain with $dx = 2 \mu\text{m}$, and CMDL: the continuous monodomain with $dx=L$.

Maximum Upstroke Velocity

In classical discrete fibers, changes in the gap resistance alter the rate of rise the action potential upstroke(98). Increases in ρ_{oeff} were also expected to modulate the action potential shape in both well and poorly coupled fibers. Figure 4.6A and 4.6B show that increases in ρ_{oeff} lead to an overall decrease in the maximum upstroke velocity (V_{max}) measured at the center of each cell in the ADMD model. The maximum upstroke velocity in both the well-coupled and poorly coupled ADMD fiber approached 207 V/s, the value measured in the highly discretized, CMD2 fiber.

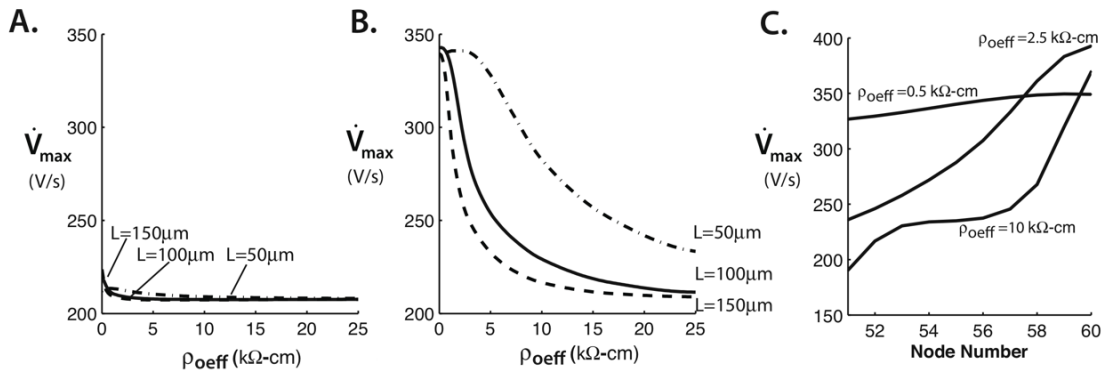


Figure 4.6: Maximum Upstroke Velocity at cell center as a function of ρ_{oeff} . Shown in (A) well-coupled and (B) poorly-coupled fibers composed of cells of different lengths, L . (C) Profile of maximum upstroke velocity within a single poorly-coupled cell with $L=100\mu\text{m}$ as a function of ρ_{oeff} .

The intracellular variation of the maximum upstroke velocity in the poorly coupled cell also changed as ρ_{oeff} increased (Figure 4.6C). At normal values of ρ_{oeff} , the variation of maximum upstroke velocity across the cell was approximately 30 V/s. As ρ_{oeff} increased, V_{max} measured at the center of the cell decreased as noted above; however, V_{max} at the beginning of the cell decreased while V_{max} at the end of the cell increased, which increased the variation in V_{max} across the cell to a maximum of 188 V/s. As ρ_{oeff} increased further, V_{max} across the entire cell eventually approached 207 V/s.

The change in upstroke velocity with increasing ρ_{oeff} depended on the length of the cell. Increasing ρ_{oeff} from 0 to 2.5 k Ω -cm caused a 1% increase in V_{max} in fibers with short cells ($L=50\mu\text{m}$), but a 25% decrease in V_{max} in fibers with long cells ($L=150\mu\text{m}$). In fibers composed of cells with varying lengths ranging from 50 to 100 μm , increasing ρ_{oeff} from 0.5 to 2.5 k Ω -cm decreased the mean maximum upstroke velocity across the fiber from $339\pm 12\text{ V/s}$ to $297\pm 50\text{ V/s}$, a 12% decrease in the mean and a 4-fold increase in the standard deviation. As ρ_{oeff} was increased further to 25 k Ω -cm, the mean maximum upstroke velocity and standard deviation decreased to $224\pm 35\text{ V/s}$.

Maximum Sodium Current

Simulations were also performed to investigate the effect of increased ρ_{oeff} on maximum sodium current ($I_{\text{Na,Max}}$) in well-coupled and poorly coupled fibers. As shown in Figure 4.7A, increasing ρ_{oeff} from 0 to 10 k Ω -cm in the well-coupled fiber caused maximum sodium current to increase slightly from $380\mu\text{A}/\text{cm}^2$ to $386\mu\text{A}/\text{cm}^2$. Increasing ρ_{oeff} from 0 to 10 k Ω -cm in the poorly coupled fiber caused maximum sodium current to increase from $351\mu\text{A}/\text{cm}^2$ to $386\mu\text{A}/\text{cm}^2$, an increase of 10%.

The intracellular variation of $I_{\text{Na,Max}}$ in the poorly coupled cell also changed as ρ_{oeff} increased (Figure 4.7C). At normal values of ρ_{oeff} the variation in $I_{\text{Na,Max}}$ across the cell was approximately $33\mu\text{A}/\text{cm}^2$. As ρ_{oeff} increased, $I_{\text{Na,Max}}$ measured at the center of the cell increased as noted above; however, $I_{\text{Na,Max}}$ at the beginning of the cell decreased while $I_{\text{Na,Max}}$ at the end of the cell increased which increased the variation in $I_{\text{Na,Max}}$ across the cell to a maximum of $120\mu\text{A}/\text{cm}^2$. As ρ_{oeff} increased further, the variation in $I_{\text{Na,Max}}$ across the cell gradually decreased to $0\mu\text{A}/\text{cm}^2$.

Note that as shown in Figure 4.7B, the poorly coupled fiber with long cells had the lowest initial $I_{Na,Max}$ but showed the steepest increase in $I_{Na,Max}$ as ρ_{eff} increased. In poorly coupled fibers composed of cells with varying lengths ranging from 50 to 150 μm , increasing ρ_{eff} from 0.5 to 2.5 $\text{k}\Omega\text{-cm}$ did not significantly change the mean $I_{Na,Max}$ across the fiber (350 $\mu\text{A}/\text{cm}^2$ versus 354 $\mu\text{A}/\text{cm}^2$ respectively) but increased the standard deviation in $I_{Na,Max}$ from 9 to 30 $\mu\text{A}/\text{cm}^2$, a 3-fold increase. As ρ_{eff} was increased further, the mean $I_{Na,Max}$ increased by as much as 6%, and the standard deviation in $I_{Na,Max}$ gradually began to decrease. Short cells showed a delayed response to changes in ρ_{eff} which led to a slight reduction in the average maximum sodium current measured at $\rho_{\text{eff}} = 25 \text{ k}\Omega\text{-cm}$ in fibers with average cell length of 100 μm ($I_{Na,Max} = 378.0 \mu\text{A}/\text{cm}^2$) compared to fibers in which each cell was exactly 100 μm long ($I_{Na,Max} = 386.0 \mu\text{A}/\text{cm}^2$).

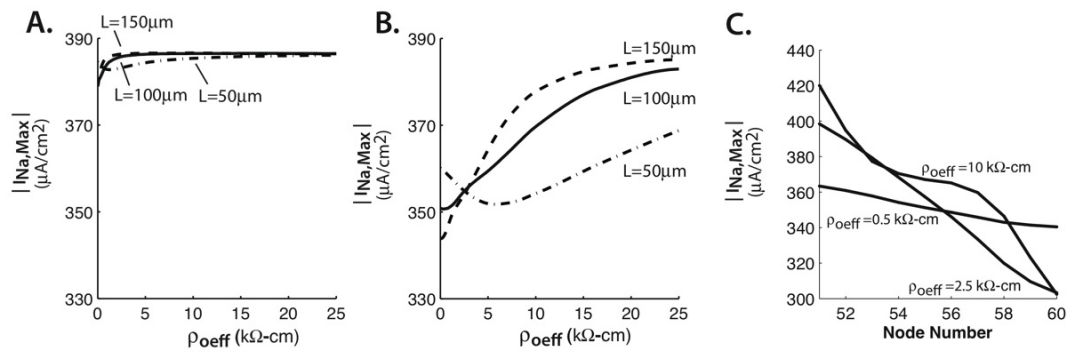


Figure 4.7: Variation in maximum sodium current as a function of ρ_{eff} . Shown in (A) well-coupled and (B) poorly-coupled fibers composed of cells of different lengths L . (C) Profile of maximum sodium current within a single poorly coupled cell with $L=100\mu\text{m}$ as a function of ρ_{eff} .

Safety Factor

The safety factor for conduction is determined by a number of factors including the membrane excitability and gap junction coupling(98). Simulations were performed to determine how other structural parameters such as ρ_{eff} and cell length influence

safety factor. In the well-coupled fiber, SF increased twofold from 1.61 to 4.55 as ρ_{oeff} increased from 0 to 10 k Ω -cm. In the poorly coupled fiber, SF increased from 2.92 to 4.52 as the ρ_{oeff} increased from 0.50 to 10 k Ω -cm. Figures 4.8A and 4.8B show safety factor as a function of ρ_{oeff} for well-coupled and poorly coupled fibers.

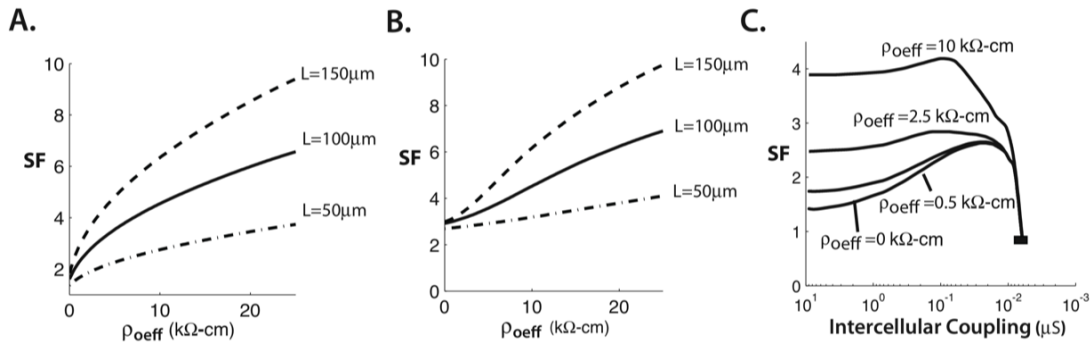


Figure 4.8: Safety Factor (SF) measured in a 1-D fiber as a function of ρ_{oeff} . Shown in (A) well-coupled fibers and (B) poorly coupled fibers. (C) Safety Factor measured as a function of both gap junction coupling and ρ_{oeff} .

Figure 4.8C is an alternate view of SF as a function of gap junction conductivity (g_j) for $\rho_{\text{oeff}} = 0, 0.5, 2.5$ and 10 k Ω -cm. Similar to studies by Shaw and Rudy which investigated safety factor in the $\rho_{\text{oeff}} = 0$ case, we found that that safety factor displayed biphasic behavior as g_j decreased. Increasing ρ_{oeff} caused an upward shift and a flattening of the SF versus g_j curve for all levels of coupling greater than 0.0013 μC (300 Ω -cm²). The effect of ρ_{oeff} on SF was greatest in well-coupled cells; increasing ρ_{oeff} did not influence safety factor in fibers with gap junction conductivities less than 0.0013 μS (R_g greater than 300 Ω -cm²) and did not prevent conduction block at $g_j=0.0061$ μS ($R_g = 621$ Ω -cm²).

Corresponding simulations performed in fibers composed of long cells and short cells showed that fibers with long cells had a much a higher safety factor than fibers with short cells. As shown in Figures 4.8A and 4.8B, the difference in safety factor between long cells and short cells increased as ρ_{oeff} increased.

1-D Heterogeneous Fiber

Several studies have shown that conduction can slow and eventually fail due to loading mismatches when a wavefront conducts from a poorly-coupled region to a well-coupled region (118). Simulations were performed to investigate whether increasing ρ_{oeff} could also influence the conditions for conduction block in a fiber with macroscopic heterogeneities in coupling. When ρ_{oeff} was set to a normal value of 0.5 k Ω -cm throughout the fiber, a long conduction delay and eventually conduction block occurred at the transition from the poorly-coupled region to the well-coupled region. As shown in Figures 4.9A and C, a transition delay occurred when gap junction resistivity of the first half of the fiber, $R_g(\text{PC})$, was increased from 1.5 Ω -cm² to 60 Ω -cm², and conduction block occurred when $R_g(\text{PC})$ was further increased to 70 Ω -cm². Wang and Rudy obtained a similar result in an earlier modeling study in which they used a traditional monodomain model to look at the effect of inhomogeneous coupling on action potential propagation(118).

When ρ_{oeff} of the fiber with $R_g(\text{PC}) = 60 \Omega$ -cm² was increased from 0.50 to 2.5 k Ω -cm as shown in Figures 8A and 8B, the conduction delay at the transition decreased from 1.4 ms to 0.10 ms. When ρ_{oeff} of the poorly-coupled fiber with $R_g(\text{PC}) = 70 \Omega$ -cm² was increased from 0.50 to 2.5 k Ω -cm as shown in Figures 4.9C and 4.9D, conduction was restored along the fiber. The improvement in conduction is due in large part to the increase in the sodium current at the transition boundary as ρ_{oeff} was increased (Figure 4.10A and 4.10C).

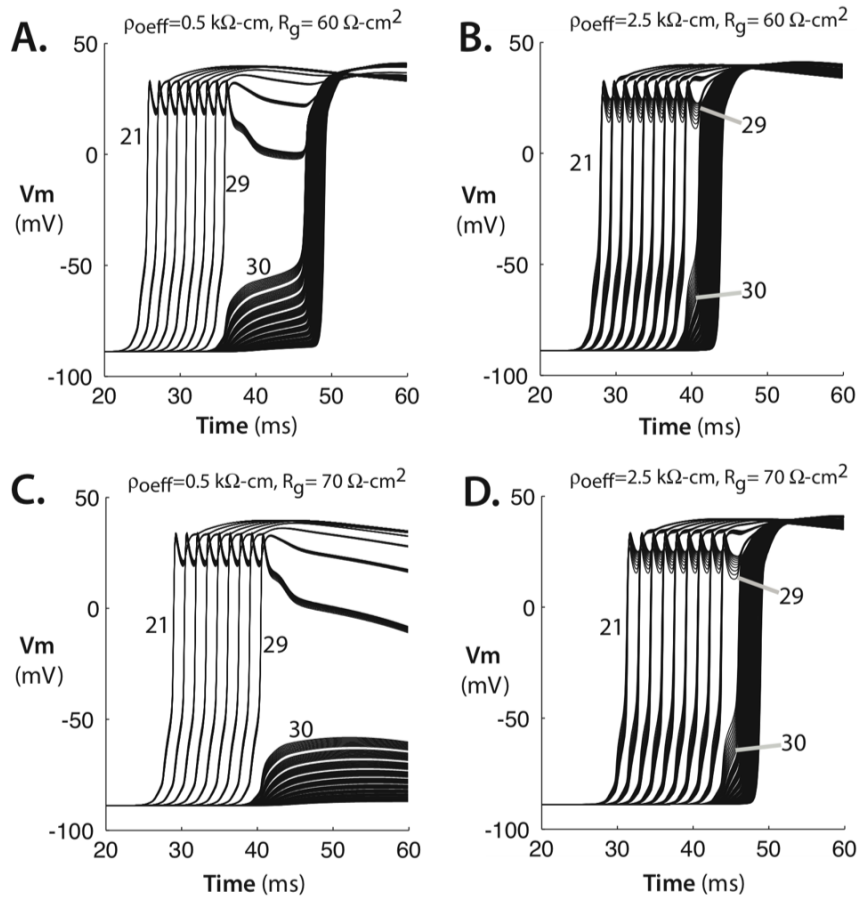


Figure 4.9: Conduction along inhomogeneous fibers with different combinations of R_g and ρ_{eff} . Top: (A) Conduction delay when $R_{g(\text{PC})}$ in the first half of the fiber was increased from to 1.5 to 60 $\Omega\text{-cm}$. (B) Reduced conduction delay when ρ_{eff} was also increased from 0.50 to 2.5 $\text{k}\Omega\text{-cm}$. Bottom: (C) Conduction block when $R_{g(\text{PC})}$ was increased from to 1.5 to 70 $\Omega\text{-cm}$. (D) Restored conduction when ρ_{eff} was also increased from 0.50 to 2.5 $\text{k}\Omega\text{-cm}$. The numbers shown indicate the cell number.

While it has been shown that increases in load caused by heterogeneous coupling can lead to increased dispersion of repolarization at the boundary between the poorly coupled and well-coupled regions(100, 113), increasing ρ_{eff} reduces the loading current during repolarization, thus reducing the dispersion of repolarization at the boundary between the poorly coupled and well-coupled region (Figure 4.10B and 4.10D).

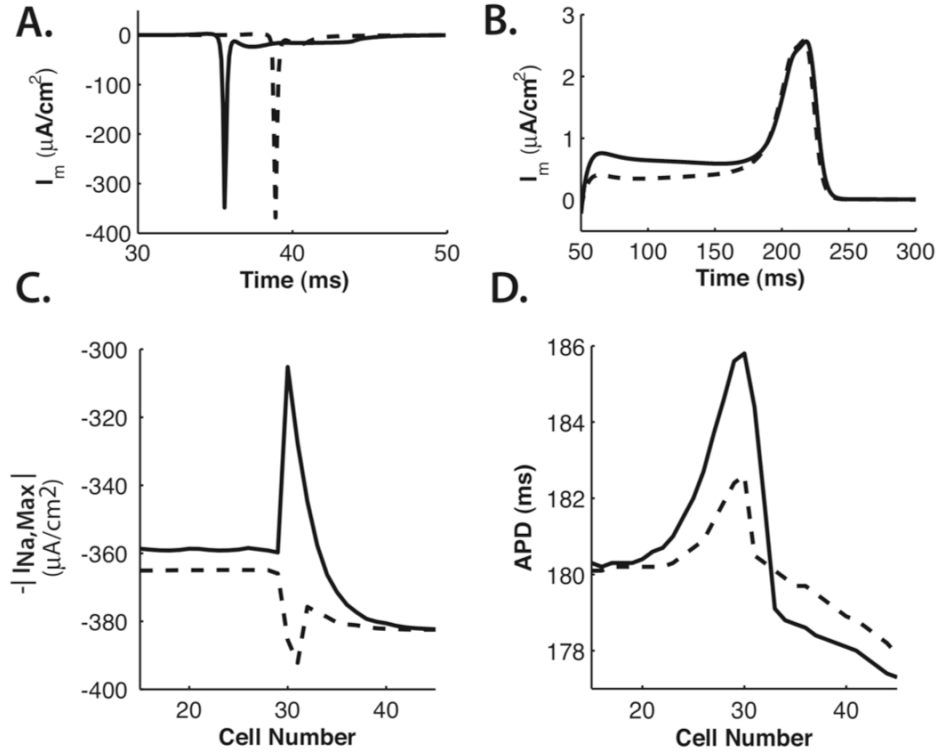


Figure 4.10: Membrane Current measured at Cell 29 in the inhomogeneous fiber with $R_g(\text{PC})=60 \Omega\text{-cm}$ during (A) depolarization and (B) repolarization. (C) Maximum Sodium Current and (D) Action Potential Duration measured along the inhomogeneous fiber. Solid Lines: $\rho_{\text{off}} = 0.5 \text{ k}\Omega\text{-cm}$, Dashed Lines: $\rho_{\text{off}} = 2.5 \text{ k}\Omega\text{-cm}$.

Premature Stimulation in a 1-D Heterogeneous Fiber

In this set of simulations, we looked at the effect of increased ρ_{off} on the escape of a single S1 action potential as well as a second S2 action potential from a poorly coupled region of tissue. In order to create a baseline for comparison, we first investigated the effect of the S1-S2 coupling interval on the conduction delay in a heterogeneous fiber with $R_g(\text{WC})=1.5 \Omega\text{-cm}^2$, $R_g(\text{PC})=1.5\text{-}63 \Omega\text{-cm}^2$, and $\rho_{\text{off}} = 0.5 \text{ k}\Omega\text{-cm}$. As expected, we observed that the conduction delay at the transition between the poorly coupled and well-coupled region became more pronounced as the gap junction resistivity of the poorly coupled region was increased. Conduction block occurred when $R_g(\text{PC})=64 \Omega\text{-}$

cm². We also observed that there was a local dispersion of repolarization at the boundary between the poorly coupled and well-coupled region. The APD profile for the case of $R_g=63 \Omega\text{-cm}^2$ is shown in Figure 4.11. The smaller peak at cell 51 is a response to the stimulus given within the cell. Steinhaus et. al have previously reported a similar effect of heterogeneous coupling on action potential duration(113). At the onset of block, the dispersion of repolarization at the boundary increased even further because the additional load from the well-coupled region drained current from the border cells during the plateau phase thus causing them to repolarize faster.

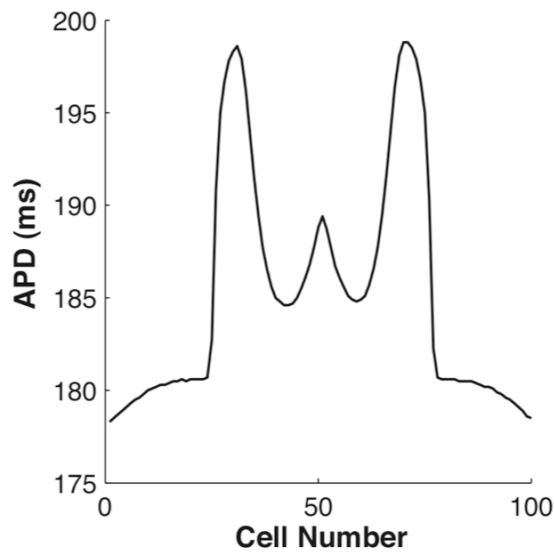


Figure 4.11: Action Potential Dispersion along the inhomogeneous fiber when $R_g(PC)=63 \Omega\text{-cm}^2$.

Even for the nominal case with $\rho_{\text{eff}} = 0.5 \text{ k}\Omega\text{-cm}$ and $R_g(PC)=60 \Omega\text{-cm}^2$, the combination of increased conduction delay and increased dispersion of repolarization (both of which were caused by structural heterogeneity alone) led to interesting results as the coupling interval between the S1 and S2 was decreased. As shown by the solid lines in Figure 4.12, intermediate decreases in the coupling interval led to a decrease in

the conduction delay measured between the poorly coupled and well-coupled regions of the fiber. In the case of the fiber with $R_g=70 \text{ } \Omega\text{-cm}^2$, intermediate reductions in the coupling interval restored conduction along the fiber. At very short coupling intervals (<250 ms), the conduction delay measured at the transition zone increased sharply from the minimum value.

Increasing ρ_{off} also reduced conduction delay and facilitated the escape of premature beats. In the fiber with $R_g=60 \text{ } \Omega\text{-cm}^2$, increasing the ρ_{off} of the central zone from 0.5 to 2.5 k $\Omega\text{-cm}$ reduced the delay at the transition between the well-coupled and poorly-coupled region in a coupling-dependent manner. As shown in Figure 4.12, the greatest decreases in delay occurred at very long (3500 ms) and very short (210 ms) coupling intervals, which showed decreases of 74% and 65% respectively. At intermediate coupling intervals (300-500 ms), the delay decreased by 57%. As shown in Figure 4.13B, increasing interstitial resistivity also reduced the APD dispersion at the boundary between the well-coupled and poorly coupled region from 6.5 mV to 2 mV.

In the fiber with $R_g(\text{PC})$ set to $70 \text{ } \Omega\text{-cm}^2$, increasing the effective interstitial resistivity to 2.5 k $\Omega\text{-cm}$ enabled action potentials generated at long intervals to escape from the poorly-coupled region. Increasing ρ_{off} also reduced the conduction delay for action potentials generated at intermediate and short coupling intervals by 58% and 28% respectively. Conduction block occurred at the transition zone when the coupling interval was reduced to 200 ms. Conduction block is indicated in Figure 4.13 with a star.

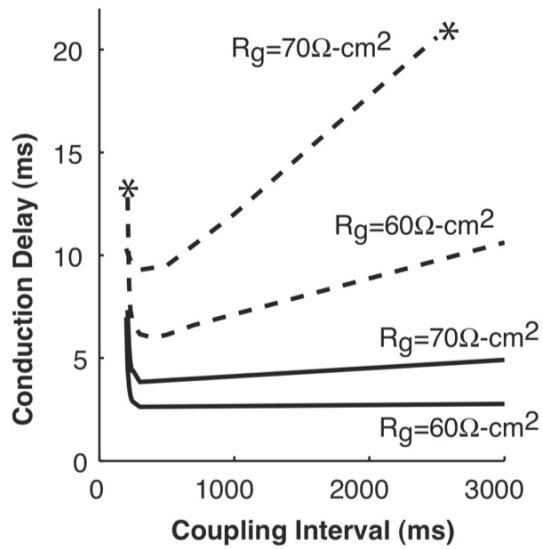


Figure 4.12: The conduction delay measured at the boundary between the poorly coupled and well-coupled region as a function of the coupling interval. *Dashed lines:* $p_{\text{eff}} = 0.5 \text{ k}\Omega\text{-cm}$, *Solid lines:* $p_{\text{eff}} = 2.5 \text{ k}\Omega\text{-cm}$.

4.4 Discussion

Previous studies on the effect of cardiac structure on propagation have focused primarily on either the effect of poor coupling or on the effect of a restricted extracellular space (91, 98). This study suggests that the combination of poor coupling and increased effective interstitial resistivity (caused by changes in interstitial volume or inherent material properties) may lead to paradoxical loading effects that enable slower, more continuous propagation at both the microscale and macroscale levels.

In the poorly-coupled fiber, the large value of the gap junction resistance combined with source-load mismatch between the intracellular and the gap junction regions leads to large conduction delays between cells; to a certain extent, however, the large value of the gap junction resistance also helps to isolate the cells and protect them

from the loading effects of neighboring cells. Increases in ρ_{eff} increase the ratio of intracellular to gap junction resistivity which initially increases loading effects but also reduces the additional charging delay caused by the mismatch between the gap junction resistance and the intracellular resistance. Long, poorly coupled cells experience greater loading effects at the cell boundaries than short cells because the gap junction has a lower relative contribution to the overall resistance of the cell and does not compensate for the source-load mismatch at the boundaries of the cell(40, 104).

This microscale changes in source-load mismatch caused by increased ρ_{eff} also affect macroscale measurements of conduction velocity, maximum upstroke velocity, maximum sodium current, and safety factor in poorly coupled tissue.

Conduction Velocity

As expected based on previous studies of the effect of a restricted extracellular space, this study showed that increasing the effective interstitial resistivity in well-coupled tissue slows the conduction velocity of the fiber(40, 92, 104). In the poorly coupled case, the interplay between the two factors influencing conduction velocity (overall increase in axial resistivity and reduced variations in spatial loading) led to paradoxical effects at the macroscale such as sustained or increased conduction velocity. This flattening of conduction velocity in response to increased extracellular resistivity is consistent with the findings of Cabo and Boyden(12). Because longer cells experience increased loading effects compared to shorter cells, they also have the most pronounced response to decreases in source-load mismatch as ρ_{eff} increases. This suggests that increased ρ_{eff} in anisotropic, multi-dimensional models may preferentially affect longitudinal rather than transverse conduction because the length of cells is much larger than the width. It is also important to note that as ρ_{eff} in the poorly coupled fiber

increases, neither continuous models with very small discretization lengths nor a continuous model with a discretization length equal to the length of a single cell accurately capture the behavior of the fiber.

Maximum upstroke velocity and Maximum sodium current

As ρ_{eff} increased, the maximum upstroke velocity measured at the center of the cell decreased while the available sodium current increased. This is in contrast to previous studies by Shaw and Rudy that have shown a biphasic increase in V_{max} and a decrease in available sodium current as the axial resistivity of fiber increases(98).

In the study by Shaw and Rudy, the axial resistivity is increased by increasing the gap junction resistivity and the fiber is modeled by lumping the intracellular and the gap junction resistivity into a single element with a $\Delta x=100 \mu\text{m}$ (the length of a single cell)(98). The increase in V_{max} was attributed to increased intracellular confinement of sodium current (decreased load) due to the large gap junction resistivity between adjacent cells (IC/GJ ratio <1). This confinement of sodium current also reduces the variation of maximum upstroke velocity across the cell. The decrease in sodium current observed in the Shaw and Rudy study as gap junction resistivity increased was attributed to dynamic inactivation of sodium channels during the long cell-to-cell delay.

In our study, the intracellular and gap junction resistivity are separated into discrete elements, and the axial resistivity is increased not only by increasing the gap junction resistivity but also by increasing ρ_{eff} in both the intracellular and gap junction regions of the cell. The increase in ρ_{eff} increases the ratio of the intracellular resistivity to gap junction resistivity, which increases the load from adjacent cells and the variation in maximum upstroke velocity and maximum sodium current at the boundaries of each cell. Because the center of the cell is more isolated from the changes in load at the

boundaries of the cell, both the measured value and the variation of maximum upstroke velocity measured in the center of the cells decreases as ρ_{oeff} increases.

In fibers with large ρ_{oeff} where the interstitial space is the dominant source of resistance in both the intracellular region and the gap region, the variation in maximum upstroke velocity and maximum sodium current across the cell becomes very small and approaches that observed in a highly-discretized continuous fiber. Uniform, highly-discretized continuous fibers do not show any spatial changes in maximum upstroke velocity or sodium current as the axial resistance changes (98). In an actual cardiac fiber, other factors that limit the amount of sodium channels in a given region may contribute to sodium channel inactivation as ρ_{oeff} increases(62).

Increased safety factor

As ρ_{oeff} increased, safety factor also increased (for $R_g < 120 \Omega\text{-cm}^2$) while maximum upstroke velocity decreased. This is contrast to the case of the discrete fiber, where increased axial resistivity is associated with increased safety factor and increased maximum upstroke velocity(98). This increase in SF is primarily due to the increase in maximum sodium current and the increase in current flowing into the cell from neighboring cells. For gap junction resistivities greater than $120 \Omega\text{-cm}^2$, increased ρ_{oeff} can no longer completely offset the sodium inactivation caused by slow cell-to-cell propagation, and, consequently, safety factor decreases.

Just as microscale variations in the intracellular and gap junction resistivity increase the likelihood of slow conduction and conduction block, mismatches in loading between well-coupled and poorly-coupled regions of tissue at the macroscale also contribute to slow conduction and conduction block in cardiac tissue. As shown in Figures 4.9 and 4.10, increasing ρ_{oeff} in poorly coupled regions of tissue homogenizes

variations caused by structural heterogeneity, reduces loading effects, and helps to delay the onset of conduction block. In diseased tissue characterized by reduced or abnormal membrane excitability, regional increases in ρ_{oeff} may also enable abnormal beats that are confined to a small, poorly-coupled region of tissue to escape and activate the surrounding tissue.

The Effect of Increased ρ_{oeff} during Premature Stimulation

The results of premature stimulation in the heterogeneous fiber suggest the presence of two different mechanisms that restore conduction at the transition between the poorly-coupled and well-coupled region. In the first mechanism, the interaction between the premature stimulus and the dispersion of repolarization reduces the difference in sodium current at the boundary between the well-coupled and poorly-coupled region and causes a curvature of $I_{\text{Na,max}}$ in the poorly-coupled region that can be observed in Figure 4.13A. This method of reducing loading is most effective at intermediate coupling intervals as evidenced by the gradual drop in the conduction delay for the fibers with $\rho_{\text{oeff}}=0.5 \text{ k}\Omega\text{-cm}$ (Figure 4.12). In the second mechanism, the increase in effective interstitial resistivity increases the available sodium current and reduces microscopic loading effects along the fiber. This reduces both the conduction delay and the dispersion of repolarization at the boundary between the well-coupled and poorly coupled region. Increased interstitial resistivity has the greatest effect at long and short coupling intervals where the APD dispersion at the boundary is less effective at reducing loading. Although these two mechanisms have competing modes of action (one mechanism decreases the total amount of available $I_{\text{Na,max}}$ while the other increases the total amount of available $I_{\text{Na,max}}$), they both reduce loading at intermediate coupling

levels which in turn increases the likelihood that a premature beat will escape from a poorly coupled region into surrounding well-coupled regions.

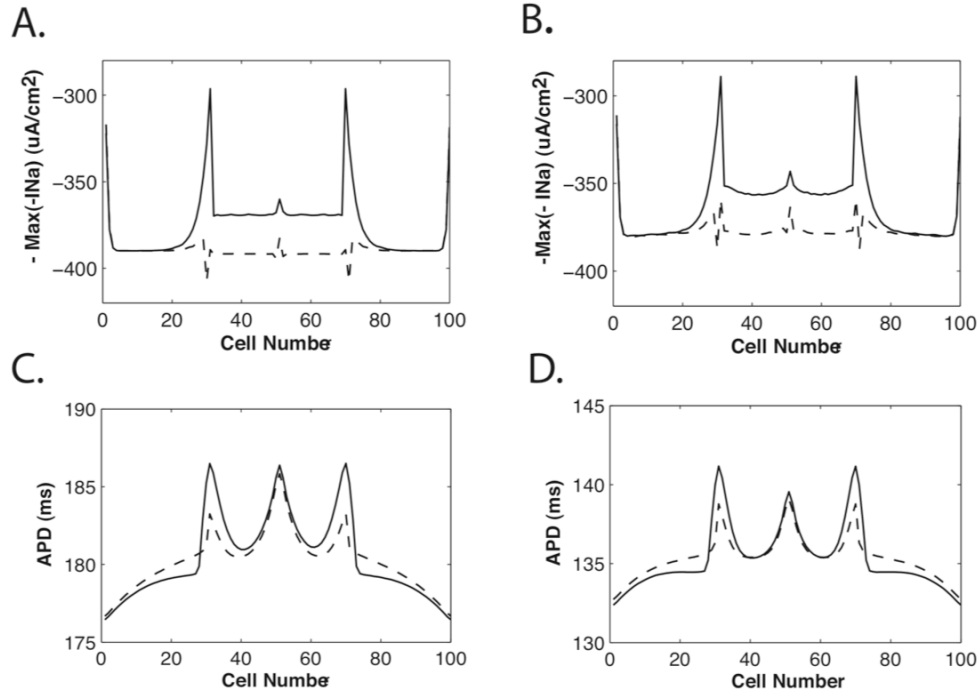


Figure 4.13: The maximum sodium current density (A,B) and the APD profile (C,D) in response to two consecutive stimuli (S1,S2), given in the poorly coupled region of an inhomogeneous fiber. *Solid lines:* $\rho_{oeff}=0.5$ k Ω -cm. *Dashed lines:* $\rho_{oeff} = 2.5$ k Ω -cm.

The results presented here are in agreement with other studies that have looked at the effect of heterogeneous coupling on conduction delay and APD dispersion; however, this study adds a new component in that it shows how heterogeneities in both the intracellular and interstitial space influence conduction delay and APD dispersion at the microstructural level even in the absence of ionic heterogeneity(100, 113). Similar to microstructural studies of conduction disturbances in atria done by Spach et al., this study suggests that variations in sodium current caused by both ionic and structural microheterogeneity may play a major role in the development of conduction abnormalities in cardiac tissue(108).

Although the 1-D model used in this study is a very simple and does not fully capture the complexity of propagation in the heart, it is nevertheless useful for understanding basic mechanisms of propagation and conduction failure. In subsequent chapters we will investigate how the delicate interplay between low intercellular coupling, dispersion of repolarization, and increased interstitial resistance at the microscale level influences complex activation patterns in the presence of a small rapidly firing focal source.

5. Intracellular Microheterogeneity in a Monolayer of Cardiac Myocytes

5.1 Introduction

Over the past few decades, experimental and modeling studies have established that electrical propagation in cardiac tissue is strongly influenced not only by ionic properties but also by myocardial architecture. As a result, an increasing number of new experimental therapies for cardiac disease have focused on restoring normal cardiac structure and function by implanting tissue constructs with controlled architecture or by administering drugs that target intercellular coupling(20, 22, 37). In order to gain a better understanding of the effect of myocardial architecture on impulse propagation in normal and diseased hearts, researchers have developed computer models of varying complexity that give a more realistic representation of cardiac structure.

One of the earliest developments in realistic modeling of cardiac structure was the shift from a continuous view that represents cardiac tissue as a fully connected medium to a discontinuous view that represents cardiac tissue as groups of cells that are only interconnected through low resistance pathways(109). Comparisons of one-dimensional (1-D) and two-dimensional (2-D) continuous and discontinuous model have shown that for high gap junction resistances, the discontinuous fibers and tissues behave very different than the continuous fiber(40, 98, 109). More recent, two-dimensional model of cardiac tissue which incorporate features of myocardial architecture such as variable cell shapes, overlap between cells, and jutting at cell borders have shown that variations in cardiac structure influence conduction properties in healthy tissue and may have a much stronger influence on ionic processes in tissues with low, heterogeneous cellular connectivity(104, 105).

Although a number of detailed computer models of myocardial architecture have been proposed, there has been no systematic comparison of these representations using a common framework. Consequently, questions remain about how various features of the architecture contribute to impulse propagation and, more importantly, how changes in the shape and interconnection of cells lead to conduction block and arrhythmia. This study investigates the role of four components of myocardial architecture, namely, brick wall tissue structure, jutting at cell ends, gap junction distribution and conductance along cell borders, and structural discontinuities (intercellular clefts), on longitudinal and transverse conduction velocity and action potential morphology.

5.2 Methods

5.2.1 Tissue Structure

As described in the methods chapter, we constructed three subgroups of two-dimensional (2-D) models that represent cardiac tissue as groups of myocytes interconnected through discrete gap junction resistances. All of the tissue models are shown in Figure 3.1A-H.

In summary, the first subgroup consists of tissue models with varying degrees of overlap between cells in neighboring rows: the uniform (UN) model (Fig 3.1A), the brick wall (BW) model (Fig 3.1B), and the random brick wall (RBW) model (Fig 3.1C).

The second subgroup consists of tissue models with jutting at the cell ends: The uniform model with jutting (UNJ) (Fig 3.1D) and the random brick wall model with jutting (RBWJ) (Fig 3.1E).

The third subgroup consists of tissue models with randomly shaped cells and varying degrees of transverse coupling: the random (RAND) model with normal structural discreteness (Fig 3.1F), the random model with 50% of transverse connection

between lateral borders removed (RANDwSD50) (Fig 3.1G), and the random model (RANDwSD100) (Fig 3.1H) with 100% of the cell=cell lateral borders removed. In the case of the RANDwSD50, the length of the intercellular clefts ranges from the length of one half of a cell (~77 μm) to the length of three cells (~432 μm).

The uniform and brick wall tissue models (UN, UNJ, BW, RBW, RBWJ) were 0.1728 cm x 0.1728 cm, contained 46,656 nodes and approximately 864 myocytes. The random models (RAND, RANDwSD) were 0.72 cm x 0.72 cm, contained 810,000 nodes, and approximately 15,000 myocytes.

5.2.2 Myocyte Representation

Each myocyte is divided into elements with length and width of 8 μm . Similar to the method of Spach et al., the membrane is represented as two parallel surfaces separated by an intracellular space with a depth of 11.3 μm (105). The nominal surface area is 128 μm^2 and was increased to 242 μm^2 to account for the irregular surface of the cell membrane. The average cell volume was 39,053 μm^3 , the average cell length was 144 μm and the average cell width was 24 μm . The myocyte shapes were generated randomly and are only an approximation of cell shapes that may occur in ventricular cardiac tissue.

5.2.3 Gap Junction Distribution

The discrete gap junctions connecting myocytes together were distributed in patterns observed experimentally in neonatal and adult cardiac tissue (24, 105, 106). In the neonatal gap junction configuration, punctuate gap junctions were spaced every 8

μm , and the cells were 100% coupled together at the ends of cells (end-to-end) and along the lateral sides of cells (side-to-side). In the adult gap junction configuration shown in Figure 5.1A, the cells were coupled end-to-end by plicate gap junctions in the longitudinal direction and by interplicate gap junctions in the transverse direction. This end-to-end region between myocytes is defined as the intercalated disk. The cells were randomly coupled along 15% of the side-to-side borders by combined plicate junctions. In this study, we also distinguish between end-to-end interplicates, which are located inside the intercalated disk, and side-to-side interplicates, which are located at the edge of the intercalated disk. The range of individual values of gap junction conductance used in this study (g_j : 0.01 – 1 μS) was consistent with values measured experimentally and with values used in other cellular models of cardiac tissue(106).

Histological and microscopy studies of healthy myocardium indicate that the interplicate regions of myocytes contain a larger percentage of gap junctional area, (~80%) and consequently have a larger conductance than the plicate regions(34, 48, 101). In most of the simulations this study, we assume that all gap junctions have the same conductance values; however, we also run a series of simulations in the RAND and RBW tissue structures to determine how the removal of different types of gap junctions ($g_j = 0$) affects propagation. The RANDwSD model (see Fig. 1G and 1H) is essentially a special case in which we remove a certain percentage of side-to-side interplicate gap junctions in order to simulate different levels of structural discontinuity that occur in cardiac disease. All results from these simulations were compared to a nominal case that had an adult gap distribution with all conductances set equal to 0.154 μS .

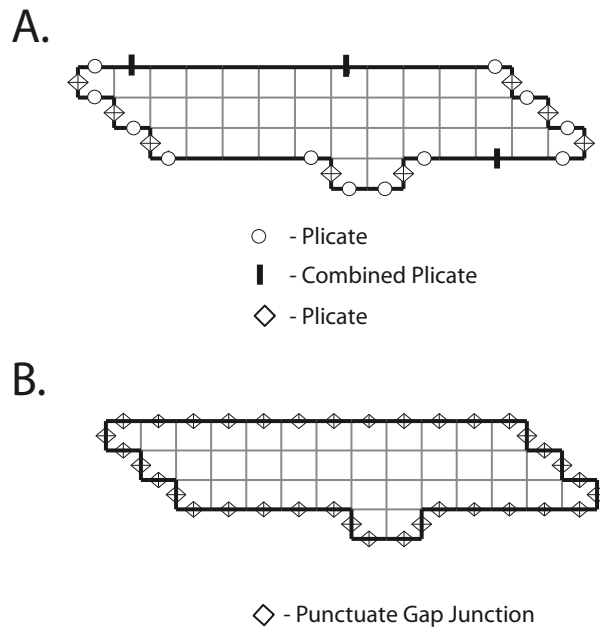


Figure 5.1: A segmented myocyte shown with (A) an adult gap junction distribution and a (B) neonatal gap junction distribution.

5.2.4 Membrane Properties

The membrane ionic currents (I_{ion}) were represented using LR1 dynamics(75), with modified calcium (d,f) kinetics. The sodium current, and consequently the action potential upstroke, was unchanged in the modified version. The maximum upstroke velocity in a membrane patch for both the original and modified models was 420 V/s.

5.2.5 Computational Details

Simulations were performed in each tissue structure (UN, UNJ, BW, RBW, RBWJ, RAND) for both neonatal and adult gap junction distributions for three different gap junction conductances: 0.01, 0.10, and 1 μ S. Longitudinal and transverse plane waves were generated by stimulating the cells along the left border or the top border of the sheet with a set of intracellular current pulses. In addition, a point stimulus was

generated in the RAND and RANDwSD models by applying intracellular current pulses to 110 nodes in a square region in the center of the sheet. All stimuli were 2 ms in duration and approximately 1.5-2 times threshold intensity.

Longitudinal upstroke velocities were calculated using membrane nodes along a line parallel to the longitudinal axis of the 2D sheet. Transverse upstroke velocities were calculated using membrane nodes along a line parallel to the transverse axis of the 2D sheet. Measurements in the 0.1728 cm x 0.1728 cm model were taken from points within the center of the tissue to minimize boundary effects and the effect of stimulus artifact. Conduction velocities in the random models were calculated from two membrane nodes that were 0.36 cm apart and at least 0.18 cm from the borders of the sheet.

This study uses a monodomain approximation that assumes that the conductivity of the extracellular medium is infinite. The time step was kept constant at 2 μ s, and output data was recorded every 10 μ s.

5.3 Results

5.3.1 Effect of brick wall tissue structure

Simulations were performed using the first subgroup of tissue models (UN, BW, RBW) to explore how the overlap of cells affects propagation. Table 5.1 summarizes the longitudinal and transverse conduction velocities and maximum upstroke velocities for UN, BW, and RBW tissue structures with gap junction conductances ($g_j = 0.01, 0.1, 1 \mu$ S) in both neonatal and adult gap junction distributions.

Neonatal Gap Distribution

When compared to the neonatal UN tissue model, the neonatal BW models show increased longitudinal conduction velocity and no significant change in transverse

conduction velocity. When gap junction conductance is large ($g_j = 1 \mu\text{S}$), the UN, BW, and RBW tissue models show little difference in either longitudinal or transverse conduction velocity.

The action potentials in the neonatal UN tissue models have larger maximum upstroke velocities for longitudinal propagation than for transverse propagation. In contrast, the action potentials in the neonatal BW and RBW tissue structures have maximum upstroke velocities that are higher in the transverse direction than in the longitudinal direction. As gap junction conductance increases, the difference between longitudinal and transverse maximum upstroke velocities decreases for all tissue structures.

Comparing the results from the first subgroup with the more realistic RAND model in the third subgroup shows that at low gap junction conductances ($g_j \leq 0.1 \mu\text{S}$), the action potentials in the RAND model have a lower longitudinal conduction velocity than the brick wall models (BW, RBW), but much higher than the UN model and have transverse conduction velocities that are slightly higher than in both the UN and BW models. The longitudinal maximum upstroke velocities are slightly higher than those in the BW case but lower than the UN case. The transverse maximum upstroke velocity is approximately the same in all of the models. At high gap junction conductances ($g_j = 1 \mu\text{S}$), however, the RAND case is comparable to the brick wall cases.

Adult Gap Distribution

When the gap junction distribution is switched from neonatal to adult, the longitudinal conduction velocity of the UN tissue model remains the same. The longitudinal conduction velocities in the BW and RBW tissue models decrease but are still larger than that observed in the UN tissue model. As expected, the reduced transverse coupling between cells slows transverse conduction velocities for all tissue

structures by as much as 70%. The BW and RBW tissue models have slightly higher transverse conduction velocities compared to the UN model.

When gap junction conductance is low, tissue structures with adult gap distributions have larger transverse maximum upstrokes than tissue structures with neonatal gap distributions. The BW and RBW models also have larger longitudinal maximum upstroke velocities. The largest differences between longitudinal and transverse maximum upstroke velocities occur in brick wall tissue models with mid-range gap junction conductances ($g_j = 0.1 \mu\text{S}$).

A comparison between the UN, BW, and RBW models and the RAND model shows that the RAND models have longitudinal conduction velocities that are slightly higher than both the UN and RAND tissue structures and longitudinal maximum upstroke velocities that are lower than the UN and brick wall models. As the gap junction conductance increases, the difference between the RAND and RBW longitudinal maximum upstrokes becomes almost negligible. The RAND tissue models have transverse conduction velocities that are 20-30% larger than observed in the UN, BW, and RBW models. At low gap junction conductances, the RAND models also have lower transverse maximum upstrokes than the UN, BW, and RBW models. Similarly to the brick wall models, the largest differences between the RAND longitudinal and transverse maximum upstroke velocities occur for mid-range gap junction conductances ($g_j = 0.1 \mu\text{S}$).

Table 5.1: Longitudinal and transverse conduction velocities (L/T) and maximum upstroke velocities (L/T) measured over a range of gap junction conductances (g_j) in tissues with various cell arrangements.

The bold entries are conduction velocities (cm/s) and all other entries are maximum upstroke velocities (V/s).

Neonatal Gap Junction Distribution			
	$g_j = 0.01 \mu\text{S}$	$g_j = 0.1 \mu\text{S}$	$g_j = 1 \mu\text{S}$
UN	7.0/5.1	35.9/17.9	66.5/46.1
	377/354	322/259	253/242
BW	18.2/5.1	49.6/17.9	67.7/46.1
	343/354	253/258	241/242
RBW	17.5/5.1	49.1/17.9	67.7/46.1
	338/354	245/259	241/242
UNJ	14.8/5.0	49.1/17.6	69.1/45.7
	374/351	273/258	244/244
RBWJ	20.0/5.0	53.0/17.7	70.2/45.5
	332/354	242/259	244/243
RAND	16.2/5.4	47.5/19.2	68.0/47.4
	357/350	257/262	243/243
Adult Gap Junction Distribution			
	$g_j = 0.01 \mu\text{S}$	$g_j = 0.1 \mu\text{S}$	$g_j = 1 \mu\text{S}$
UN	7.0/1.6	36.0/7.8	66.0/21.5
	378/370	322/310	246/234
BW	11.4/2.2	43.0/9.7	67.5/26.6
	372/371	272/296	245/240
RBW	11.4/2.1	43.7/9.7	67.5/26.6
	372/375	264/292	244/240
UNJ	14.8/2.1	49.1/9.2	69.7/25.4
	374/367	273/270	245/232
RBWJ	15.1/2.2	48.3/9.7	69.1/25.6
	363/373	253/290	244/240
RAND	13.7/3.5	44.3/13.6	67.5/33.7
	359/363	265/280	242/247

5.3.2 Effect of jutting at cell borders

Because the more realistic RAND model includes jutting at the end that is not seen in the more idealized models (UN, BW, RBW), simulations were performed in the second subgroup of tissue models (UNJ, RBWJ) in order to investigate the role of the stairstep interface. Table 5.1 also summarizes the longitudinal and transverse conduction velocities and maximum upstrokes for the UNJ, RBWJ tissue structures with gap junction conductances ($g_j = 0.01, 0.1, 1 \mu\text{S}$) in both neonatal and adult gap junction distributions.

The results show that tissue structures with jutting at cell ends (UNJ, RBWJ) have larger longitudinal conduction velocities than tissue structures without jutting (UN, RBW). The most significant increases occur in UNJ tissue models and in RBWJ tissue structures with reduced transverse coupling. In RBWJ models with adult gap junction distributions, jutting also slightly decreases longitudinal maximum upstroke.

To better analyze the effect of the coupling in and near the jutting region of the cell, the gap conductance was increased to a nominally normal value (i.e., $g_j = 0.154 \mu\text{S}$) to obtain more realistic propagation. Table 5.2 shows longitudinal and transverse conduction velocities and maximum upstrokes for the nominal case for the UN, RBWJ, and RAND tissue structures. The simulations showed that conduction velocity and waveshape were both affected when junctions were removed in the intercalated disc region.

Longitudinal conduction velocity in the RBWJ and RAND models decreases when plicate, end-to-end interplicate, or side-to-side interplicate gap junctions are removed from the tissue. When the plicate junction is removed from the UN tissue structure, longitudinal propagation blocks completely. Longitudinal propagation in brick wall structures, however, does not block when the plicate junction is removed,

since the interplicate junctions maintain coupling. Longitudinal maximum upstroke velocity increases in the RBWJ and RAND models when combined plicates, plicates, and side-to-side interplicates are removed. The most significant increases in longitudinal maximum upstroke velocities occur in the RBWJ and RAND models when both end-to-end and side-to-side interplicates are removed from the tissue. Longitudinal maximum upstroke jumps from 246 to 274 V/s in the RBWJ case and from 254 to 284 V/s in the RAND case.

Transverse conduction velocity in the UN, RBWJ, and RAND models decreases anywhere from 20-40% when the combined plicate is removed and approximately 40-50% when the side-to-side interplicates are removed. In the UN model, transverse conduction velocity decreases 5% when the plicate gap junction is removed. Transverse maximum upstroke velocity increases most significantly when side-to-side interplicate junctions are removed from the tissue. Transverse maximum upstroke velocity jumps from 277 to 326 V/s in the RBWJ case and from 267 to 298 V/s in the RAND case. In the UN model, transverse maximum upstroke velocity increases when the plicate gap junction is removed because there is no longitudinal current flow to adjacent cells. The largest differences between the longitudinal and transverse maximum upstroke velocities also occur when the side-to-side interplicate is removed; the RBWJ model has a 27% difference between the longitudinal and transverse maximum upstroke velocities (257 V/s and 326 V/s respectively).

Table 5.2: Longitudinal (L) and Transverse (T) conduction velocities and maximum upstroke velocities for various tissue structures which have adult gap junction distribution and gap junctions removed at select locations.

The bold entries are (L/T) conduction velocities (cm/s) and all other entries are (L/T) maximum upstroke velocities (V/s).

Gap Junction Conductance	UN	RBWJ	RAND
All $g_j = 0.154 \mu\text{S}$ (Nominal Case)	43.0/10.0 299/273	53.6/11.8 246/277	50.0/16.8 254/267
Combined Plicate = 0	43.0/6.4 299/313	53.0/9.6 251/291	49.7/15.2 255/272
Plicate = 0	block/9.6 block/291	44.3/12.0 251/283	39.6/15.0 269/275
End-to-End Interplicate = 0	N/A	48.5/11.9 246/281	47.9/16.4 257/271
Side-to-Side Interplicate = 0	43.0/6.8 299/301	51.4/6.0 257/326	43.2/10.2 271/298
Both Interplicates = 0	N/A	43.2/6.1 274/313	40.4/9.8 284/304

5.3.3 Effect of Lateral Decoupling on CV Ratio

The results in Table 5.2 suggest that the longitudinal conduction velocity is affected by the degree of transverse coupling depending on the degree of overlap. Simulations were performed in the third subgroup of randomly generated cells to investigate how lateral decoupling of cells, often seen in disease, affects propagation. Table 5.3 shows longitudinal and transverse conduction velocities and maximum upstrokes for the nominal case ($g_j = 0.154 \mu\text{S}$) with normal structural discontinuity and for the RANDwSD50 and RANDwSD100 tissue structures with increased structural discontinuity. Results are given for longitudinal and transverse plane wave propagation and point propagation.

Table 5.3 Longitudinal (L) and Transverse (T) conduction velocities (cm/s) and conduction velocity ratios (AR) for plane wave and point propagation in adult RAND, RANDwSD50 and RANDwSD100 tissue models.

Plane Wave Propagation		
	CV	AR
Normal	50.0/16.8	2.9
RANDwSD50	45.6/10.4	4.5
RANDwSD100	42.0/7.7	4.5
Point Stimulus		
	CV	AR
Normal	44.0/17.0	2.6
RANDwSD50	41.3/10.4	4.0
RANDwSD100	36.4/7.7	4.7

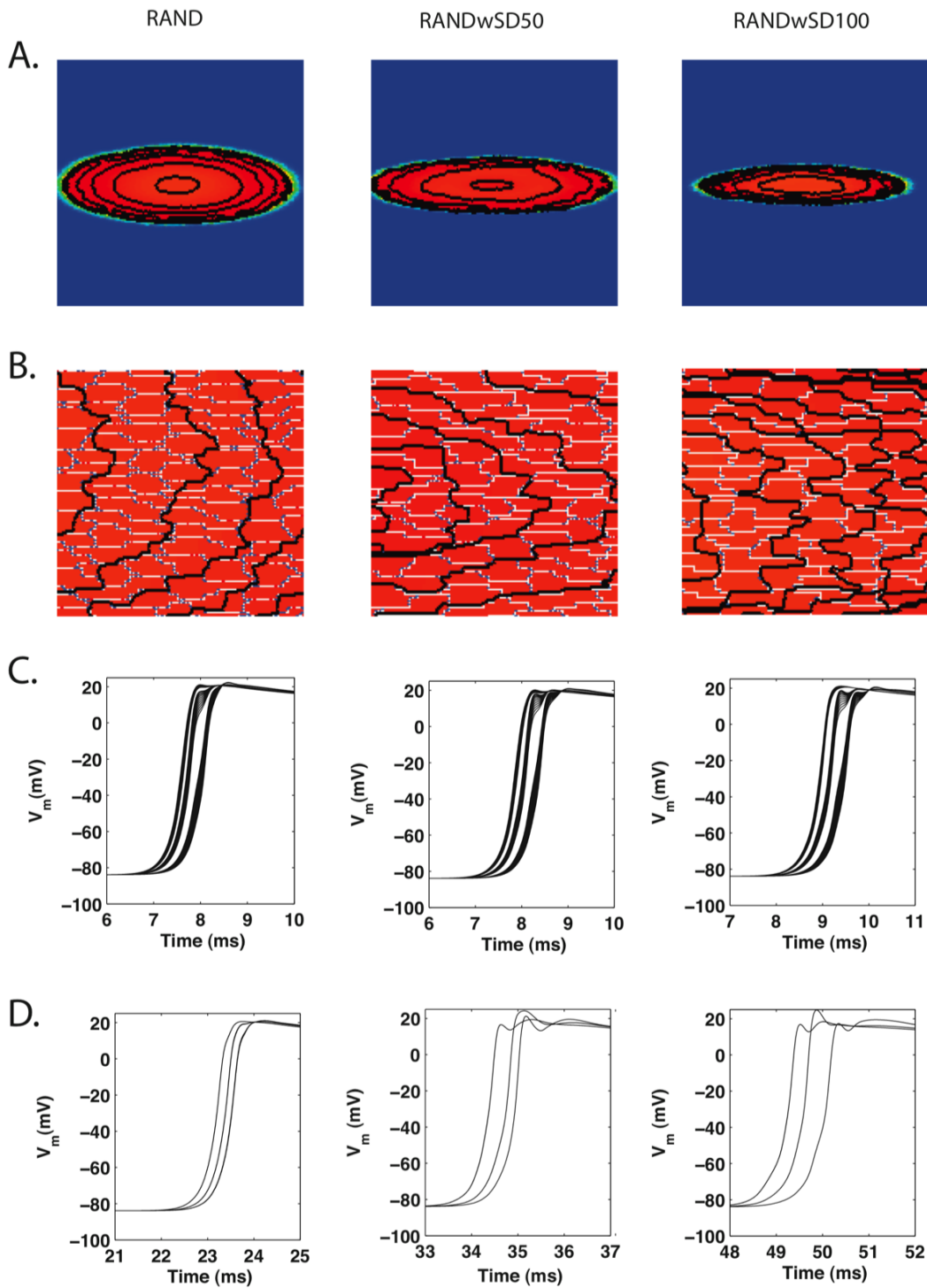


Figure 5.2: Activation maps(A,B) and action potentials propagating parallel to the longitudinal(C) and transverse (D) axes in response to a point stimulus given in tissues with varying levels of structural discontinuity.

When the amount of structural discontinuity in the tissue increases to 100%, longitudinal conduction velocity decreases from 50.0 cm/s to 42 cm/s, and longitudinal maximum upstroke velocity increases from 254 V/s to 278 V/s. Transverse conduction velocity decreases from 16.8 cm/s to 7.7 cm/s, while transverse maximum upstroke velocity increases from 267 V/s to 308 V/s.

Conduction velocity measured along the x (longitudinal) axis of the elliptic wavefront was 10-14% slower than longitudinal conduction velocity measured using plane wavefronts. In both cases, the ratio of longitudinal to transverse conduction velocities increases as structural discontinuity increases. The difference between the point and plane wave CV ratios, however, increases from 0.3 in the normal case to 0.8 in the RANDwSD100 case. Figure 5.2 shows that as the degree of structural discontinuity increases, the path of the wavefront becomes more tortuous, the shape of both longitudinal and transverse action potentials becomes more irregular, and the cell-to-cell activation delays become more pronounced.

To better illustrate the effects of lateral coupling on longitudinal propagation, a simulation was performed on the RBW model in which a single row of the brick wall cells was isolated from the rest of the tissue. When transverse current flow was eliminated, the longitudinal conduction velocity and maximum upstroke of the isolated fiber were identical to the UN case (Table 5.1). Figure 5.3 shows that fibers that are coupled together in a brick wall configuration have shorter cell-to-cell delays than fibers that are laterally isolated from neighboring fibers. The gap junction delay in the RBW tissue structure was 0.21 ms, while the gap junction delay in the isolated fiber was 0.27 ms.

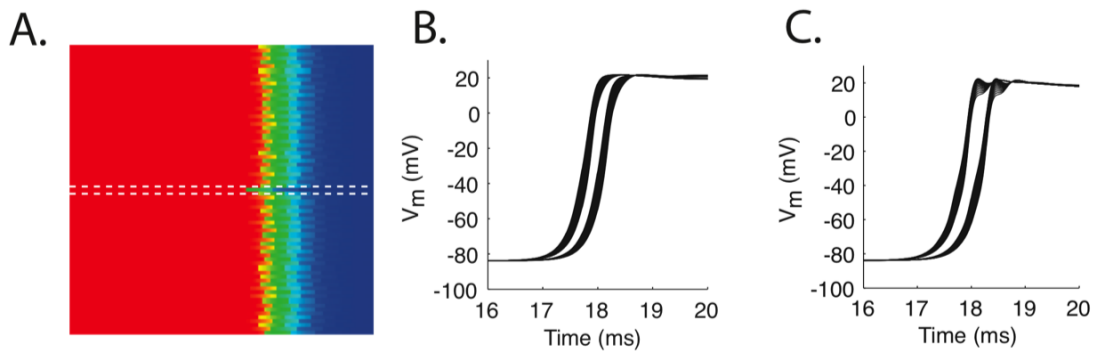


Figure 5.3: The effect of lateral decoupling on longitudinal propagation. (A) Longitudinal propagation in a brick wall tissue structure that has an isolated row of cells in the center. The white dotted line denotes the position of the isolated row of cells. (B) Example of action potentials from two cells in the brick wall portion of the tissue (C) Example of action potentials from two cells in the isolated row.

5.4 Discussion

This study illustrates how the complex myocardial architecture creates pathways of current flow that can significantly affect both longitudinal and transverse propagation. Table 5.1 shows that under conditions of low coupling, the longitudinal propagation in the BW model is much faster than in the UN model. The brick wall model used in this paper is structurally different than the parallel cable models used by other researchers in previous studies because it allows for current flow between rows of cells during longitudinal propagation. The parallel cable model corresponds more with the UN model in this study because they both incorporate interconnected cables (or rows of cells) with identical structures and do not allow transverse current flow during propagation of longitudinal plane waves(67, 68). Bursac et al. showed that in a monolayer of neonatal rat cells, decreasing lateral coupling by selectively engineering gaps between cardiac fibers reduced longitudinal conduction velocity when the conduction velocity ratio was greater than 3.5(10). Similarly to other studies, we have found that longitudinal propagation is slower for an elliptic wavefront than a plane wavefront. One explanation that has been proposed for this observation is that the

increased current load created by the steep curvature of the wavefront slows longitudinal conduction velocity(13). In general, the results suggest that conditions that reducing transverse coupling will slow longitudinal propagation, independent of changes in gap junction conductance.

As shown in Figure 5.3 the action potentials propagating in the decoupled fiber approach that seen in the uniform (UN) structure. Even when side-to-side connections are significantly reduced as in the case of the RANDwSD100 model, the tissue can still maintain a transverse conduction velocity of 6-7 cm/s. This is because the transverse wavefront is able to travel longitudinally and 'zig-zag' through the few side-to-side interconnections left in the cell. This 'zig-zag' conduction has been documented experimentally in studies of infarcted papillary muscles in the heart(19).

The simulations also showed that another structural feature that affects longitudinal propagation velocity is the jutting at the end of the cells. Jutting helps to (1) increase the number of interpicate gap junctions in the intercalated disk region and (2) increase overlap between rows of cells. Both of these factors help to increase longitudinal conduction velocity in the adult UNJ model ($g_j = 0.01 \mu S$) from 36.0 to 49.1 cm/s and to reduce longitudinal maximum upstroke from 322 to 273 V/s. The effect on transverse conduction is significantly less, increasing slightly or not at all in the UNJ and RBWJ structures. This may in part be due to the limited model of cell jutting we use in the UNJ and RBWJ models. The RAND tissue structure incorporates larger regions of jutting not only at the ends of cells but also along the lateral borders of the cell. The jutting along the lateral borders increases the number of side-to-side interpicate gap junctions and most likely accounts for the larger transverse conduction velocities in the RAND tissue structure. When jutting is added to the UN model, longitudinal conduction velocity becomes as large or larger than the longitudinal conduction velocity

in the RBWJ tissue model. A portion of this increase is caused by small amounts of overlap at the ends of cells. When the overlap is removed, the longitudinal conduction velocity in the adult UNJ model ($g_j = 0.1 \mu\text{S}$) decreases from 49.1 to 44.3 cm/s, thus indicating that even small amounts of overlap between cells can enhance longitudinal propagation.

In the various models studied, both types of interplicate gap junctions are important for determining longitudinal conduction velocity and maximum upstroke velocities of the action potentials. This is consistent with our earlier findings as well as experimental and modeling findings by Fast and Kleber that transverse current flow reduces cell-to-cell delay and thus facilitates longitudinal propagation, and is particularly important in poorly-coupled tissue (25). The transverse conduction properties are determined primarily by the number and distribution of combined plicate gap junctions and side-to-side interplicate junctions. The end-to-end interplicate gap junctions, however, seem to contribute very little to transverse propagation. This indicates that the distribution and orientation of gap junction plaques within intercalated disk region may play an important role in determining conduction velocity and maximum upstroke velocity.

One notable discrepancy between the adult RAND model and experimental observations in thin sections of adult cardiac tissue is the small difference (~5%) between longitudinal and transverse maximum upstroke. In comparison, experimental studies of healthy adult tissue have shown much larger directional differences of approximately 20-30%, and other microstructural modeling studies by Spach et. al have shown directional differences of approximately 12%(109). The simulation results presented here indicate that in a monodomain, the directional differences in maximum upstroke increase as the conduction velocity ratio increases, and the largest directional differences

in maximum upstroke occur in brick wall models with reduced side-to-side connections. It is important to note that the RAND tissue structure is only a hypothetical arrangement of a monolayer of cardiac cells, and it may be possible to increase directional differences in maximum upstroke velocities by increasing the brick wall overlap between cells, adjusting gap junction conductances within the intercalated disk, or reducing the percentage of side-to-side connections. Other factors have also been shown to affect the maximum upstroke. Henriquez and Plonsey showed that directional differences in maximum upstroke could also arise due to transverse loading in the tissue depth in the presence of an adjacent bath(41). Because cultures of adult cells with adult coupling are not yet feasible, it is unknown how large the differences might be in a true monolayer of cells compared to a tissue slice.

While the models considered in this study do not fully consider the effects of the interstitial space on electrical propagation in cardiac tissue and are perhaps more relevant to 2-D cardiac cell cultures, the simulations reveal that features of the myocardial architecture such as overlap and jutting help to enhance conduction when connectivity between cells is reduced. Although these features help to maintain impulse conduction from cell to cell, they can also enable slow, tortuous conduction that can increase susceptibility to cardiac arrhythmias. Future studies with these microstructural models will focus on the role that myocardial architecture in healthy and diseased tissue plays in determining the dynamics of more complicated patterns of electrical activation such as premature excitation and spiral waves.

6. The Effect of Tissue Microstructure on the Escape of Ectopic Beats

6.1 Introduction

Ectopic beats in the heart have been identified as a source of abnormal rhythms in both the atria and the ventricles. A landmark study by Haissaguerre et al. and subsequent studies by other researchers found that rapidly firing ectopic sources located in the atrial sleeves of the pulmonary veins are a primary driver of atrial fibrillation (AF) (52, 125). Ischemia-induced and reperfusion arrhythmias in the ventricles have also been correlated with the presence of ectopic sources as well as increases in interstitial resistivity and decreases in gap junction coupling that occur during the early stages of ischemia and a heterogeneous increase in gap junction coupling during subsequent reperfusion(57).

A number of research studies have shown that the pathological structural changes that occur in diseased cardiac tissue can facilitate both the formation of ectopic sources and the maintenance of widespread reentrant circuits. In particular, intracellular heterogeneity caused by local reductions in coupling has been shown to reduce the size of the focal source needed to initiate an ectopic beat and to influence the rate at which an ectopic focus fires(86, 96, 117, 122). While local reductions in coupling facilitate the formation of focal sources, the loading mismatches between the poorly-coupled and well-coupled areas often increase the likelihood of conduction block, which can make it more difficult for premature beats that originate in a poorly-coupled region to escape and propagate throughout the heart(118). Surprisingly, *in-vivo* studies seem to indicate that increasing gap junction coupling using novel pharmacological therapies such as rotigaptide is marginally effective at suppressing AF in a dogs with congestive heart failure and has no effect on the incidence of ventricular arrhythmias caused by

ischemia-induced focal activity, raising additional questions about how other factors such as pathological changes in the composition and size of the interstitial space of diseased atria affect ectopic behavior (99, 126). The interstitial space located near capillaries and veins may decrease in size and contain a disproportionate amount of resistive material such as basement membrane and extracellular matrix proteins compared to other regions, particularly during early stage ischemia or myocardial infarction(30). In the context of the pulmonary vein, the composition of the fibro-fatty plane separating the atrial cells located along the myocardial sleeve from the outer layer of the vein and the high elastic content of the fibrotic scarring in the PV may also influence the initiation and propagation of focal activity(95, 112).

In this chapter we use inhomogeneous 1-D and 2-D microstructural computer models to investigate how the interstitial space interacts with specific features of myocardial architecture such as cell arrangement and fibrosis to influence both the initiation of ectopic beats and the escape of ectopic beats from a poorly coupled region of tissue into surrounding well-coupled tissue. This study shows that in regions of tissue with significant source-load mismatch, variations in cell arrangement and effective interstitial resistivity at the size scale of single cells can lead to complex patterns of escape and reentry in tissue that would normally experience complete conduction block.

6.2 Methods

6.2.1 Ionic Model

The Luo Rudy dynamic model of guinea pig myocytes described in Chapter 3 was used to calculate the ionic current for the cells located in healthy regions of tissue that did not exhibit ectopic activity(74)

In all of the 1-D cases and several of the 2-D cases, the spontaneously active regions of tissue were modeled using a modified Luo-Rudy dynamic model (also

described in Chapter 3) that included a funny current based on the DiFrancesco-Noble model of human Purkinje cells. The pacing rate of the spontaneous cell was modulated by changing the conductance of the funny current, G_f . At $G_f=0.02 \text{ mS/cm}^2$, the spontaneous uncoupled cell fired at a pacing rate of 231 ms as shown in Figure 6.1.

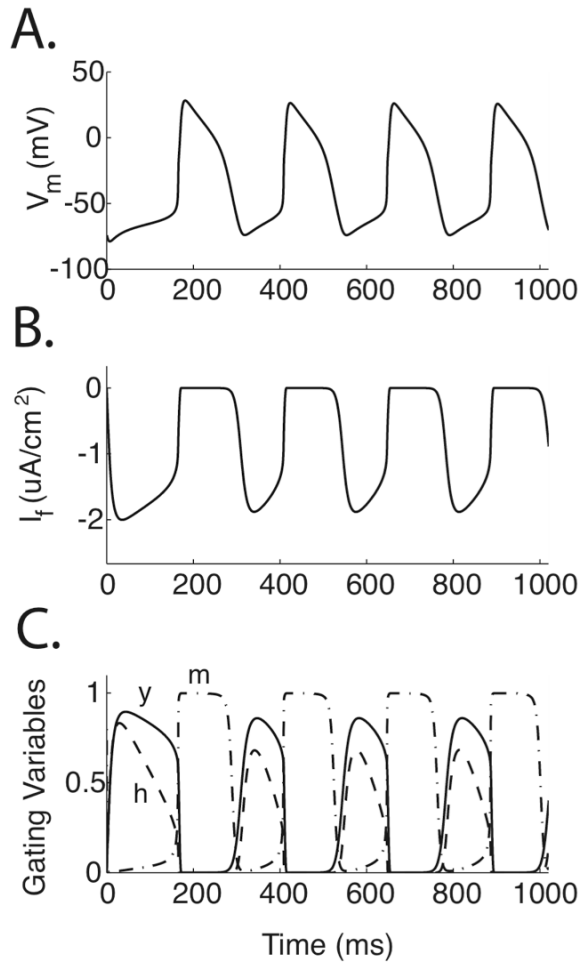


Figure 6.1: Plots of parameters related to the funny current. (A) Membrane voltage during spontaneous activation (B) Hyperpolarization-activated inward current, I_f (C) Selected gating variables: y , funny current; m and h , sodium current.

6.2.2 Structural Model (1-D)

The effect of intracellular and interstitial structure on the initiation and propagation of focal beats was explored using 1-D microstructural models of 2 cm long cardiac fibers. Similarly to the study in Chapter 3, an approximate discrete monodomain (ADMD) which lumped the interstitial and intracellular properties into a single space while preserving the discrete cellular structure was used to model the inhomogeneous 1-D cable.

As shown in Figure 6.2, heterogeneity was introduced into the intracellular space by uniformly increasing the gap junction resistivity, $R_g(PC)$, in a 1 cm center region of the fiber. Heterogeneity was also introduced into the interstitial space by increasing the ρ_{oeff} of the center region to a value between 0.5 and 25 $\text{k}\Omega\text{-cm}$. In the outer regions of the fiber, all properties were set to normal values ($\rho_i=150 \text{ }\Omega\text{-cm}$, $R_g=1.5 \text{ }\Omega\text{-cm}^2$, $\rho_{\text{oeff}}=0.5 \text{ k}\Omega\text{-cm}$). The size of the focal source needed to initiate a propagating action potential was measured as a function of R_g and ρ_{oeff} , and the ability of the beat to escape from the poorly coupled region to the well-coupled region was also recorded.

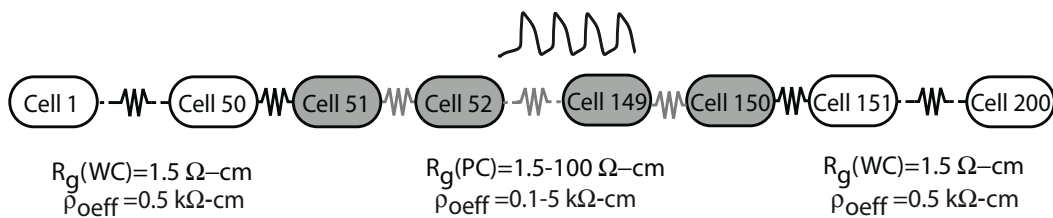


Figure 6.2: Representation of a 2 cm inhomogeneous fiber, with a 1 cm poorly coupled central region.

6.2.3 Randomly Generated Structural Model (2-D)

Similar to the 1-D case, the ADMD model was used to model the 2-D tissue structure. In the 2-D microstructural models, each myocyte was represented as a random stairstep unit with irregular jutting at the cell borders. The randomly generated meshes were 1 cm x 1 cm, and the average cell length and width were 100 μm and 30 μm respectively. Each myocyte was subdivided into elements with length and width of 10 μm . The discrete gap junctions connecting myocytes together were distributed in patterns observed adult cardiac tissue. In the more well-coupled tissue, longitudinal and transverse gap junctions were set equal to $g_j=0.10 \mu\text{S}$. A more detailed description of the two-dimensional structure is given in Chapters 3 and 4.

A 0.4 cm x 0.4 cm heterogeneous region in the center of the randomly generated ADMD model tissue was created by increasing all of the longitudinal and transverse gap junction conductivities, $R_g(\text{PC})$, to a single value between $g_j=0.1$ and $0.002 \mu\text{S}$ and increasing the ρ_{eff} of the center region to a single value between 0.5 and 2.5 $\text{k}\Omega\text{-cm}$. In the outer regions of the fiber, all properties were set to normal values ($\rho_i=150 \Omega\text{-cm}$, $R_g=1.5 \Omega\text{-cm}_2$, $\rho_{\text{eff}}=0.5 \text{k}\Omega\text{-cm}$). A schematic of this tissue is shown in Figure 6.3a. Fibrosis was introduced into both the center region and the surrounding tissue by randomly decoupling 40% of the lateral borders. To determine the sensitivity of the results to tissue parameters, several tissue models representing different realizations of the same microstructure statistics (cell shape, size, coupling, fibrosis etc.) were created.

6.2.4 Basic Structure Models (2-D)

Four inhomogeneous microstructural models (0.6cm x 0.6cm) that focused a specific component of cardiac architecture were created to investigate the effect of effective interstitial resistivity on regions of tissue with significant source-load mismatch. The first two tissue types were the uniform (UN) and brick wall (BW)

microstructural models described in Chapter 3. The second two tissue types were a brick wall model (BW_{Long}) composed of cells with increased length, $L=150\ \mu\text{m}$, and a brick wall model (BW_{Wide}) composed of cells with increased width, $W=40\ \mu\text{m}$. All four tissue types were compared with a corresponding $0.6\ \text{cm} \times 0.6\ \text{cm}$ RAND model. Gap junctions were distributed evenly around each cell.

To look at the effect of inhomogeneity on longitudinal propagation, all of the longitudinal and transverse gap junction conductivities, $g_j(PC)$, in the left half of the tissue were decreased to $0.01\ \mu\text{S}$, and the ρ_{oeff} of the tissue was increased to a value between 0.5 and $2.5\ \text{k}\Omega\text{-cm}$. Gap junction conductivities in the right-hand side of the tissue were set to normal values: $g_j(WC)=0.10\ \mu\text{S}$, and $\rho_{\text{oeff}} = 0.5\ \text{k}\Omega\text{-cm}$. In the case of transverse propagation, all of the longitudinal and transverse gap junction conductivities, $g_j(PC)$, in the bottom half of the tissue were increased to $0.01\ \mu\text{S}$, and the ρ_{oeff} of that region of tissue was also increased to a value between 0.5 and $2.5\ \text{k}\Omega\text{-cm}$. Gap junction conductivities in the top half of the tissue were set to higher values of $g_j(WC)=0.10\ \mu\text{S}$.

A schematic of the pattern of inhomogeneity used in the basic structure meshes is shown in Figures 6.3b and 6.3c. The dots indicate the cells at the transition boundary.

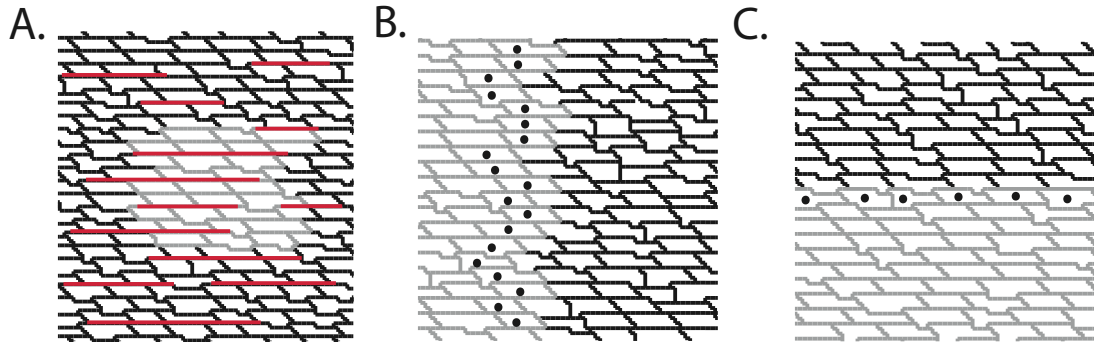


Figure 6.3: Representations of the inhomogeneous tissues with the poorly coupled region shown in gray and fibrotic strands shown in red. (A) Centralized inhomogeneous region used in the RAND model. (B) Basic inhomogeneous RAND mesh used to study longitudinal propagation (C) Basic inhomogeneous RAND mesh used to study transverse propagation.

6.2.5 Stimulation and Measurement Protocols

Except where specified, the focal source in 2-D is modeled using a point stimulus rather than a funny current focal source in order to have better control of the timing of the initiating current source. Point stimuli were generated by applying three intracellular current pulses to 110 node-square area in the center of the sheet of tissue at a basic cycle length of 200 ms. All stimuli were 2 ms in duration and approximately 1.5-2 times threshold intensity. Both the point current sources and the funny current sources are presented as generalized cases of focal activity in the heart. As proposed in a study by Pumir et al., we anticipate that the underlying influence of structure on the initiation and propagation of ectopic beats are broadly applicable to both triggered and spontaneous sources(86).

Longitudinal and transverse plane waves were generated in the basic structure meshes by stimulating the cells intracellularly along the left border or the top border of

the sheet, respectively, with a set of intracellular current pulses. All stimuli were 2 ms in duration and approximately 1.5-2 times threshold intensity.

$I_{Na,max}$ and action potential duration (APD) were measured at the center of the cell along a row or column of the sheet of tissue. Activation times were recorded at the time the membrane voltage initially reached -40 mV, and recovery times were recorded at the time the membrane voltage returned to -60 mV. The intracellular delays were computed by taking the difference of the activation times between two nodes along a single row or column located at the beginning and the end of a single cell. Gap junction delays were computed by taking the difference of activation times between two nodes along a single row or column located at the beginning of one cell and the end of the cell immediately preceding it. Action potential duration was computed as the difference between the recovery time and the activation time. In the well-coupled and poorly coupled regions, measurements were taken from points within the center of each region of the tissue to minimize boundary effects and the effect of stimulus artifact. At the transition zone between the well-coupled and poorly coupled region, measurements were taken from a line of observation points parallel to the direction of propagation. The dots in Figures 6.3B and 6.3C indicate the relative position of the observation points along the transition boundary. Means and standard deviations are reported for gap junction delays, maximum sodium current, and action potential duration. The data for the activation maps were recorded at a minimum of every 100 μ s.

6.3 Results

6.3.1 Initiation of Focal Beats in 1-D

A number of earlier studies have shown that decreases in intercellular coupling conductance reduce the current load from adjacent cells thus enabling action potentials to be generated using a smaller-sized focal source. As shown in Figure 6.4a, increasing the interstitial resistivity also reduces the focal size needed to initiate a focal beat in 1-D fibers. Interestingly, the reduction in focal size as the interstitial resistivity increases in the poorly coupled region is correlated with a reduction in the gap junction conduction delay at the boundary between the poorly coupled and well-coupled regions of the fibers (Figure 6.4b). In the fiber with moderate levels of coupling ($R_g=10 \Omega\text{-cm}^2$), increasing ρ_{oeff} from 0.25 to 5 k $\Omega\text{-cm}$ reduced the focal size by 53% (from 0.64 cm to 0.30 cm), and reduced the conduction delay at the boundary by 35% (from 0.78 ms to 0.51 ms). When ρ_{oeff} was increased from 0.25 to 5 k $\Omega\text{-cm}$ in the fiber with poor coupling ($R_g=100 \Omega\text{-cm}^2$), the reduction of focal size was less pronounced with only a 17% decrease in size (from 0.24 cm to 0.20 cm); however, increasing ρ_{oeff} from 0.5 to 5 k $\Omega\text{-cm}$ enabled the escape of the wavefront from the poorly coupled region to the surrounding well-coupled tissue. This finding was also observed in Chapter 4 where we investigated the effect of heterogeneous structure on the escape of action potentials generated using a point stimulus. The decrease in the conduction delay at the boundary between the two regions increases the likelihood that action potentials generated from small focal sources will escape from a poorly coupled region into surrounding well-coupled regions.

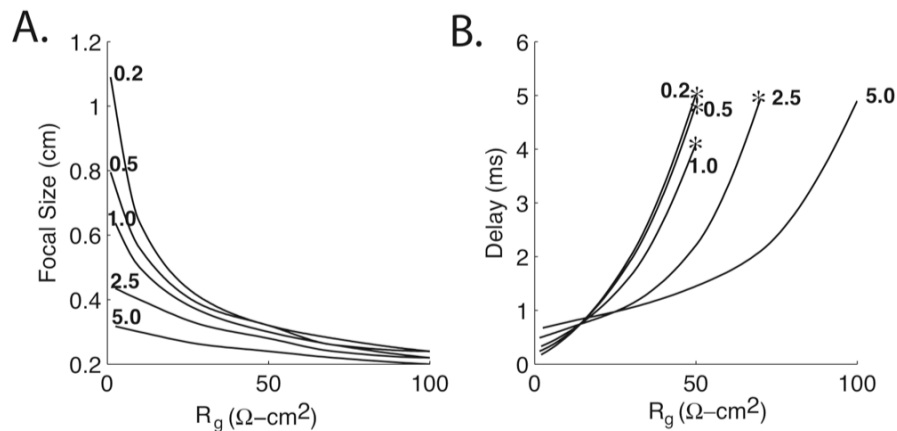


Figure 6.4: (A) Plot of the focal size as a function of gap junction resistivity (R_g) and effective interstitial resistivity (B) Delay at the boundary between the well-coupled and poorly coupled regions as a function of R_g and ρ_{eff} . Conduction block is indicated with a star. ρ_{eff} values are shown in bold.

In inhomogeneous 2-D tissue, the pattern of escape from a poorly coupled central region can be broken into three major groups illustrated in Figure 6.5: full escape, partial escape (unidirectional conduction block), complete block. Of particular interest are the structural properties that facilitate long conduction delays and partial escape (unidirectional block) because these conditions are known to increase the dispersion of repolarization and promote macroreentry.

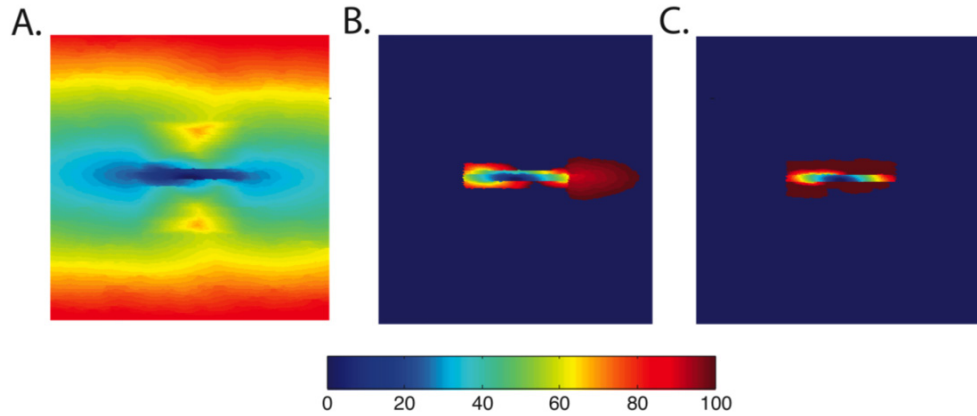


Figure 6.5: Activation maps during the first 100 ms of propagation in inhomogeneous tissue with varying levels of escape. (A) Full escape from the poorly coupled region when g_j of the inner region is equal to 0.01 mS/cm^2 . (B) Partial escape from the poorly coupled region when g_j of the inner region is equal to 0.003 mS/cm^2 . (C) Exit block when g_j of the poorly coupled region inner region is equal to 0.002 mS/cm^2 . The gap junction conductivity, g_j , of the outer region is equal to 0.10 mS/cm^2 , and ρ_{eff} is uniformly equal to $0.10 \text{ k}\Omega\text{-cm}$ in all cases.

6.3.2 Effect of Cell Arrangement in 2-D Tissue

In the first set of tissues (UN, BW), we looked at the effect of cell arrangement on the conduction delay in inhomogeneous tissue. In tissue with normal effective interstitial resistivity, changing from a uniform cell arrangement to a brickwall cell arrangement decreased the longitudinal conduction delay at the boundary between the well-coupled and poorly coupled region by 88% and had no effect on transverse propagation. In the uniform cell arrangement, the maximum sodium current density, $I_{\text{Na,max}}$ during longitudinal propagation in cells located just before the transition decreased from 358 ± 8 to $281 \pm 0 \text{ }\mu\text{A/cm}^2$ while $I_{\text{Na,max}}$ measured in the brick wall arrangement increased from 374 ± 18 to $409 \pm 1 \text{ }\mu\text{A/cm}^2$. The dispersion in action potential duration at the boundary between the two regions was more pronounced in the uniformly arranged tissues (5 ms) than in the tissues with brick wall arrangement (2

ms). During transverse propagation, the action potential dispersion at the boundary was 4 ms.

As shown in Tables 6.1 and 6.2, increasing ρ_{oeff} in the UN tissue caused a 25% increase in $I_{\text{Na,max}}$ during longitudinal propagation and a 46% decrease in the boundary conduction delay. In the tissue with a brick wall cell arrangement, increasing ρ_{oeff} caused a 2% increase in $I_{\text{Na,max}}$ and a 23% decrease in the boundary conduction delay. The dispersion in action potential duration decreased from 5 ms to 3 ms in the UN tissue and from 2 ms to 1 ms in the BW tissue. In both the UN and BW tissues, the $I_{\text{Na,max}}$ during transverse propagation decreased slightly from $360 \mu\text{A}/\text{cm}^2$ to $358 \mu\text{A}/\text{cm}^2$ while the conduction delay increased from 4.36 ms to 4.52 ms, an increase of 4%. The mean $I_{\text{Na,max}}$ measured during transverse propagation in the poorly coupled region (non-transition zone) remained unchanged at $374 \mu\text{A}/\text{cm}^2$, but the standard variation increased from ± 2 to $\pm 8 \mu\text{A}/\text{cm}^2$. In poorly coupled cells located away the boundary, the variation in $I_{\text{Na,max}}$ is primarily due to the fluctuations that occur within each individual cell.

6.3.3 Combined Effect of Cell Size and Increased ρ_{oeff} in 2-D Tissue

Cell Length and Width

Cell size varies widely in both diseased hearts as well as healthy hearts and is just as or more important than gap junction coupling for determining conduction properties in cardiac tissue(104).

In order to determine the combined effect of cell length and ρ_{oeff} on conduction delays in inhomogeneous tissue, we ran a set of simulations comparing brick wall tissues composed of long cells ($L=150\mu\text{m}$) under conditions of normal and increased ρ_{oeff} . Increasing ρ_{oeff} from 0.5 to 2.5 $\text{k}\Omega\text{-cm}$ in BW_{Long} tissues caused the $I_{\text{Na,max}}$ measured at the boundary during longitudinal propagation to increase from $405\pm 5 \mu\text{A}/\text{cm}^2$ to 422 ± 25

$\mu\text{A}/\text{cm}^2$, a 4% increase, and the longitudinal conduction delay at the boundary to decrease from 1.14 ms to 0.95 ms, a 17% decrease.

In tissue with normal ρ_{eff} increasing cell width from 30 μm to 40 μm increased $I_{\text{Na,max}}$ at the transition boundary during longitudinal propagation by 2% and decreased the longitudinal conduction delay at the boundary between the well-coupled and poorly coupled region by 20%. The $I_{\text{Na,max}}$ at the transition during transverse propagation decreased from 360 $\mu\text{A}/\text{cm}^2$ to 346 $\mu\text{A}/\text{cm}^2$ (-4%) and the transverse conduction delay at the transition boundary increased from 4.36 ms in the BW tissue with normal-sized cells to 5.09 ms in the BW tissue with wider cells (an 18% increase).

As shown in Table 6.1, increasing ρ_{eff} in the BW models composed of wider cells caused a 2% increase in $I_{\text{Na,max}}$ at the transition boundary during longitudinal propagation and a 26% decrease in the boundary conduction delay. In the transverse direction, $I_{\text{Na,max}}$ and the conduction delay measured at the transition boundary remained essentially unchanged when ρ_{eff} was increased.

Table 6.1: Gap junction delay, $I_{Na,Max}$ and Action Potential Duration(APD) measured during longitudinal propagation as a function of ρ_{oeff} in different regions of inhomogeneous tissues with varied underlying structures.

<i>Gap Junction Delay</i>				
Structure	ρ_{oeff}	PC Region	Boundary Region	WC Region
UN	0.5	1.95±0.00	10.37±0	0.27±0.00
	2.5	1.88±0.00	5.48±0	0.27±0.00
BW	0.5	0.96±0.00	1.29±0.03	0.19±0.00
	2.5	0.85±0.00	0.99±0.08	0.19±0.00
BW _{Long}	0.5	1.02±0.01	1.14±0.02	0.19±0.00
	2.5	0.88±0.02	0.95±0.03	0.19±0.00
BW _{Wide}	0.5	1.09±0.00	1.55±0.01	0.21±0.00
	2.5	0.98±0.01	1.14±0.08	0.21±0.00
RAND	0.5	0.82±0.23	1.36±0.41	0.15±0.03
	2.5	0.69±0.19	0.84±0.21	0.14±0.03

<i>$I_{Na,max}$</i>				
Structure	ρ_{oeff}	PC Region	Boundary Region	WC Region
UN	0.5	-358±8	-281±0	-385±26
	2.5	-358±32	-352±0	-385±26
BW	0.5	-374±18	-409±1	-392±3
	2.5	-376±29	-417±9	-392±3
BW _{Long}	0.5	-375±30	-405±6	-393±6
	2.5	-379±20	-422±25	-392±6
BW _{Wide}	0.5	-372±16	-401±2	-390±6
	2.5	-374±32	-410±7	-390±6
RAND	0.5	-371±21	-387±18	-392±12
	2.5	-377±34	-402±17	-392±12

<i>APD</i>				
Structure	ρ_{oeff}	PC Region	Boundary Region	WC Region
UN	0.5	173±0	178±0	173±0
	2.5	173±0	176±0	173±0
BW	0.5	173±0	174±0	173±0
	2.5	173±0	175±0	173±0
BW _{Long}	0.5	173±0	174±0	173±0
	2.5	173±0	175±0	173±0
BW _{Wide}	0.5	173±0	174±0	173±0
	2.5	173±0	175±0	173±0
RAND	0.5	173±0	174±0	173±0
	2.5	173±0	174±0	173±0

Table 6.2: Gap junction delay, $I_{Na,Max}$ and Action Potential Duration(APD) measured during transverse propagation as a function of ρ_{eff} in different regions of inhomogeneous tissues with varied underlying structures.

<i>Gap Junction Delay</i>				
Structure	ρ_{eff}	PC Region	Boundary Region	WC Region
UN	0.5	0.73±0.00	4.36±0.00	0.18±0.00
	2.5	0.73±0.00	4.52±0.00	0.18±0.00
BW	0.5	0.73±0.00	4.36±0.00	0.18±0.01
	2.5	0.73±0.00	4.51±0.00	0.18±0.00
BW _{Long}	0.5	0.73±0.00	4.36±0.00	0.18±0.01
	2.5	0.73±0.00	4.52±0.00	0.18±0.00
BW _{Wide}	0.5	0.90±0.00	5.09±0.00	0.20±0.01
	2.5	0.90±0.00	5.06±0.00	0.20±0.00
RAND	0.5	0.70±0.05	4.03±0.20	0.17±0.02
	2.5	0.68±0.07	3.73±0.32	0.17±0.01

<i>$I_{Na,max}$</i>				
Structure	ρ_{eff}	PC Region	Boundary Region	WC Region
UN	0.5	-374±2	-360±0	-386±2
	2.5	-374±8	-358±0	-386±2
BW	0.5	-374±2	-360±0	-386±2
	2.5	-374±8	-358±0	-386±2
BW _{Long}	0.5	-374±2	-360±0	-386±2
	2.5	-374±8	-358±0	-386±2
BW _{Wide}	0.5	-371±2	-346±0	-385±5
	2.5	-371±12	-346±0	-384±5
RAND	0.5	-374±8	-360±11	-388±6
	2.5	-374±20	-367±18	-388±6

<i>APD</i>				
Structure	ρ_{eff}	PC Region	Boundary Region	WC Region
UN	0.5	173±0	177±0	173±0
	2.5	173±0	177±0	173±0
BW	0.5	173±0	177±0	173±0
	2.5	173±0	177±0	173±0
BW _{Long}	0.5	173±0	177±0	173±0
	2.5	173±0	177±0	173±0
BW _{Wide}	0.5	173±0	177±0	173±0
	2.5	173±0	177±0	173±0
RAND	0.5	173±0	177±0	174±0
	2.5	173±0	177±0	174±0

6.3.4 Effect of Increased ρ_{off} in Randomly Generated Tissue

Increasing ρ_{off} from 0.5 to 2.5 k Ω -cm in the RAND tissue model caused $I_{\text{Na,max}}$ measured during longitudinal propagation to increase from 387 ± 18 to 402 ± 17 $\mu\text{A}/\text{cm}^2$, an increase of 4%, and the longitudinal conduction delay to decrease from 1.36 ± 0.41 to 0.84 ± 0.21 ms, a decrease of 38%. This percentage change in the boundary conduction delay was greater than that observed in any of the BW models but much less than that observed in the uniform model. During transverse propagation, increasing ρ_{off} from 0.5 to 2.5 k Ω -cm in the RAND tissue model caused $I_{\text{Na,max}}$ measured at the transition boundary to increase from 360 ± 11 to 367 ± 18 $\mu\text{A}/\text{cm}^2$, an increase of 2%, and the transverse conduction delay to decrease from 4.03 ± 0.20 to 3.73 ± 0.32 ms, a decrease of 7%. This percentage change in the boundary conduction delay during transverse propagation was much smaller than that observed during longitudinal propagation. The variation in $I_{\text{Na,max}}$ and conduction delay at the transition boundary during both longitudinal and transverse propagation can be clearly seen in Figure 6.6. No conduction block was observed for the case of $g_j(\text{PC})=0.01$ μS . The shortest conduction delays were correlated with regional cell arrangements that placed boundary cells between two adjacent cells that were poorly coupled but not located directly on the boundary.

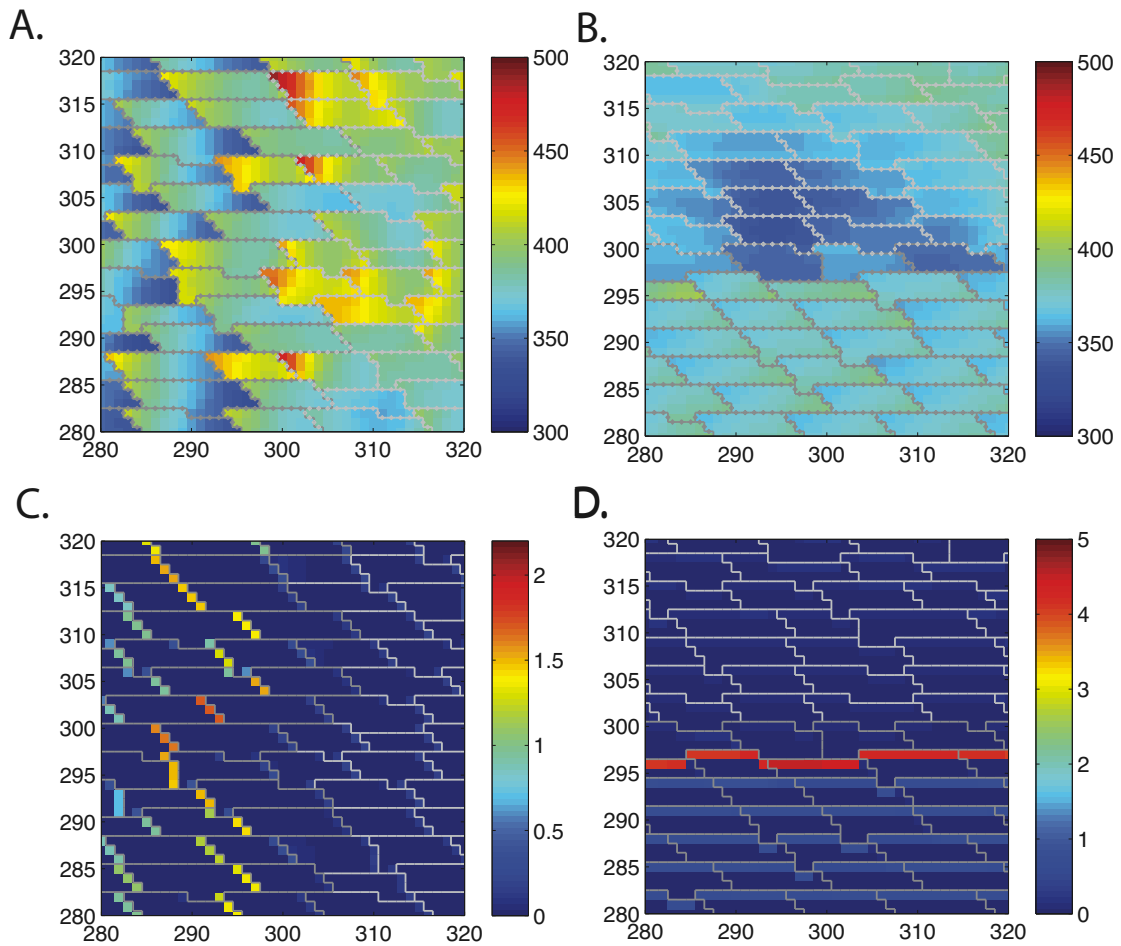


Figure 6.6: Distribution of $I_{Na,max}$ (A,B) and gap junction delays(C,D) in inhomogeneous RAND tissues during longitudinal(A,C) and transverse propagation(B,D) with no conduction block. *Dark Gray:* Poorly coupled Tissue. *Light Gray:* Well-coupled Tissue.

6.3.5 Implications for ectopic beats and reentrant circuits

In the presence of source-sink mismatch caused by an abrupt change in coupling, small variations in cell arrangement can also increase the likelihood of unidirectional conduction block and microentry. In three comparable cases, where R_g of the inner network = $0.003 \mu S$, R_g of the outer network = $0.01 \mu S$, and ρ_{off} of the entire tissue was set equal to $0.5 \text{ k}\Omega\text{-cm}$, the ectopic beat was able to escape out of the central zone through a small subset of cells at the boundary between the well-coupled and poorly-coupled

regions. Slow conduction caused by heterogeneity in the outer region enabled the escaped beat to propagate around and reenter the poorly coupled region from the other side.

Activation maps for each of the three cases are shown in Figure 6.7A,B, and C. When corresponding traditional monodomain (models which incorporated the same intracellular structure but included no interstitial properties) were simulated, all three cases showed complete conduction block. Increasing the ρ_{off} of the poorly coupled region from 0.5 k Ω -cm to 2.5 k Ω -cm, increased the number of points of escape as shown in Figure 6.7D,E, and F, which in all cases inhibited sustained reentry.

Figures 6.8, 6.9, and 6.10, show magnified images of the escape from the poorly coupled region with isolines of the activation times. These figures correspond to the cases shown in Figures 6.7A,B, and C. In each case, a small variation in which a boundary cell is adjacent to two or more non-boundary cells that have already activated is the driving force for the escape. The wavefront at the escape point had a large curvature similar to the wavefront generated by the point stimulus that was originally used to stimulate the tissue. The arrows indicate the site of escape.

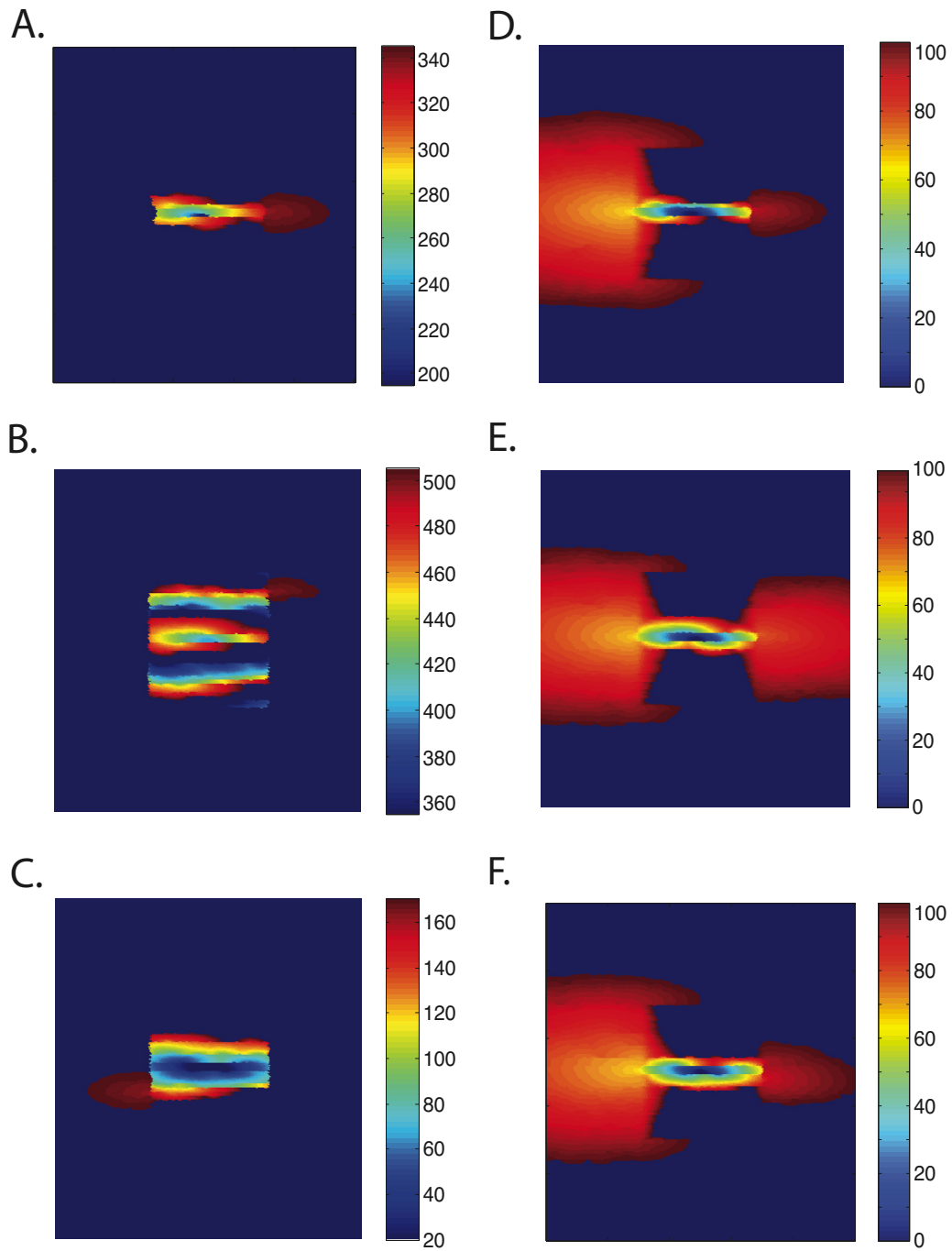


Figure 6.7: (A,B,C) Partial escapes shown for comparable tissues with $g_j(\text{inner})=0.003 \mu\text{S}$, $g_j(\text{outer})=0.10 \mu\text{S}$, and $\rho_{\text{oeff}}=0.5 \text{ k}\Omega\text{-cm}$ (D,E,F) Multiple escapes for tissues with ρ_{oeff} increased to $2.5 \text{ k}\Omega\text{-cm}$.

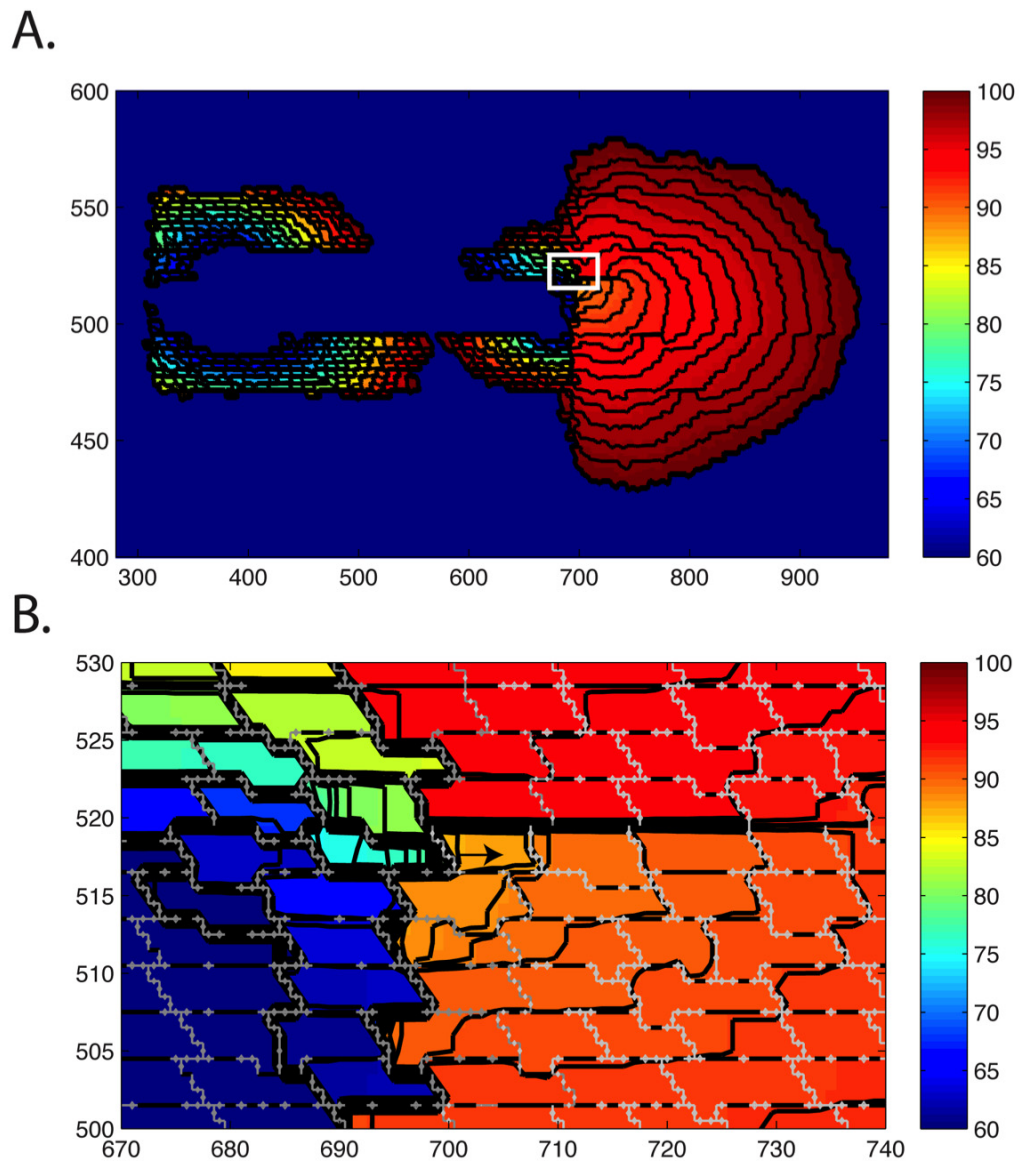
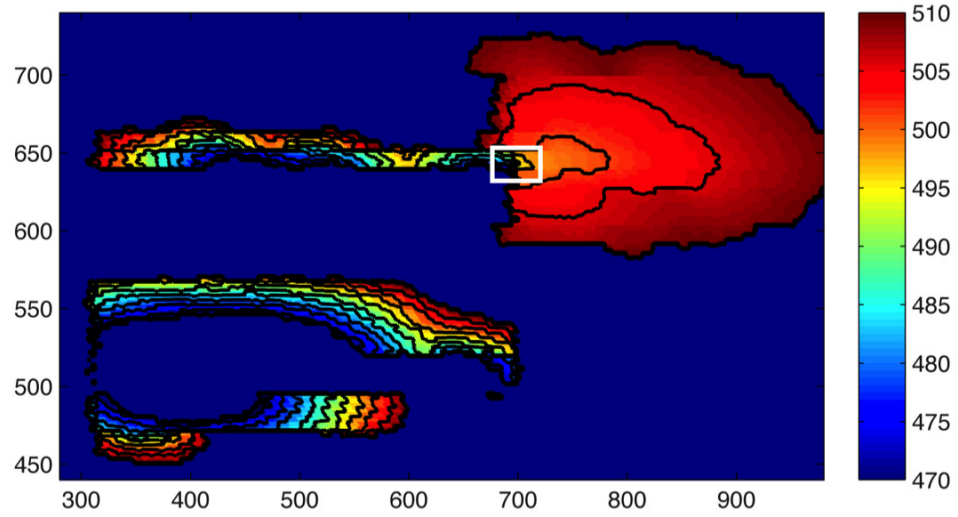


Figure 6.8: Magnified image with isolines for the escape shown in Figure 6.7A.

A.



B.

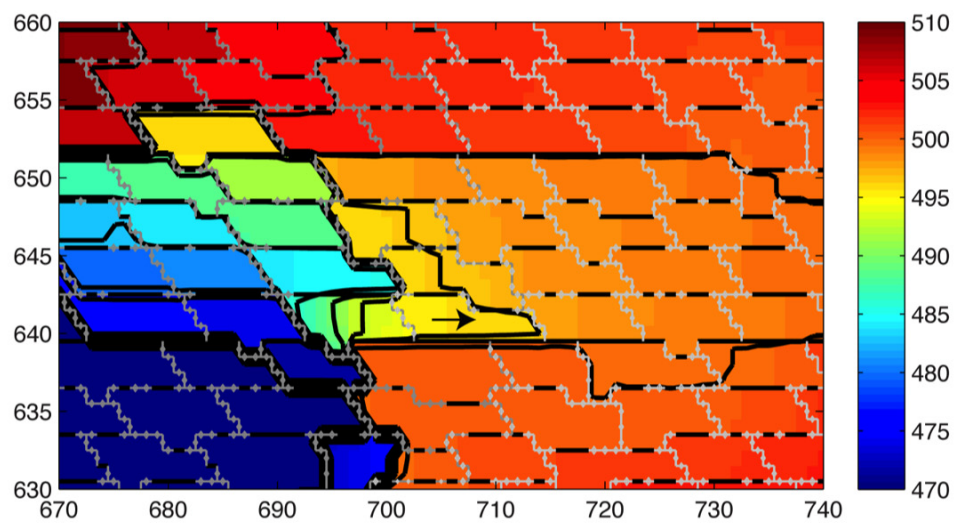
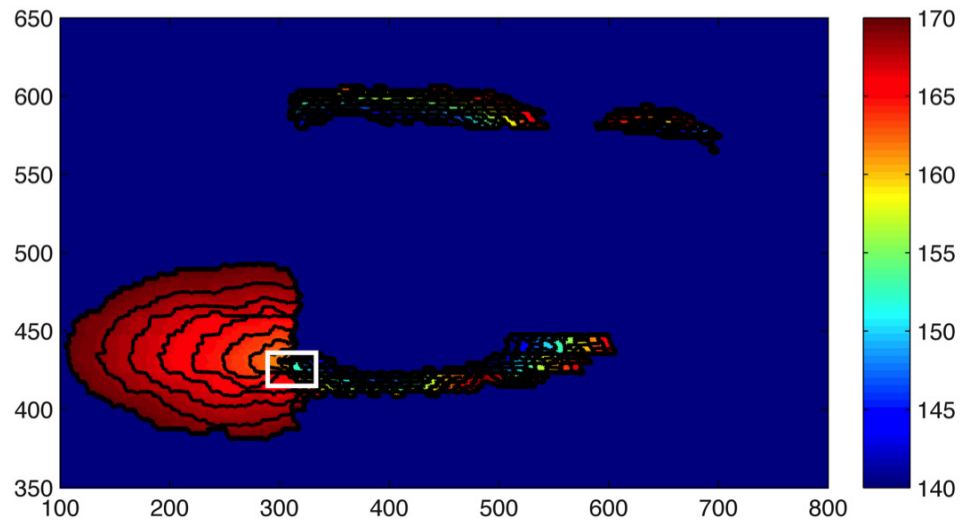


Figure 6.9: Magnified image with isolines for the escape shown in Figure 6.7B.

A.



B.

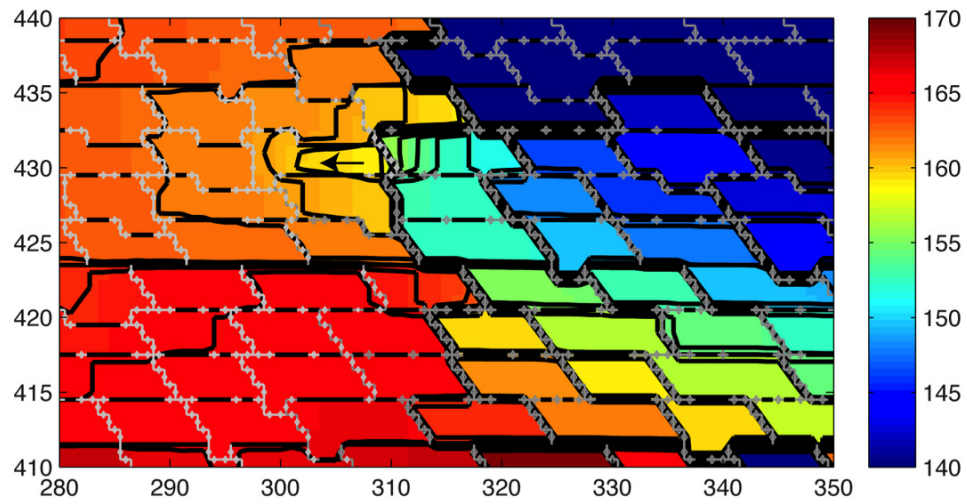


Figure 6.10: Magnified images with isolines for the escape shown in 6.7C.

In two out of three of the cases, where R_g of the inner network=0.002 μS , R_g of the outer network=0.01 μS , and ρ_{off} of the entire tissue was set to 0.5 $\text{k}\Omega\text{-cm}$, all three of the ectopic beats which were given at $t=0$ ms, $t=200$ ms, and $t=400$ ms as well as the resulting microreentry were completely contained in the poorly-coupled region. Snapshots of the contained reentry are shown in Figure 6.11A-H. Increasing ρ_{off} to 5 $\text{k}\Omega\text{-cm}$ released the escape and facilitated macroreentry as displayed in Figure 6.12A-H. The first ectopic beat was given at $t=0$ ms and escaped from the poorly coupled region at $t=110$ ms (Figure 6.12A). The escaped beat propagated out of the tissue and around the top and bottom of the poorly coupled region. The second ectopic beat was given at $t=200$ ms and escaped from the poorly coupled region at $t=380$ ms (Figure 6.12D). A third ectopic beat was given at $t=400$ ms but the tissue had not yet recovered so the beat did not propagate. The second ectopic beat that escaped at $t=380$ ms reentered the right side of the tissue at $t=500$ ms (Figure 6.12F), passed through the center of the poorly coupled tissue, and escaped out of the left side of the tissue at $t=640$ ms (Figure 6.12G). This pattern of reentry continued for the entire 1000 ms of the simulation.

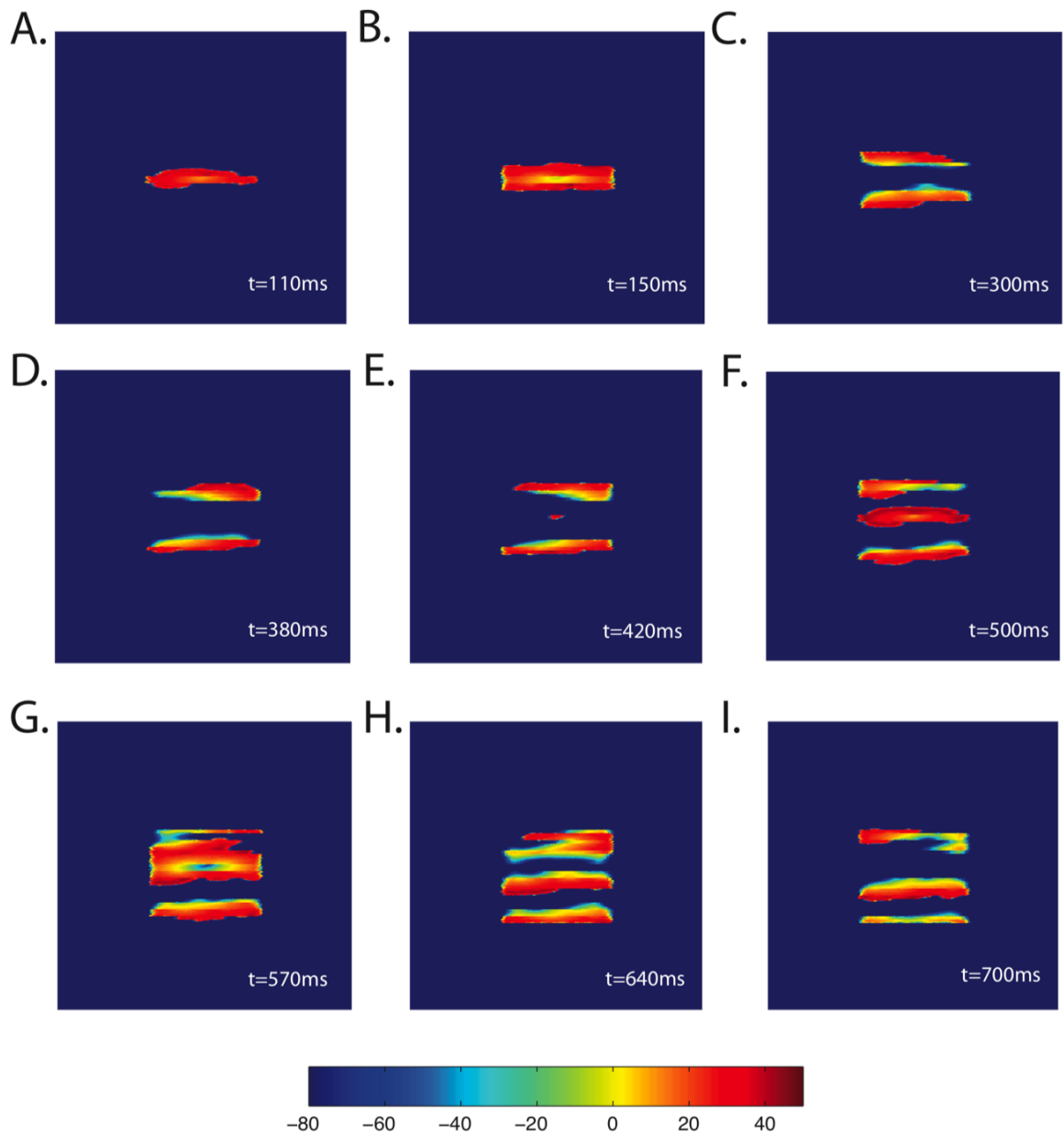


Figure 6.11: Contained reentry shown for the case with g_j (outer) = 0.1 mS/cm², g_j (inner) network=0.002 mS/cm², and $\rho_{\text{eff}}=0.50$ k Ω -cm throughout the tissue.

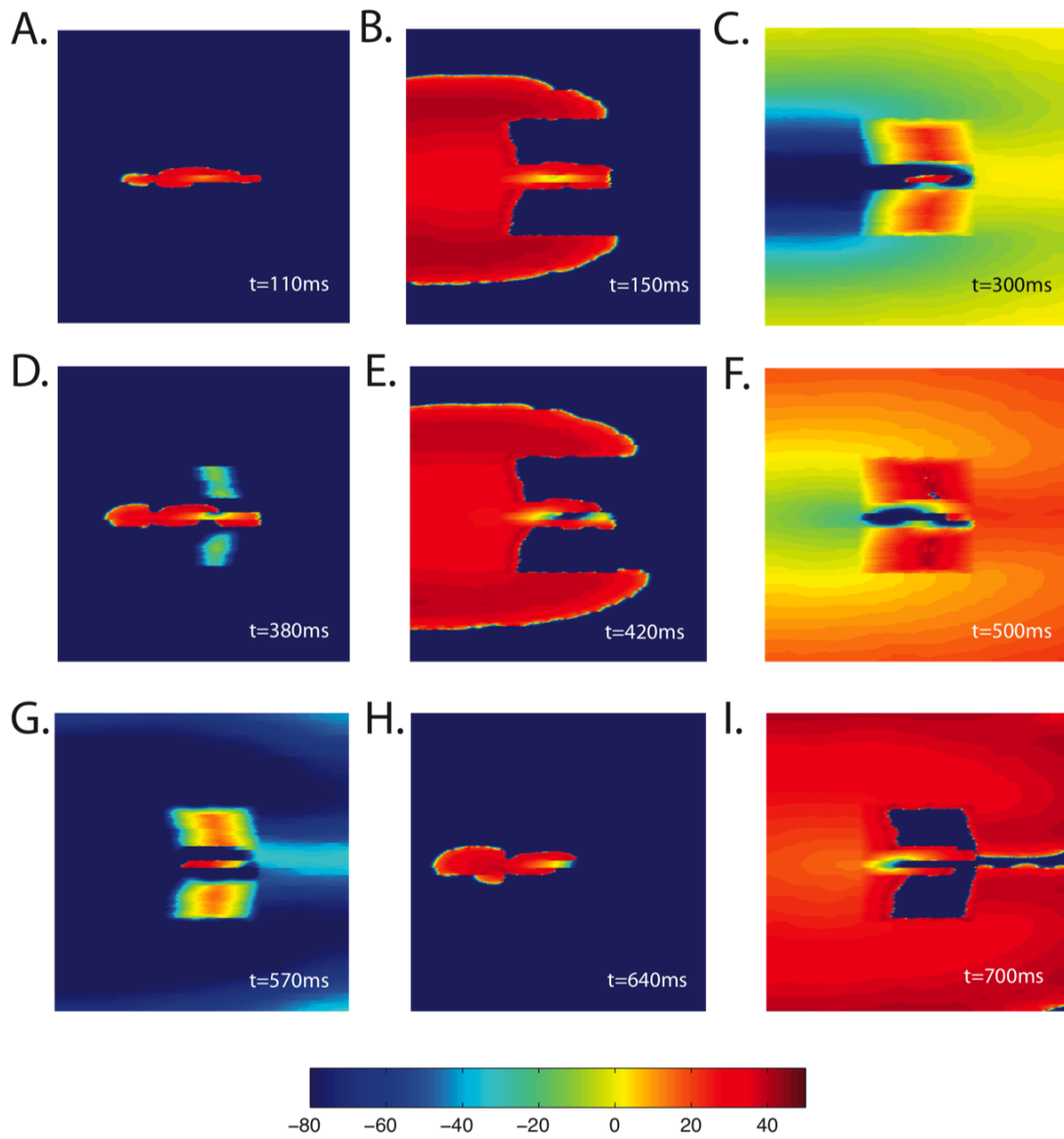


Figure 6.12: Progression of the escape of ectopic beat and the resulting reentry for a period of 700 ms. Shown for the case with g_j (outer) = 0.100 mS, g_j (inner) network=0.002 mS, and ρ_{oeff} increased to 5.0 k Ω -cm in the central region of the tissue.

For simplicity, this study only considers the effect of one focal source that is generated using either a point current source or a funny current. In the case of the point current source, both partial escapes and sustained microreentry were observed because the area of the point source (0.01 cm x 0.01 cm) was much smaller than the area of the heterogeneous region. In order to generate focal activity using a funny current, a larger, slowly-activating focal region of tissue that comprised almost 50% of the heterogeneous region was used, and, consequently, partial escape but no sustained microreentry was observed (Figure 6.12). The curvature of the wavefront at the point of escape was much more pronounced than the curvature at the original site of the ectopic beat. Sustained microreentry may be more likely to occur in larger tissue preparations, which have a smaller ratio of the area of the focal region to the area of the poorly coupled region.

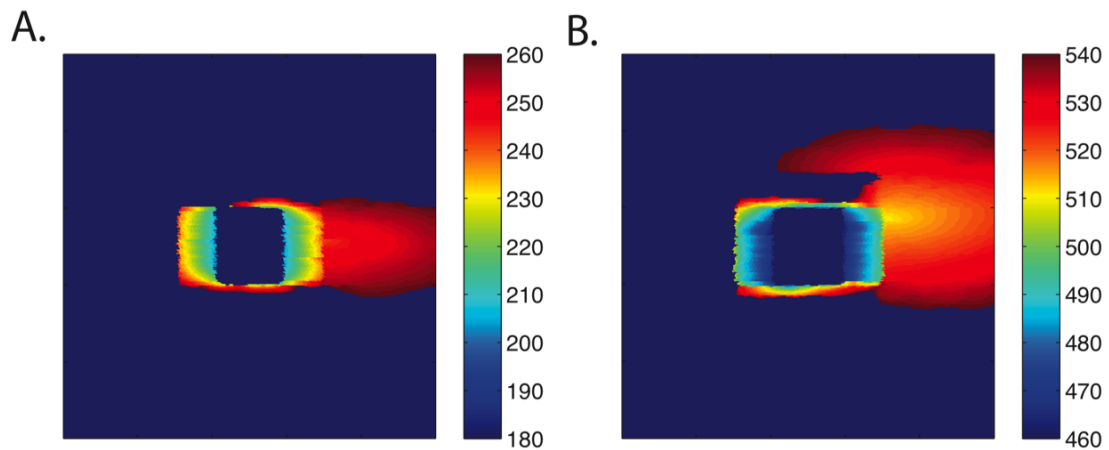


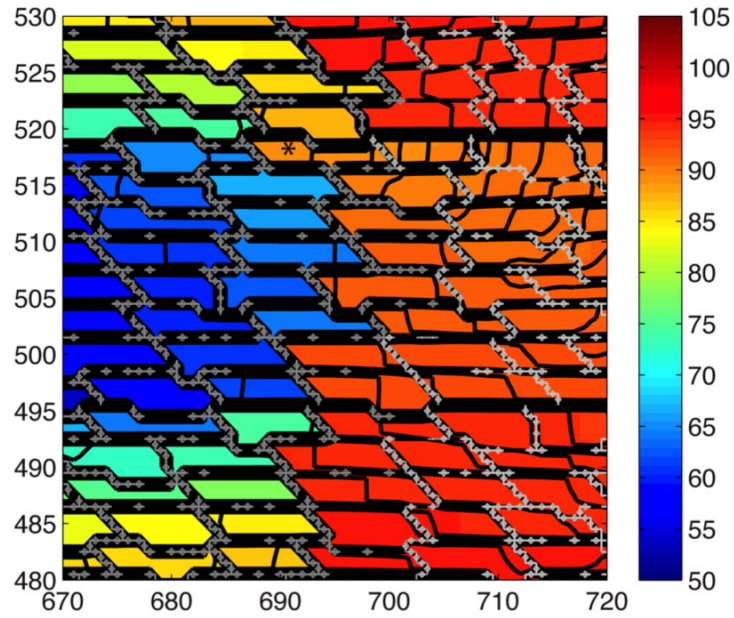
Figure 6.13: Partial escape from a poorly coupled region shown for two comparable cases where activation is driven by funny current focal sources. In both cases, g_j of the poorly coupled inner region is 0.003 mS, and ρ_{oeff} is uniformly equal to 0.5 k Ω -cm

6.4 Discussion

The co-localization of regions of increased interstitial resistivity with regions of reduced gap junction coupling may be a key component of ectopic substrates that support both the generation and propagation of focal beats. Large decreases in interstitial resistivity help to confine focal beats to a poorly coupled region of tissue, while large increases in interstitial resistivity enable the full escape or full block of action potentials generated by a rapidly firing source. The greatest danger may come from moderate changes in interstitial resistivity that facilitate the partial escape of small wavefronts that have large curvature.

The mechanism for improved conduction as interstitial resistivity increases is the reduction in source-load mismatch at the boundary between the poorly coupled and well-coupled region. An elegant study by Rohr et al., which investigated the onset of conduction block caused by structural discontinuities showed that partial uncoupling of the current load or both the current source and current load can improve conduction, while partial uncoupling of the source current does not delay the onset of conduction block(90). The results from this study indicate that local increases in interstitial resistivity that occur in the region of the source current and close to the source-sink boundary, which in the case of spontaneously active tissue is more likely to be diseased than the surrounding well-coupled tissue, can also reduce source-load mismatch. As little as a 2% increase in the maximum sodium current during longitudinal propagation decreased the conduction delay at the site of source-load mismatch by almost 40%. In the ectopic substrate shown in Figure 6.14, sensitivity to variations in sodium current translates into a microscopic route of escape that facilitates macroreentry.

A.



B.

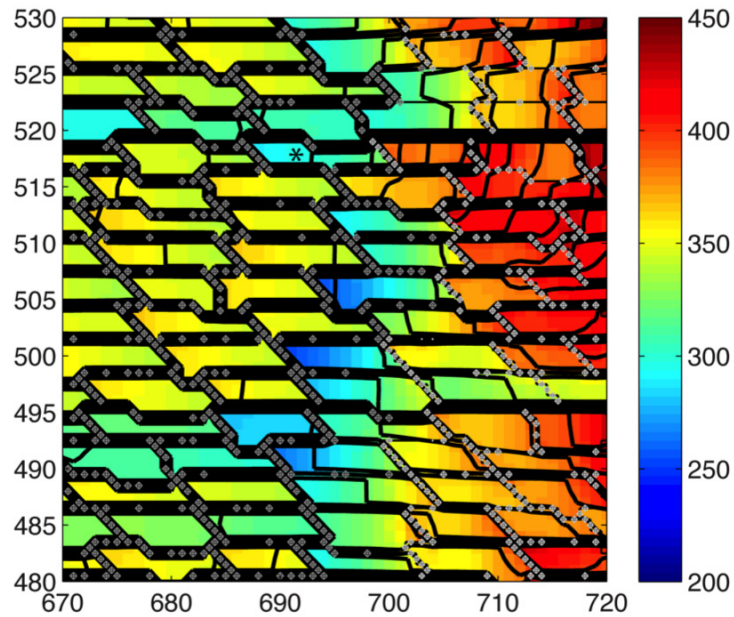


Figure 6.14: (A) Voltage activation map (time in ms) shown with contour lines during the escape. (A) Distribution of $I_{Na,max}$ ($\mu A/cm^2$) shown with contour lines after all the cells have activated. The active cell at the point of escape is indicated with a star.

This increased sensitivity to $I_{Na,max}$ in critical regimes characterized by low excitability and low coupling is consistent with experimental and modeling studies by Spach et al. which showed that small changes in the location and timing of premature beats generated in aging human atrial bundles can lead to conduction abnormalities such as reentry and lateral shifts in a small area of tissue. It is important to note that the distribution of maximum sodium current in cardiac tissue is influenced by a number of factors including the direction of the propagating wavefront, the cell arrangement, gap junction distribution, and cell size. During longitudinal propagation, the maximum sodium current tends to be highest at the entry point into the cell and lowest at exit point from the cell. Propagation in the transverse direction is less sensitive to increases in effective interstitial resistivity than propagation in the longitudinal direction because the short width of the cell helps to contain the ionic current and compensates for the large variations in $I_{Na,max}$ that occur along the inside of the cell.

Cell arrangement has a large influence on the maximum sodium current, and consequently, on the escape of ectopic beats in inhomogeneous tissue (2-D). The combination of microstructural heterogeneity in both cell arrangement and interstitial resistivity increase the likelihood of partial escape from poorly coupled regions to well-coupled regions of tissue and significantly increases vulnerability to macroreentry. Regions that have the largest source-load mismatch show the greatest percentage increase in $I_{Na,max}$ and the greatest percentage decrease in conduction delay as ρ_{eff} increases; however, these sites are much less likely to facilitate escape than other regions which have a lower source-load mismatch due to cell arrangement. A recent study by Kim et al. has shown that the improved conduction observed in model tissues that have a brick wall cell arrangement can be attributed to a local increase in the effective resistivity(55). Continuous models which incorporate variations in resistivity in regions

of tissue with source-sink mismatch may also be able to capture the complex dynamics at the boundary, but may not be able to effectively portray the directional effects of increased effective interstitial resistivity. A more detailed explanation of the differences between continuous and discrete models in the case of increased interstitial resistivity can be found in Chapter 4. Although Chapter 4 primarily focuses on 1-D propagation, many of the qualitative findings about the differences between continuous and discrete models and the effect of cell size are applicable in 2-D as well.

Limitations

While the distribution of the gap junctions is varied in the model, the actual conductance of the gap junction is constant throughout the tissue. In real tissue preparations, heterogeneity in gap junction expression as well as gradients of coupling will also affect the complexity of the pattern of escape. The tissue resistances, cell arrangements, and cell shapes used in the study are hypothetical parameters that may occur locally in diseased regions of tissue. However, we believe that the general findings of this study provide a qualitative insight into how interstitial and intracellular microstructural architecture influence the escape of ectopic beats in regions of tissue that have significant source-sink mismatch.

7. Conclusions

This dissertation study demonstrates that small variations in myocardial architecture play a larger role in conduction in the presence of source-load mismatch caused by abrupt changes in coupling. Increases in effective interstitial resistivity within the poorly coupled region can help to reduce the effects of source-load mismatch and can both facilitate and impede microentry in heterogeneous tissue.

The complex microstructure of myocardium facilitates additional pathways of current flow and creates small variations in the distribution of maximum sodium current that influence both longitudinal and transverse propagation. These alternative pathways of current help to maintain conduction in critical regimes such as the ectopic substrate.

7.1 Major Findings

In answer to our first question, “How does heterogeneity in intracellular and interstitial microstructure influence propagation in critical regimes characterized by reduced cell-to-cell coupling and reduced excitability?”, we have come to the following conclusions:

- Increasing ρ_{off} in poorly coupled 1-D fibers alters the distribution of electrical load at the microscale and causes propagation to become more like that observed in continuous fibers. In the poorly coupled fiber, this nearly continuous state is characterized by decreased gap junction delay, sustained conduction velocity, increased sodium current, reduced maximum upstroke velocity, and increased safety factor.

- Long, poorly coupled cells experience greater loading effects than short cells and show the greatest initial response to changes in ρ_{oeff} because they have a much larger distribution of $I_{\text{Na,max}}$ which influences source-sink mismatch at the cell borders.

-In inhomogeneous fibers with adjacent well-coupled and poorly coupled regions, increasing ρ_{oeff} in the poorly coupled region also reduces source-load mismatch, which delays the onset of conduction block and reduces the dispersion of repolarization at the transition between the two regions. This reduction in the dispersion of repolarization at the boundary decreases the dependence of the boundary conduction delay on the coupling beat interval between consecutive stimuli.

-In homogeneous as well as heterogeneous 2-D tissue models, brick wall architecture and jutting decrease cell-to-cell delay, increase the maximum sodium current, and decrease longitudinal maximum upstroke velocity. Lateral decoupling makes poorly coupled fibers more susceptible to conduction block and to increased dispersion of repolarization.

-Small increases in the maximum sodium current during longitudinal propagation decrease the conduction delay at the site of source-load mismatch by disproportionately large amounts indicating that sites of source-load mismatch are extremely sensitive to small changes in sodium current.

-Conduction delays caused by source-sink mismatches in the direction of transverse propagation are less sensitive to changes in effective interstitial resistivity because the small width of the cells helps to compensate for the cell-to-cell boundary effects.

In answer to our second question, “Can interstitial and intracellular microheterogeneity contribute to complex patterns of escape for ectopic beats that originate in a poorly coupled region of tissue?” we have come to the following conclusions:

-Local increases in the effective interstitial resistivity not only reduce the size of the focal source needed to generate an ectopic beat in poorly coupled tissue but also increase the source current during longitudinal propagation and increase the likelihood of escape and reentry in poorly coupled regions of tissue with heterogeneous cell arrangement.

-Variations in the distribution of sodium current as a function of cell length and width lead to directional differences in the response to increases in effective interstitial resistivity.

In answer to the last question, “Can continuous domains which average the microheterogeneities in the interstitial and intracellular spaces effectively capture the complex ectopic and reentrant behavior observed in poorly coupled tissue?” we conclude that current implementation of continuous models may be able to account for random heterogeneity in cell arrangement simply by implementing additional random heterogeneity in coupling, particularly in areas of high source-sink mismatch; however, models which include increases in interstitial resistivity should account more carefully for 1) directional differences in the effect of increased interstitial resistivity and 2) the microscopic changes in source-load mismatch which may manifest as a local increase in effective conductivity when the material composition of the interstitial space becomes

more resistive or the space becomes more confined. Continuous models may also not be suitable for studying variability in V_{\max} or $I_{\text{Na,max}}$ in regions with microheterogeneity in both the intracellular and interstitial space.

7.2 Limitations and Future Work

The studies in this dissertation were all completed using ventricular models of cardiac tissue. We expect that comparable studies in other cell types such as atrial or Purkinje cells will show qualitatively similar results; however, differences in cell size and shape and the content of the surrounding interstitial space may introduce additional behaviors that were not observed in this study. The role of the geometry of the wavefront was also not considered in this study, but is also likely to have a strong influence on action potential propagation in critical regimes(13, 26). Although the large majority of the findings in this study are consistent with *in vivo* and *in vitro* studies of cardiac propagation, many of the findings, particularly those related to the effects of ρ_{eff} on the microscale distribution of $I_{\text{Na,max}}$, will need to be validated using experimental techniques that have yet to be developed. The gap junction values used in these studies were selected so that we could observe conditions of slow conduction and conduction block rather than to match actual experimental measurements. An interesting direction for future study would be to create corresponding sets of *in vitro* experimental monolayers and 2-D microstructural models that investigate cardiac propagation in the critical regimes described in this dissertation research. The focus of this study was the changes in microstructure that occur in diseased tissue; however, these changes often occur in concert with changes in ionic process that also affect membrane excitability and repolarization dynamics. Regions of increased interstitial resistivity may also have

paradoxical influences on the relative contributions of sodium, calcium, and potassium currents in regions with high source-load mismatch. An interesting area for future study will be to investigate how the combination of microstructural heterogeneity in the interstitial space and the preferential localization of sodium channels in the intercalated disk influence conduction properties in healthy and diseased tissue.

Future studies will use large-scale models of the human atria to investigate the effect of co-localization of interstitial and intracellular heterogeneity on calcium currents and triggered focal sources during the development of atrial fibrillation. The increased complexity of cardiac cell arrangement as well as the presence of variable fiber orientation and interlaminar clefts in the three-dimensional heart may also increase the complexity of the escape of ectopic beats.

References

1. Allesie MA, Bonke FIM, and Schopman FJG. Circus movement in rabbit atrial muscle as a mechanism of tachycardia .2. Role of nonuniform recovery of excitability in occurrence of unidirectional block, as studied with multiple microelectrodes. *Circulation Research* 39: 168-177, 1976.
2. Allesie MA, Bonke FIM, and Schopman FJG. Circus movement in rabbit atrial muscle as a mechanism of tachycardia .3. Leading circle concept - New model of circus movement in cardiac tissue without involvement of an anatomical obstacle. *Circulation Research* 41: 9-18, 1977.
3. Arora R, Verheule S, Scott L, Navarrete A, Katari V, Wilson E, Vaz D, and Olgin JE. Arrhythmogenic substrate of the pulmonary veins assessed by high-resolution optical mapping. *Circulation* 107: 1816-1821, 2003.
4. Arutunyan A, Pumir A, Krinsky V, Swift L, and Sarvazyan N. Behavior of ectopic surface: effects of beta-adrenergic stimulation and uncoupling. *American Journal of Physiology-Heart and Circulatory Physiology* 285: H2531-H2542, 2003.
5. Bian WN and Tung L. Structure-related initiation of reentry by rapid pacing in monolayers of cardiac cells. *Circulation Research* 98: E29-E38, 2006.
6. Biktashev VN, Arutunyan A, and Sarvazyan NA. Generation and escape of local waves from the boundary of uncoupled cardiac tissue. *Biophysical Journal* 94: 3726-3738, 2008.
7. Boldt A, Scholl A, Garbade J, Resetar M, Mohr F, Gummert J, and Dhein S. ACE-inhibitor treatment attenuates atrial structural remodeling in patients with lone chronic atrial fibrillation. *Basic Research in Cardiology* 101: 261-267, 2006.
8. Bosman FT, Cleutjens J, Beek C, and Havenith M. Basement-Membrane Heterogeneity. *Histochemical Journal* 21: 629-633, 1989.
9. Bub G, Shrier A, and Glass L. Spiral wave generation in heterogeneous excitable media. *Physical Review Letters* 88, 2002.
10. Bursac N, Parker KK, Iravanian S, and Tung L. Cardiomyocyte cultures with controlled macroscopic anisotropy - A model for functional electrophysiological studies of cardiac muscle. *Circulation Research* 91: E45-E54, 2002.

11. Burstein B and Nattel S. Atrial Fibrosis: Mechanisms and Clinical Relevance in Atrial Fibrillation. *J Am Coll Cardiol* 51: 802-809, 2008.
12. Cabo C and Boyden PA. Extracellular Space Attenuates the Effect of Gap Junctional Remodeling on Wave Propagation: A Computational Study. 96: 3092-3101, 2009.
13. Cabo C, Pertsov AM, Baxter WT, Davidenko JM, Gray RA, and Jalife J. Wave-Front Curvature as a Cause of Slow Conduction and Block in Isolated Cardiac-Muscle. *Circulation Research* 75: 1014-1028, 1994.
14. Cabo C, Yao JN, Boyden PA, Chen S, Hussain W, Duffy HS, Ciaccio EJ, Peters NS, and Wit AL. Heterogeneous gap junction remodeling in reentrant circuits in the epicardial border zone of the healing canine infarct. *Cardiovascular Research* 72: 241-249, 2006.
15. Camelliti P, Borg TK, and Kohl P. Structural and functional characterisation of cardiac fibroblasts. *Cardiovascular Research* 65: 40-51, 2005.
16. Campbell SE, Rakusan K, and Gerdes AM. Change in cardiac myocyte size distribution in aortic-constricted neonatal rats. *Basic Research in Cardiology* 84: 247-258, 1989.
17. Carmeliet E. Cardiac Ionic Currents and Acute Ischemia: From Channels to Arrhythmias. *Physiol Rev* 79: 917-1017, 1999.
18. Crank J and Nicolson P. A practical method for numerical evaluation of solutions of partial differential equations of the heat-conduction type. *Advances in Computational Mathematics* 6: 207-226, 1996.
19. Debacker JMT, Vancapelle FJL, Janse MJ, Tasseron S, Vermeulen JT, Dejonge N, and Lahpor JR. Slow Conduction in the Infarcted Human Heart - Zigzag Course of Activation. *Circulation* 88: 915-926, 1993.
20. Dengler TJ and Katus HA. Stem cell therapy for the infarcted heart ("cellular cardiomyoplasty"). *Herz* 27: 598-610, 2002.
21. DiFrancesco D and Noble D. A model of cardiac electrical activity incorporating ionic pumps and concentration changes. *Philosophical Transactions of the Royal Society of London Series B-Biological Sciences* 307: 353-398, 1985.

22. Eloff BC, Gilat E, Wan XP, and Rosenbaum DS. Pharmacological modulation of cardiac gap junctions to enhance cardiac conduction - Evidence supporting a novel target for antiarrhythmic therapy. *Circulation* 108: 3157-3163, 2003.
23. Faber GM and Rudy Y. Action potential and contractility changes in $[Na^+]_i$ overloaded cardiac myocytes: A simulation study. *Biophysical Journal* 78: 2392-2404, 2000.
24. Fast VG, Darrow BJ, Saffitz JE, and Kleber AG. Anisotropic activation spread in heart cell monolayers assessed by high-resolution optical mapping - Role of tissue discontinuities. *Circulation Research* 79: 115-127, 1996.
25. Fast VG and Kleber AG. Microscopic Conduction in Cultured Strands of Neonatal Rat-Heart Cells Measured with Voltage-Sensitive Dyes. *Circulation Research* 73: 914-925, 1993.
26. Fast VG and Kleber AG. Role of wavefront curvature in propagation of cardiac impulse. *Cardiovascular Research* 33: 258-271, 1997.
27. Filion RJ and Popel AS. Intracoronary administration of FGF-2: a computational model of myocardial deposition and retention. *American Journal of Physiology-Heart and Circulatory Physiology* 288: H263-H279, 2005.
28. Fleischhauer J, Lehmann L, and Kleber AG. Electrical resistances of interstitial and microvascular space as determinants of the extracellular electrical-field and velocity of propagation in ventricular myocardium. *Circulation* 92: 587-594, 1995.
29. Fozzard HA. Membrane capacity of cardiac purkinje fiber. *Journal of Physiology-London* 182: 255-&, 1966.
30. Frank JS and Langer GA. Myocardial Interstitium - Its structure and its role in ionic exchange. *Journal of Cell Biology* 60: 586-601, 1974.
31. Gerdes AM, Onodera T, Wang X, and McCune SA. Myocyte Remodeling During the Progression to Failure in Rats With Hypertension. *Hypertension* 28: 609-614, 1996.
32. Go AS, Hylek EM, Phillips KA, Chang YC, Henault LE, Selby JV, and Singer DE. Prevalence of diagnosed atrial fibrillation in adults - National implications for rhythm management and stroke prevention: the AnTicoagulation and Risk Factors in Atrial Fibrillation (ATRIA) study. *Jama-Journal of the American Medical Association* 285: 2370-2375, 2001.

33. Goette A, Bukowska A, and Lendeckel U. Non-ion channel blockers as anti-arrhythmic drugs (reversal of structural remodeling). *Current Opinion in Pharmacology* 7: 219-224, 2007.
34. Green CR, Peters NS, Gourdie RG, Rothery S, and Severs NJ. Validation of Immunohistochemical quantification in confocal scanning laser microscopy - A comparative assessment of gap junction size with confocal and ultrastructural techniques. *Journal of Histochemistry & Cytochemistry* 41: 1339-1349, 1993.
35. Guerra JM, Everett TH, Lee KW, Wilson E, and Olgin JE. Effects of the gap junction modifier rotigaptide (ZP123) on atrial conduction and vulnerability to atrial fibrillation. *Circulation* 114: 110-118, 2006.
36. Gutstein DE, Danik SB, Lewitton S, France D, Liu FY, Chen FL, Zhang J, Ghodsi N, Morley GE, and Fishman GI. Focal gap junction uncoupling and spontaneous ventricular ectopy. *American Journal of Physiology-Heart and Circulatory Physiology* 289: H1091-H1098, 2005.
37. Hennen JK, Swillo RE, Morgan GA, Keith JC, Schaub RG, Smith RP, Feldman HS, Haugan K, Kantrowitz J, Wang PJ, Abu-Qare A, Butera J, Larsen BD, and Crandall DL. Rotigaptide (ZP123) prevents spontaneous ventricular arrhythmias and reduces infarct size during myocardial ischemia/reperfusion injury in open-chest dogs. *Journal of Pharmacology and Experimental Therapeutics* 317: 236-243, 2006.
38. Henriquez CS. Simulating the Electrical Behavior of Cardiac Tissue Using the Bidomain Model. *Critical Reviews in Biomedical Engineering* 21: 1-77, 1993.
39. Henriquez CS and Hooke NF. Effect Of Interstitial Anisotropy And The Extracellular Volume Conductor On Action Potential Morphology In A Thin Layer Of Cardiac Tissue. *Engineering in Medicine and Biology Society: Proceedings of the Annual International Conference of the IEEE* 2: 600-601, 1992.
40. Henriquez CS and Plonsey R. Effect of resistive discontinuities on waveshape and velocity in a single cardiac fiber. *Medical & Biological Engineering & Computing* 25: 428-438, 1987.
41. Henriquez CS and Plonsey R. Simulation of propagation along a cylindrical bundle of cardiac tissue. 2. Results of simulation. *IEEE Transactions on Biomedical Engineering* 37: 861-875, 1990.
42. Hestenes MR and Stiefel E. Methods of conjugate gradients for solving linear systems. *Journal of Research of the National Bureau of Standards* 49: 409-436, 1952.

43. Ho SY, Cabrera JA, Tran VH, Farr J, Anderson RH, and Sanchez-Quintana D. Architecture of the pulmonary veins: relevance to radiofrequency ablation. *Heart* 86: 265-270, 2001.
44. Hocini M, Ho SY, Kawara T, Linnenbank AC, Potse M, Shah D, Jais P, Janse MJ, Haissaguerre M, and de Bakker JMT. Electrical conduction in canine pulmonary veins - Electrophysiological and anatomic correlation. *Circulation* 105: 2442-2448, 2002.
45. Hodgkin AL. The ionic basis of electrical activity in nerve and muscle. *Biological Reviews of the Cambridge Philosophical Society* 26: 339-409, 1951.
46. Hodgkin AL and Huxley AF. A quantitative description of membrane current and its application to conduction and excitation in nerve. *Journal of Physiology-London* 117: 500-544, 1952.
47. Hodgkin AL, Huxley AF, and Katz B. Ionic currents underlying activity in the giant axon of the squid. *Archives Des Sciences Physiologiques* 3: 129-150, 1949.
48. Hoyt RH, Cohen ML, and Saffitz JE. Distribution and 3-dimensional structure of Intercellular-Junctions in Canine Myocardium. *Circulation Research* 64: 563-574, 1989.
49. Hubbard ML and Henriquez CS. Increased interstitial loading reduces the effect of microstructural variations in cardiac tissue. *Am J Physiol Heart Circ Physiol* 298: H1209-1218, 2010.
50. Hubbard ML and Henriquez CS. Increasing the Effective Interstitial Resistivity Promotes the Escape of Premature Beats. In: *Proceedings of Computers in Cardiology*, edited by Murray A. Park City, Utah, 2009.
51. Hubbard ML, Ying W, and Henriquez CS. Effect of gap junction distribution on impulse propagation in a monolayer of myocytes: a model study. *Europace* 9: vi20-28, 2007.
52. Jais P, Haissaguerre M, Shah DC, Chouairi S, Gencel L, Hocini M, and Clementy J. A focal source of atrial fibrillation treated by discrete radiofrequency ablation. *Circulation* 95: 572-576, 1997.
53. Joyner RW. Effects of the discrete pattern of electrical coupling on propagation through an electrical syncytium. *Circulation Research* 50: 192-200, 1982.

54. Kelvin L. On the theory of the electric telegraph. *Proceedings of the Royal Society of London* 7: 382-390, 1855.
55. Kim J, Bursac N, and Henriquez C. A Computer Model of Engineering Cardiac Monolayers. *Biophysical Journal* In Press, 2010.
56. Kleber AG and Riegger CB. Electrical constants of arterially perfused rabbit papillary muscle. *Journal of Physiology-London* 385: 307-324, 1987.
57. Kleber AG, Riegger CB, and Janse MJ. Electrical uncoupling and increase of extracellular resistance after induction of ischemia in isolated, arterially perfused rabbit papillary muscle. *Circulation Research* 61: 271-279, 1987.
58. Kostin S, Klein G, Szalay Z, Hein S, Bauer EP, and Schaper J. Structural correlate of atrial fibrillation in human patients. *Cardiovascular Research* 54: 361-379, 2002.
59. Kostin S, Rieger M, Dammer S, Hein S, Richter M, Klovekorn WP, Bauer EP, and Schaper J. Gap junction remodeling and altered connexin43 expression in the failing human heart. *Molecular and Cellular Biochemistry* 242: 135-144, 2003.
60. Krassowska W, Pilkington TC, and Ideker RE. Periodic conductivity as a mechanism for cardiac stimulation and defibrillation. *IEEE Transactions on Biomedical Engineering* 34: 555-560, 1987.
61. Krassowska W, Pilkington TC, and Ideker RE. The closed form solution to the period core-conductor model using asymptotic analysis. *IEEE Transactions on Biomedical Engineering* 34: 519-531, 1987.
62. Kucera JP, Rohr S, and Rudy Y. Localization of sodium channels in intercalated disks modulates cardiac conduction. *Circulation Research* 91: 1176-1182, 2002.
63. Kuijpers NHL, Keldermann RH, ten Eikelder HMM, Arts T, and Hilbers PAJ. The role of the hyperpolarization-activated inward current I_f in arrhythmogenesis: A computer model study. *Ieee Transactions on Biomedical Engineering* 53: 1499-1511, 2006.
64. Laurita KR, Girouard SD, and Rosenbaum DS. Modulation of Ventricular Repolarization by a Premature Stimulus: Role of Epicardial Dispersion of Repolarization Kinetics Demonstrated by Optical Mapping of the Intact Guinea Pig Heart. *Circ Res* 79: 493-503, 1996.

65. Laurita KR and Rosenbaum DS. Interdependence of Modulated Dispersion and Tissue Structure in the Mechanism of Unidirectional Block. *Circ Res* 87: 922-928, 2000.
66. Le Heuzey JY, Piziaud O, Piot O, Said MA, Copie X, Lavergne T, and Guize L. Cost of care distribution in atrial fibrillation patients: The COCAF study. *American Heart Journal* 147: 121-126, 2004.
67. Leon LJ and Roberge FA. Directional Characteristics of Action-Potential Propagation in Cardiac-Muscle - a Model Study. *Circulation Research* 69: 378-395, 1991.
68. Leon LJ and Roberge FA. Structural Complexity Effects on Transverse Propagation in a 2-Dimensional Model of Myocardium. *IEEE Transactions on Biomedical Engineering* 38: 997-1009, 1991.
69. Levick JR. Flow through interstitium and other fibrous matrices. *Quarterly Journal of Experimental Physiology and Cognate Medical Sciences* 72: 409-438, 1987.
70. Lin SF, Roth BJ, and Wikswo JP. Quatrefoil reentry in myocardium: An optical imaging study of the induction mechanism. *Journal of Cardiovascular Electrophysiology* 10: 574-586, 1999.
71. Linge S, Sundnes J, Hanslien M, Lines GT, and Tveito A. Numerical solution of the bidomain equations. *Philosophical Transactions of the Royal Society a- Mathematical Physical and Engineering Sciences* 367: 1931-1950, 2009.
72. Liu X, Shi H, Tan H, Wang X, Zhou L, and Gu J. Decreased Connexin 43 and Increased Fibrosis in Atrial Regions Susceptible to Complex Fractionated Atrial Electrograms. *Cardiology* 114: 22-29, 2009.
73. Luke RA and Saffitz JE. Remodeling of Ventricular Conduction Pathways in Healed Canine Infarct Border Zones. *Journal of Clinical Investigation* 87: 1594-1602, 1991.
74. Luo CH and Rudy Y. A dynamic model of the cardiac ventricular action potential. 1. Simulations of ionic currents and concentration changes. *Circulation Research* 74: 1071-1096, 1994.
75. Luo CH and Rudy Y. A model of the ventricular cardiac action potential - depolarization, repolarization, and their interaction. *Circulation Research* 68: 1501-1526, 1991.

76. Mines G. On dynamic equilibrium of the heart. *J Physiol* 46: 349-382, 1913.
77. Moe G. Evidence for reentry as a mechanism of cardiac arrhythmias. *Reviews of Physiology, Biochemistry and Pharmacology* 72: 55-81, 1975.
78. Moe GK. On Multiple Wavelet Hypothesis of Atrial Fibrillation. *Archives Internationales De Pharmacodynamie Et De Therapie* 140: 183-&, 1962.
79. Neuberger H-R, Schotten U, and Allesie MA. Mapping of atrial fibrillation in a goat model of atrial dilatation. *Heart Rhythm* 2: S143-S143, 2005.
80. Peters NS. Myocardial Gap Junction Organization in Ischemia and Infarction. *Microscopy Research and Technique* 31: 375-386, 1995.
81. Poelzing S, Akar FG, Baron E, and Rosenbaum DS. Heterogeneous connexin43 expression produces electrophysiological heterogeneities across ventricular wall. *American Journal of Physiology-Heart and Circulatory Physiology* 286: H2001-H2009, 2004.
82. Poelzing S, Roth BJ, and Rosenbaum DS. Optical measurements reveal nature of intercellular coupling across ventricular wall. *American Journal of Physiology-Heart and Circulatory Physiology* 289: H1428-H1435, 2005.
83. Pogwizd S and Corr P. Electrophysiologic mechanisms underlying arrhythmias due to reperfusion of ischemic myocardium. *Circulation* 76: 404-426, 1987.
84. Pormann J. A modular simulation system for the bidomain equations. *PhD Thesis Duke University Department of Electrical and Computer Engineering*, 1999.
85. Pullan A, Buist M, and Cheng L. Mathematically Modelilng the Electrical Activity of the Heart: From Cell to Body Surface and Back Again. 2005.
86. Pumir A, Arutunyan A, Krinsky V, and Sarvazyan N. Genesis of ectopic waves: Role of coupling, automaticity, and heterogeneity. *Biophysical Journal* 89: 2332-2349, 2005.
87. Qu ZL. Dynamical effects of diffusive cell coupling on cardiac excitation and propagation: a simulation study. *American Journal of Physiology-Heart and Circulatory Physiology* 287: H2803-H2812, 2004.
88. Quan WL and Rudy Y. Unidirectional block and reentry of cardiac excitation-A model study. *Circulation Research* 66: 367-382, 1990.

89. Roberts SF, Stinstra JG, and Henriquez CS. Effect of nonuniform interstitial space properties on impulse propagation: A discrete multidomain model. *Biophysical Journal* 95: 3724-3737, 2008.
90. Rohr S, Kucera JP, Fast VG, and Kleber AG. Paradoxical improvement of impulse conduction in cardiac tissue by partial cellular uncoupling. *Science* 275: 841-844, 1997.
91. Rohr S, Kucera JP, and Kleber AG. Slow Conduction in Cardiac Tissue, I : Effects of a Reduction of Excitability Versus a Reduction of Electrical Coupling on Microconduction. *Circ Res* 83: 781-794, 1998.
92. Roth BJ. Action potential propagation in a thick strand of cardiac muscle. *Circulation Research* 68: 162-173, 1991.
93. Roth BJ. Influence of a Perfusing Bath on the Foot of the Cardiac Action Potential. *Circ Res* 86: e19-22, 2000.
94. Roux N, Havet E, and Mertl P. The myocardial sleeves of the pulmonary veins: potential implications for atrial fibrillation. *Surgical and Radiologic Anatomy* 26: 285-289, 2004.
95. Saito T, Waki K, and Becker AE. Left atrial myocardial extension onto pulmonary veins in humans: Anatomic observations relevant for atrial arrhythmias. *Journal of Cardiovascular Electrophysiology* 11: 888-894, 2000.
96. Saiz J, Ferrero JM, Monserrat M, Ferrero JM, and Thakor NV. Influence of electrical coupling on early afterdepolarizations in ventricular myocytes. *IEEE Transactions on Biomedical Engineering* 46: 138-147, 1999.
97. Schlant R and Alexander R. *The Heart*, 8th Ed., 1994.
98. Shaw RM and Rudy Y. Ionic mechanisms of propagation in cardiac tissue - Roles of the sodium and L-type calcium currents during reduced excitability and decreased gap junction coupling. *Circulation Research* 81: 727-741, 1997.
99. Shiroshita-Takeshita A, Sakabe M, Haugan K, Hennen JK, and Nattel S. Model-dependent effects of the gap junction conduction-enhancing antiarrhythmic peptide rotigaptide (ZP123) on experimental atrial fibrillation in dogs. *Circulation* 115: 310-318, 2007.
100. Sinha S and Christini DJ. Termination of reentry in an inhomogeneous ring of model cardiac cells. *Physical Review E* 66: 061903, 2002.

101. Sommer JR and Scherer B. Geometry of cell and bundle appositions in cardiac muscle - light microscopy. *American Journal of Physiology* 248: H792-H803, 1985.
102. Spach MS. The discontinuous nature of electrical propagation in cardiac muscle - Consideration of a quantitative model incorporating the membrane ionic properties and structural complexities - The ALZA Distinguished Lecture. *Annals of Biomedical Engineering* 11: 209-261, 1983.
103. Spach MS and Boineau JP. Microfibrosis produces electrical load variations due to loss of side-to-side cell connections: A major mechanism of structural heart disease arrhythmias. *Pace-Pacing and Clinical Electrophysiology* 20: 397-413, 1997.
104. Spach MS, Heidlage IF, Barr RC, and Dolber PC. Cell size and communication: Role in structural and electrical development and remodeling of the heart. *Heart Rhythm* 1: 500-515, 2004.
105. Spach MS and Heidlage JF. The Stochastic Nature of Cardiac Propagation at a Microscopic Level - Electrical Description of Myocardial Architecture and Its Application to Conduction. *Circulation Research* 76: 366-380, 1995.
106. Spach MS, Heidlage JF, Dolber PC, and Barr RC. Electrophysiological effects of remodeling cardiac gap junctions and cell size - Experimental and model studies of normal cardiac growth. *Circulation Research* 86: 302-311, 2000.
107. Spach MS, Heidlage JF, Dolber PC, and Barr RC. Extracellular discontinuities in cardiac muscle - Evidence for capillary effects on the action potential foot. *Circulation Research* 83: 1144-1164, 1998.
108. Spach MS, Heidlage JF, Dolber PC, and Barr RC. Mechanism of origin of conduction disturbances in aging human atrial bundles: Experimental and model study. *Heart Rhythm* 4: 175-185, 2007.
109. Spach MS, Miller WT, Geselowitz DB, Barr RC, Kootsey JM, and Johnson EA. The Discontinuous Nature of Propagation in Normal Canine Cardiac-Muscle - Evidence for Recurrent Discontinuities of Intracellular Resistance That Affect the Membrane Currents. *Circulation Research* 48: 39-54, 1981.
110. Stein M, van Veen TAB, Remme CA, Boulaksil M, Noorman M, van Stuijvenberg L, van der Nagel R, Bezzina CR, Hauer RNW, de Bakker JMT, and van Rijen HVM. Combined reduction of intercellular coupling and membrane excitability differentially affects transverse and longitudinal cardiac conduction. *Cardiovascular Research* 83: 52-60, 2009.

111. Steinberg BE, Glass L, Shrier A, and Bub G. The role of heterogeneities and intercellular coupling in wave propagation in cardiac tissue. *Philosophical Transactions of the Royal Society a-Mathematical Physical and Engineering Sciences* 364: 1299-1311, 2006.
112. Steiner I, Hájková P, Kvasnička J, and Kholová I. Myocardial sleeves of pulmonary veins and atrial fibrillation: a postmortem histopathological study of 100 subjects. *Virchows Archiv* 449: 88-95, 2006.
113. Steinhaus BM, Spitzer KW, and Isomura S. Action potential collision in heart tissue-computer simulations and tissue experiments. *IEEE Transactions on Biomedical Engineering* 32: 731-742, 1985.
114. Stinstra JG, Hopfenfeld B, and MacLeod RS. On the passive cardiac conductivity. *Annals of Biomedical Engineering* 33: 1743-1751, 2005.
115. Stinstra JG, Shome S, Hopfenfeld B, and MacLeod RS. Modelling passive cardiac conductivity during ischaemia. *Medical & Biological Engineering & Computing* 43: 776-782, 2005.
116. Trayanova N and Pilkington TC. - A bidomain model with periodic intracellular junctions: a one-dimensional analysis. - 40: - 433, 1993.
117. Wagner MB, Golod D, Wilders R, Verheijck EE, Joyner RW, Kumar R, Jongsma HJ, van Ginneken ACG, and Goolsby WN. Modulation of propagation from an ectopic focus by electrical load and by extracellular potassium. *American Journal of Physiology-Heart and Circulatory Physiology* 41: H1759-H1769, 1997.
118. Wang Y and Rudy Y. Action potential propagation in inhomogeneous cardiac tissue: safety factor considerations and ionic mechanism. *American Journal of Physiology-Heart and Circulatory Physiology* 278: H1019-H1029, 2000.
119. Wang YG, Kumar R, Wagner MB, Wilders R, Golod DA, Goolsby WN, and Joyner RW. Electrical interactions between a real ventricular cell and an anisotropic two-dimensional sheet of model cells. *American Journal of Physiology-Heart and Circulatory Physiology* 278: H452-H460, 2000.
120. Wiegerinck RF, Verkerk AO, Belterman CN, van Veen TAB, Baartscheer A, Opthof T, Wilders R, de Bakker JMT, and Coronel R. Larger Cell Size in Rabbits With Heart Failure Increases Myocardial Conduction Velocity and QRS Duration. *Circulation* 113: 806-813, 2006.

121. Wijffels MCEF, Kirchhof CJHJ, Dorland R, and Allessie MA. Atrial Fibrillation Begets Atrial Fibrillation : A Study in Awake Chronically Instrumented Goats. *Circulation* 92: 1954-1968, 1995.
122. Wilders R, Wagner MB, Golod DA, Kumar R, Wang YG, Goolsby WN, Joyner RW, and Jongsma HJ. Effects of anisotropy on the development of cardiac arrhythmias associated with focal activity. *Pflugers Archiv-European Journal of Physiology* 441: 301-312, 2000.
123. Winfree A. Ventricular reentry in three dimensions. In: *Cardiac Electrophysiology: From Cell to Bedside* (First ed.), edited by DP Z and J J. Philadelphia, PA, 1990.
124. Winslow RL, Varghese A, Noble D, Adlakha C, and Hoythya A. Generation and Propagation of Ectopic Beats Induced by Spatially Localized Na-K Pump Inhibition in Atrial Network Models. *Proceedings of the Royal Society of London Series B-Biological Sciences* 254: 55-61, 1993.
125. Wit AL and Boyden PA. Triggered activity and atrial fibrillation. *Heart Rhythm* 4: S17-S23, 2007.
126. Xing DZ, Kjolbye AL, Petersen JS, and Martins JB. Pharmacological stimulation of cardiac gap junction coupling does not affect ischemia-induced focal ventricular tachycardia or triggered activity in dogs. *American Journal of Physiology-Heart and Circulatory Physiology* 288: H511-H516, 2005.
127. Xu J, Cui G, Esmailian F, Plunkett M, Marelli D, Ardehali A, Odum J, Laks H, and Sen L. Atrial Extracellular Matrix Remodeling and the Maintenance of Atrial Fibrillation. *Circulation* 109: 363-368, 2004.

Biography

MARJORIE LETITIA HOLDEN HUBBARD

Date of Birth: May 27, 1982

Birthplace: Huntsville, AL

EDUCATION

Duke University, Durham, NC

PhD, Biomedical Engineering, May 2010

Georgia Institute of Technology, Atlanta, GA

B.S., Electrical Engineering, *Summa Cum Laude*, *Tau Beta Pi*, *Eta Kappa Nu*

Spelman College, Atlanta, GA

B.S., Physics, *Class Valedictorian*, *Phi Beta Kappa*

AWARDS/HONORS

UNCF/Merck Dissertation Fellowship, 2008-2009

National Science Foundation Fellowship, 2004-2007

James B. Duke Fellowship, 2004-2008

Duke Endowment Fellowship, 2004-2008

Barry Goldwater Fellowship, 2002-2004

PUBLICATIONS

Hubbard ML, Henriquez CS. Increased interstitial loading reduces the effect of microstructural variations in cardiac tissue. *Am J Physiol Heart Circ Physiol*. 298: H1209-1218, 2010.

Hubbard, ML, Henriquez, CS. Increased interstitial resistivity facilitates the escape of premature beats. *Comput. Cardiol.*, Vol. 36, pp, 661-664. Park City, Utah, Sept. 2009.

Hubbard ML, Ying W, Henriquez CS. Effect of gap junction distribution on impulse propagation in a monolayer of myocytes: a model study. *Europace* 2007; 9(suppl_6):vi20-28.